Strojniški vestnik

Journal of Mechanical Engineering

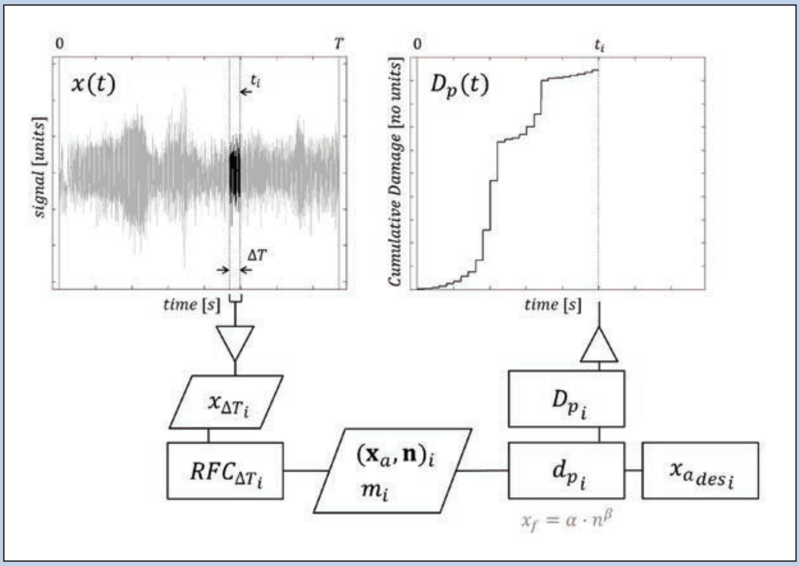

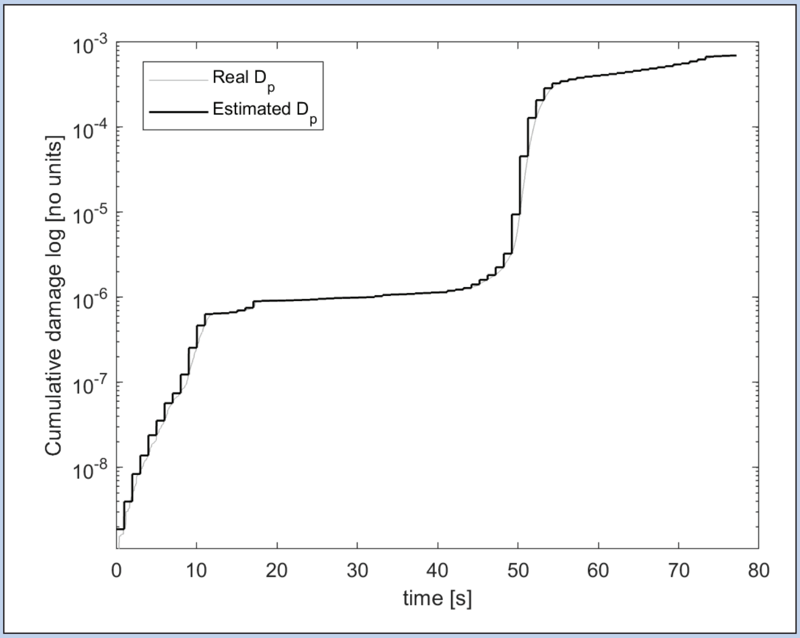

no. 10
year 2020
volume 66

Strojniški vestnik – Journal of Mechanical Engineering (SV-JME)

Aim and Scope

The international journal publishes original and (mini)review articles covering the concepts of materials science, mechanics, kinematics, thermodynamics, energy and environment, mechatronics and robotics, fluid mechanics, tribology, cybernetics, industrial engineering and structural analysis.

The journal follows new trends and progress proven practice in the mechanical engineering and also in the closely related sciences as are electrical, civil and process engineering, medicine, microbiology, ecology, agriculture, transport systems, aviation, and others, thus creating a unique forum for interdisciplinary or multidisciplinary dialogue.

The international conferences selected papers are welcome for publishing as a special issue of SV-JME with invited co-editor(s).

Editorial Office
University of Ljubljana, Faculty of Mechanical Engineering
SV-JME, Aškerčeva 6, SI-1000 Ljubljana, Slovenia
Phone: 386 (0)1 4771 137
Fax: 386 (0)1 2518 567
info@sv-jme.eu, http://www.sv-jme.eu

Print: Koštomaj printing office, printed in 275 copies

Founders and Publishers
University of Ljubljana, Faculty of Mechanical Engineering, Slovenia
University of Maribor, Faculty of Mechanical Engineering, Slovenia
Association of Mechanical Engineers of Slovenia
Chamber of Commerce and Industry of Slovenia, Metal Processing Industry Association

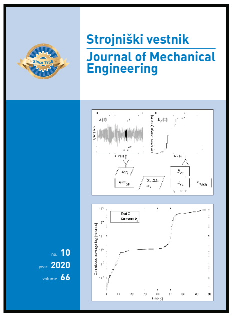

Cover:
The flow chart of the proposed damage online evaluation.
A comparison between cumulated real damage (Real) over time and the results of the proposed methodology (Estimated).

Image courtesy:
Department of Engineering, University of Perugia, Perugia, Italy

ISSN 0039-2480, ISSN 2536-2948 (online)

General information

Strojniški vestnik – Journal of Mechanical Engineering is published in 11 issues per year (July and August is a double issue).

Institutional prices include print & online access: institutional subscription price and foreign subscription €100,00 (the price of a single issue is €10,00); general public subscription and student subscription €50,00 (the price of a single issue is €5,00). Prices are exclusive of tax. Delivery is included in the price. The recipient is responsible for paying any import duties or taxes. Legal title passes to the customer on dispatch by our distributor. Single issues from current and recent volumes are available at the current single-issue price. To order the journal, please complete the form on our website. For submissions, subscriptions and all other information please visit: *http://www.sv-jme.eu.*

You can advertise on the inner and outer side of the back cover of the journal. The authors of the published papers are invited to send photos or pictures with short explanation for cover content.

We would like to thank the reviewers who have taken part in the peer-review process.

The journal is subsidized by Slovenian Research Agency.

Strojniški vestnik - Journal of Mechanical Engineering is available on *https://www.sv-jme.eu*.

Contents

Strojniški vestnik - Journal of Mechanical Engineering
volume 66, (2020), number 10
Ljubljana, October 2020
ISSN 0039-2480

Published monthly

Papers

Strojniški vestnik - Journal of Mechanical Engineering 66(2020)10, 557-566

DOI:10.5545/sv-jme.2020.6853

Original Scientific Paper

Received for review: 2020-07-09
Received revised form: 2020-08-21
Accepted for publication: 2020-09-24

How to Experimentally Monitor the Fatigue Behaviour of Vibrating Mechanical Systems?

Filippo Cianetti*
University of Perugia, Italy

Fatigue damage and, in general, fatigue behaviour is not simple to observe or estimate during the operational life of a generic vibrating mechanical system. There are a lot of theoretical or numerical methods that allow to evaluate it or by knowing a priori the loading conditions and obtaining output stress states by adopting numerical models of the mechanical system or by directly experimentally measuring and acquiring stress/strain states. A few examples of instruments (e.g. rain flow recorders) or measurement chains dedicated to estimate it in time domain or frequency domain are found in the literature but none that fully both observes the system dynamic behaviour and estimates the related actualized cumulated damage, and, thus, none that can estimate the residual life of the system itself.

In this paper, a simple time-domain method, designed to monitor the instantaneous fatigue behaviour by definition of the instantaneous and cumulated potential damage or of equivalent damage signal amplitude is presented, based on rain-flow counting method and a damage linear cumulation law and starting from system dynamics signals. This methodology was designed to overestimate real damage to alert the system manager before any crack starts and to be simply translated into electronic boards that can be mounted on generic mechanical systems and linked to one of the sensors that usually monitor system functionality.

Keywords: fatigue; damage; rain flow counting; random loads

Highlights

- *A smart procedure to on-line evaluate the fatigue behaviour of mechanical systems is presented.*
- *It is based on rain-flow counting method and a damage linear cumulation law.*
- *It is designed to be simply translated into electronic boards.*
- *This method allows placing fatigue among the phenomena to be controlled in feedback in any mechanical system.*

0 INTRODUCTION

Fatigue damage and, in general, fatigue behaviour is not simple to be observed or estimated during the operational life of a generic vibrating mechanical system (e.g. automotive [1] and [2], aeronautical [3] and naval applications [4] or wind turbines [5]). Many theoretical or numerical methods allow evaluating it by knowing a priori the loading conditions (i.e. force or acceleration) [6], expressed in time [6] to [10] or frequency domain [10] to [12], and obtaining output stress states by adopting numerical models of the mechanical system (i.e. multibody (MBS) [13], finite element (FE) [14], multibody with flexible elements (Flex/MBS) [15]) or by directly experimentally measuring and acquiring stress/strain states, knowing, by hypotheses, the fatigue strength (i.e. S-N Wohler or Basquin curve [16]).

A few examples of instruments or measurement chains dedicated to evaluate it in time domain (rain flow recorder [17]) or in frequency domain [18] and [19] are available the in literature but none that fully observes the system dynamic behaviour (i.e. accelerations, internal loads, strains) and foresights the related actualized damage and, is thus able to estimate the residual life of the system itself.

In this paper, a simple time-domain method (used in previous papers [20] and [21]), designed to monitor the instantaneous fatigue behaviour by definition of instantaneous and cumulated potential damage or equivalent damage signal amplitude is presented, based on the Rain Flow Counting (RFC) method [16], on a damage linear cumulation law (Palmegren-Miner's rule [16]), and starting from signals coming from system dynamics. This methodology was designed to overestimate real damage to alert the system manager before any crack starts and to be translated simply into an electronic board to be mounted on a generic mechanical system and linked to one of the sensors that usually monitor system functionality. To this aim, this paper presents its translation in a computing environment dedicated to the dynamic multi-domain simulation of mechanical systems and to the design and verification of control systems. This passage made it possible to verify how the results, obtainable from the evaluation tool, can be obtained online both directly, by the physical measurements made on the turbine, and, in any case, by numerical measures, obtainable through more or less complex dynamic models of the generator itself.

The fundamental hypothesis of this work is that many experimental measures are acquired online,

*Corr. Author's Address: University of Perugia , Via G. Duranti, 93, 06125 Perugia, Italy, filippo.cianetti@unipg.it

for various reasons, on generic machines (i.e. speed, accelerations, moments) and whose values are instantly used to control any condition without being affected by assessments related to the duration, fatigue or damage of the system itself.

Assuming the linear behaviour of the machine and of the mechanical system, a relationship can always be established between these measures and the generic stress state in any location of the components, allowing to drive evaluations toward fatigue on such generic signals but adopting the classical evaluation tools adopted on stress state time histories. If the evaluation of the fatigue behaviour is made starting from a generic signal on which all the hypotheses and tools developed over the years for the evaluation of the damage starting from stress state cannot be directly adopted [16], the definition of fatigue Potential Damage and, therefore, the proposed method can be justified.

1 TIME DOMAIN FATIGUE ANALYSIS

If a generic signal (i.e. acceleration, force, moment) x is considered, to evaluate the mechanical system or component fatigue behaviour and to evaluate its durability performance, the fatigue strength curve related to it has to be known. Its expression is the following, similar to that of the Basquin [16] curve for stress signals:

$$x_f = \alpha \cdot N^{\beta}, \tag{1}$$

where x_f is the strength amplitude value of the signal related to an applied cycles number N, α is the intercept of the curve on the amplitudes axis for $N=1$, β is the curve slope considered constant in the whole cycles range.

Its inverse representation is also valid:

$$N = \sqrt[\beta]{\frac{x_a}{\alpha}}, \tag{2}$$

where N represents the strength cycles number when an amplitude value x_a of the alternating signal is applied.

The choice to adopt a single slope curve is justified by the nature of the proposed method intended to monitor potential damage but not real damage. The most common evaluation method of the fatigue behaviour, i.e., of the damage, therefore, requires two further steps: to identify a damage model and to choose a counting and identifying method for the alternating cycles of the signal under examination.

The adoptable damage model is the linear damage cumulation law of Palmegren-Miner [16]. Regarding the cycles counting, the counting method considered as standard in this paper; however, the scientific community and international standards uses the RFC as standard [16]. The RFC identifies the closed hysteretic cycles defined by the signal and, generally, the cycles are collected in bands (bins) to reduce the result dimensions of this evaluation. A load spectrum (i.e. a three-column matrix) can be obtained in which the number of counted cycles n, the associated mean value x_m and amplitude value x_a of the signal are represented in its generic row. All the counted cycles can also still be kept in memory, with relative amplitude and mean value, without to be sampled in bands, obtaining, in this case, a spectrum with as many rows as many cycles were counted, that is assuming for each row $n=1$

The presence of a mean value would require a further step to adopt the previously mentioned damage model. By adopting, for example, the correction of Goodman or Gerber [16], it is possible to trace back to an equivalent amplitude value of the cycle by knowing ultimate static strength related to of the variable, x_{ut}.

However, following the hypothesis introduced in the introduction and at the beginning of this sections, that the signal that is going to be analysed does not allow going back to parameters strictly related to the component strength, for example to the ultimate static strength, the first simplification hypothesis assumed is that the mean value of the generic cycle will be neglected.

Assuming the above hypothesis, the load spectrum can be represented as shown below:

$$(\mathbf{x}_a, \mathbf{n}), \tag{3}$$

with, respectively, $\mathbf{x}_a$ and $\mathbf{n}$ the vectors of amplitude and number of applied or counted cycles.

By knowing spectrum (Eq. (3)), fatigue damage is evaluable by Palmegren-Miner rule, that is by the following:

$$D_p = \sum_{i=1}^{m} \left[\frac{n_i}{\sqrt[\beta]{\frac{x_{ai}}{\alpha}}} \right], \tag{4}$$

where m is the total number of counted cycles, D_p the cumulated damage [16]. Subscript p is used to remember that the damage, not being calculated necessarily starting from a stress value, is potential damage [22] and [23], very useful for comparative analysis but not to be analysed as the absolute value of the *real* damage

Another definition, useful to better understand the subsequent steps proposed by the method object of the present paper, is that of damage equivalent signal (DES) [5], often used in the field of wind engineering.

Under the hypothesis of the constant slope of the fatigue strength curve, by knowing the damage or equivalently the load spectrum, it is possible to define a stationary cyclic condition equivalent to the entire spectrum [23] in terms of damage. Given an arbitrary number of cycles, to which it is possible to assign the value of the total number of cycles m, it is always possible to evaluate the equivalent amplitude value $x_{a_{des}}$ of the signal that determines the same damage of the whole spectrum ($\mathbf{x}_a, \mathbf{n}$) by means of the following equation:

$$x_{a_{des}} = \alpha \cdot \left\{ m \cdot \sum_{i=1}^{m} \left[\sqrt[\beta]{\frac{x_{a_i}}{\alpha}} / n_i \right] \right\}^{\beta}, \qquad (5)$$

that can be also expressed as follows by adopting damage definition (Eq. (4)):

$$x_{a_{des}} = \alpha \cdot \left[\frac{m}{D_p} \right]^{\beta}. \qquad (6)$$

2 PROPOSED PROCEDURE FOR DAMAGE MONITORING

To evaluate the cumulative damage at a given moment in the life of the mechanical system requires acquiring the whole history of the signal, considered representative of its behaviour, from the first use of the machine, seamlessly, to the moment of evaluation. Moreover, it is useful to instantaneously know if the dynamic condition is dangerous or critical for system fatigue behaviour.

The evaluation of cumulated damage is difficult to be performed both for reasons of memory space allocation and for reasons related to computational times to perform cycles counting through RFC and then to damage evaluation. As concerns the second aim, an instantaneous damage definition does not exist, such as an instantaneous equivalent damage value of the reference signal to be adopted to control system dynamics actively.

The author wants to demonstrate the possibility of monitoring the potential damage of a generic machine by evaluating it at any of the operating times without taking up all the memory space required by the ideal methodology, evaluating it by adopting a mobile window defined in the time domain, of appropriate characteristics, allowing by this approach to define the "instantaneous" damage such as the "instantaneous" equivalent damage signal.

Let us imagine having a signal measured throughout its temporal extension T and on which it is, therefore, possible to evaluate the *real* potential damage by applying the RFC and Palmgren-Miner's rule (Eq. (4)) in increasing time intervals $[0, t_i]$, with t_i between 0 and T. This enables defining a time history of the damage $D_p(t)$. Associated with this time history, the time history of the damage equivalent signal $x_{a_{des}}(t)$ can also be obtained. Fig. 1 shows the flow chart of the process.

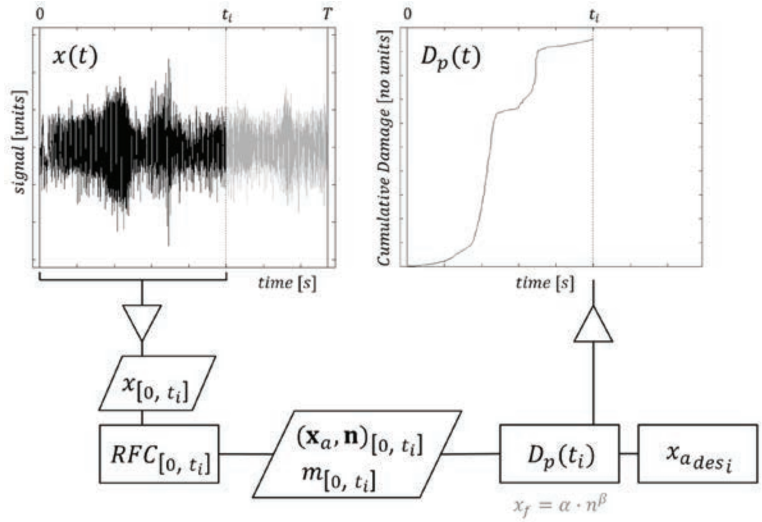

Fig. 1. *Flow chart of standard evaluation of damage time history* [20]

The formulation of the RFC method is a function of the hypothesis that the signal time history is single or repeats itself several times, which introduces a dichotomy of the load spectrum and, therefore, of the damage and of the equivalent alternating value of the signal caused by the definition of residue [16] and [24] and its management within the counting method. The residues are the values of the signal that do not determine any closed hysteretic cycle and, therefore, are not considered in the evaluation of the damage for single signal time history. For signals that repeats several times, however, by adopting the rule of Cloorman-Seeger or ASTM [24] and [25], all the cycles are forcibly closed, which determines a different assessment of the damage for the two aforementioned hypotheses.With the objective of monitoring fatigue in mechanical systems that are typically very long-term loaded with variable and random loads, the hypothesis of repeating signal is adopted in this paper and in this proposed approach.

The first step of the proposed procedure is to define a moving window.

Which sampling time dt should has to be taken? How long must the mobile window be ΔT?

The answers to these two questions define the fundamental choices of the procedure.

Answering these questions means analysing the mechanical system and the load conditions to which it is typically subjected and, therefore, presumably, to which it will be subjected in the future, during operating conditions.

The analysis of the frequency content of the loads (accelerations or forces) and of the natural frequencies of the system and/or component constitutes the instrument with which to reach and define these two values.

The sampling time must be such as to capture the maximum frequency f_{max} that is wanted to be observed, whether this is the maximum observable in the input or that represents the natural mode of maximum natural frequency that is to be considered. The sampling time dt must be k times lower than that corresponding to the maximum frequency value:

$$dt = \frac{1}{k \cdot f_{max}}. \tag{7}$$

The length of the mobile window ΔT must instead be such as to capture the minimum frequency f_{min} that is wanted to be observed, whether this is the minimum observable in the input or that represents the natural mode of minimum natural frequency that is to be considered. ΔT must be at least k times the value of the one corresponding to the minimum frequency:

$$\Delta T = k \cdot \frac{1}{f_{min}}. \tag{8}$$

These two limit values allow observing and, therefore, being able to count the cycles associated with both fast and slow phenomena in the mobile window, in an appropriate number that can represent a significant spectrum for the loading condition.

Once the floating window has been defined, this is the data buffer that is continuously filled in for the evaluation of fatigue behaviour.

In Fig. 2, a flow chart of the proposed procedure is shown.

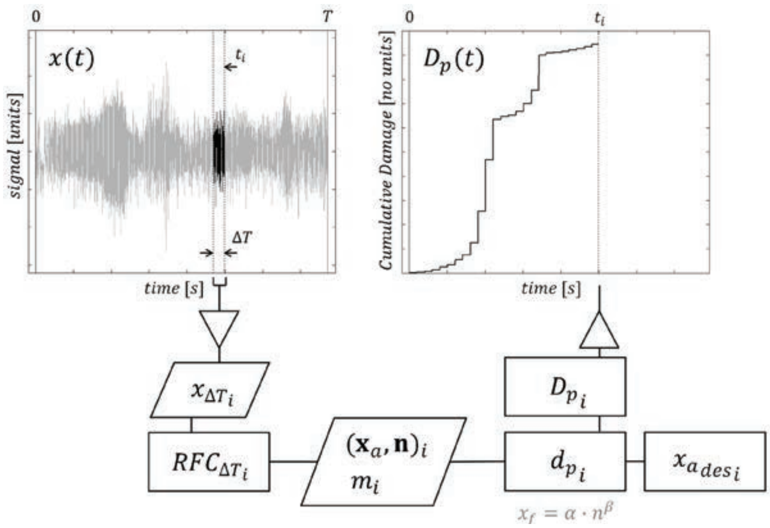

Fig. 2. *Flow chart of proposed evaluation of damage time history* [20]

When the mobile i^{th} window is post-processed, the load spectrum obtained by RFC is:

$$\left(\mathbf{x}_a, \mathbf{n}\right)_i . \tag{9}$$

The Cloorman-Seeger hypothesis is followed without considering the cycle mean value.

If a strength curve such as Eq. (1) is adopted, it is possible to define the i^{th} potential damage d_{p_i}, which is called instantaneous damage, meaning by instantaneous the one associated with the current mobile window:

$$d_{p_i} = \sum_{k=1}^{m_i} \left[\frac{\left(n_k\right)_i}{\sqrt[\beta]{\dfrac{\left(x_{a_k}\right)_i}{\alpha}}} \right], \tag{10}$$

in which subscript i refers to i^{th} window and k to the generic spectrum cycle (Eq. (9)), counted in the same window. m_i is the total number of cycles counted in the window.

The cumulated damage at the generic instant, that is at the generic i^{th} window, is:

$$D_{p_i} = \sum_{r=1}^{i} d_{p_i} . \tag{11}$$

Similarly, the DES related to the window is:

$$x_{a_{des_i}} = \alpha \cdot \left\{ m_i \cdot \sum_{k=1}^{m_i} \left[\sqrt[\beta]{\frac{\left(x_{a_k}\right)_i}{\alpha}} / \left(n_k\right)_i \right] \right\}^{\beta}, \tag{12}$$

$$x_{a_{des_i}} = \alpha \cdot \left[\frac{m_i}{d_{p_i}} \right]^{\beta} . \tag{13}$$

The value $x_{a_{des_i}}$ is strongly influenced by the number of cycles counted in the window, m_i, and therefore window by window, could vary in value, increasing or decreasing, without, however, meaning that the damage has increased or decreased. For example, if two windows i^{th} and $(i+1)^{th}$ generate the same instantaneous damage d_p but the two windows contain different numbers of cycles m_i and m_{i+1}, two different values of $x_{a_{des}}$ occur for the same damage. To overcome this result and have a value of comparable among the various windows and, therefore, independent of the number of cycles, the value of the normalized DES has been defined $\overline{x}_{a_{des}}$ that is evaluated in the hypothesis of a number of cycles constant for all the windows. In the case of the number of cycles constant and equal to 1 its definition is:

$$\overline{x}_{a_{des_i}} = \alpha \cdot \left\{ \sum_{k=1}^{m_i} \left[\sqrt[\beta]{\frac{\left(x_{a_k}\right)_i}{\alpha}} / \left(n_k\right)_i \right] \right\}^{\beta}, \tag{14}$$

$$\overline{x}_{a_{des_i}} = \alpha \cdot \left[d_{p_i} \right]^{-\beta} . \tag{15}$$

It has to be highlighted that the definition of the fatigue curve as previously done and the consequent damage evaluation procedure are strictly related. If we have to manage signals that are not stresses or strains and thus not directly related to the concept of the Basquin curve or of hot spot stress or of the damage rule, a virtual damage evaluation has to be accepted, which that means the definition of a strength curve that implicitly considers aspects such as stress concentration, mean effect, or reliability. As more these are well modelled into the curve, the potential damage and the instantaneous damage will be closer to the real one.

3 SIMPLE TEST CASE

The example (signal) considered to test the goodness of the method is shown in Fig. 3 and relative to an accelerometric measurement carried out in a wind tunnel, on a mini-wind generator [20], [21] and [26]. It varies in a rage from 2 m/s² to −2 m/s².

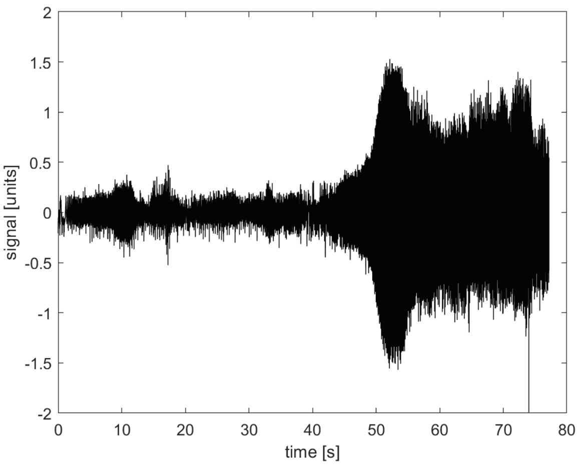

Fig. 3. *Time history of signal test case*

Figs. 4 and 5 show the rain flow matrix, the cumulative of the amplitudes of the cycles (Fig. 4) and the time histories of the equivalent signal (DES) and of the damage (Fig. 5). The calculation of the damage and of the equivalent signal was carried out by assuming a fatigue strength curve with parameters $\alpha = 924$ m/s² and $\beta = 0,2228$

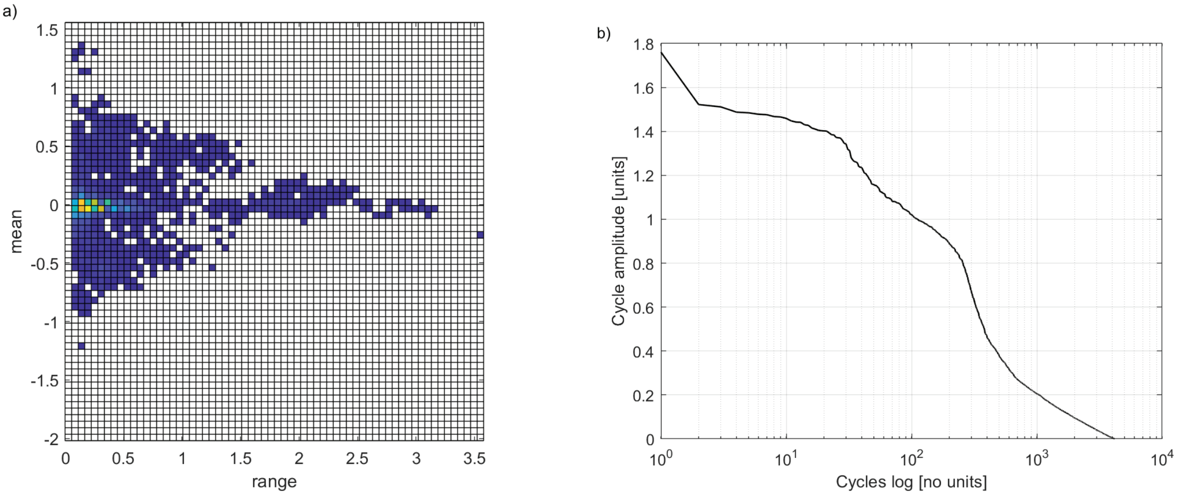

Fig. 4. *a) Rain flow counting matrix, and b) cycles amplitude cumulative of test case time history*

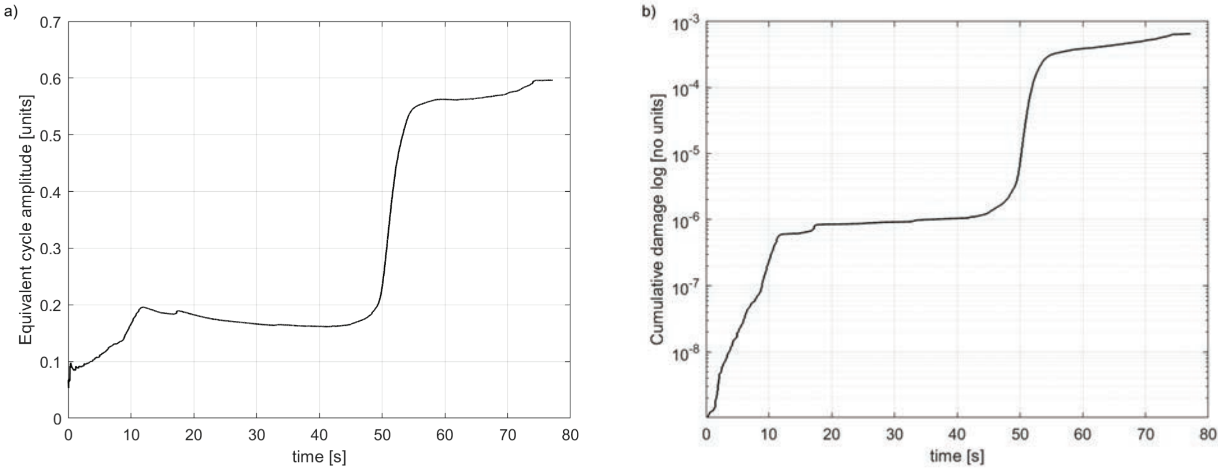

Fig. 5. *a) Damage equivalent signal and b) cumulative damage time histories of test case signal*

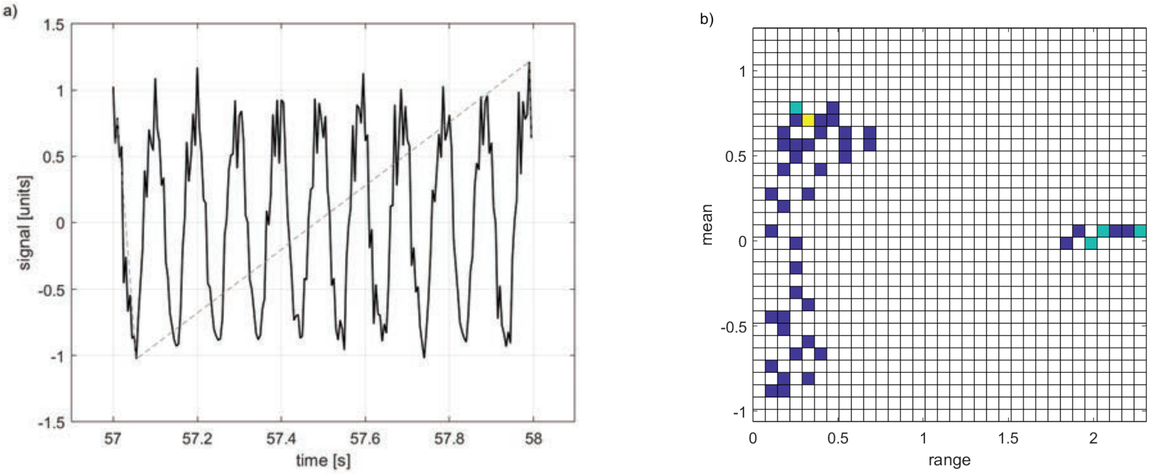

Fig. 6. *a) Example of i^{th} signal time window of proposed process (i = 58), and b) its rain flow matrix*

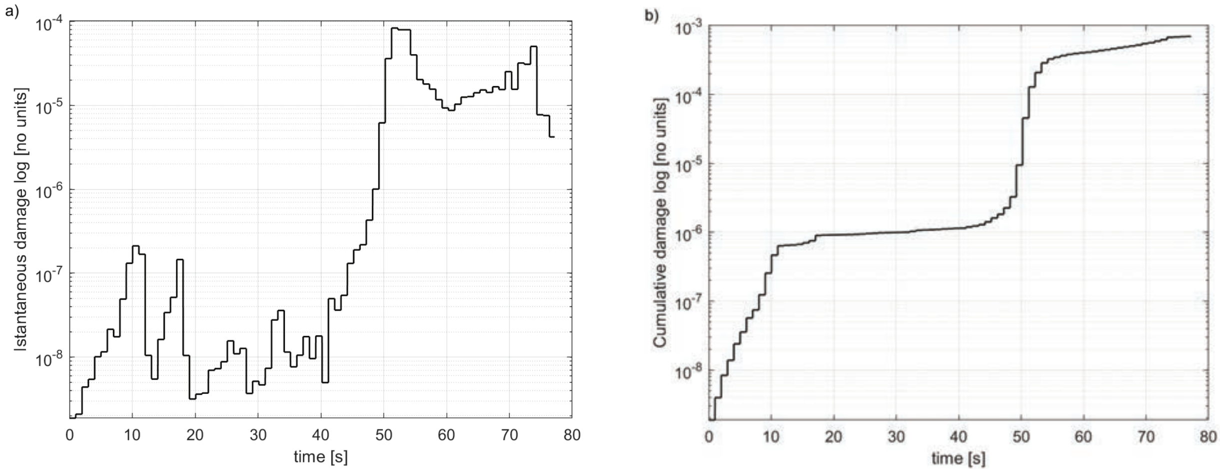

Fig. 7. *Proposed method results; a) instantaneous damage d_p, and b) cumulative damage D_p time histories*

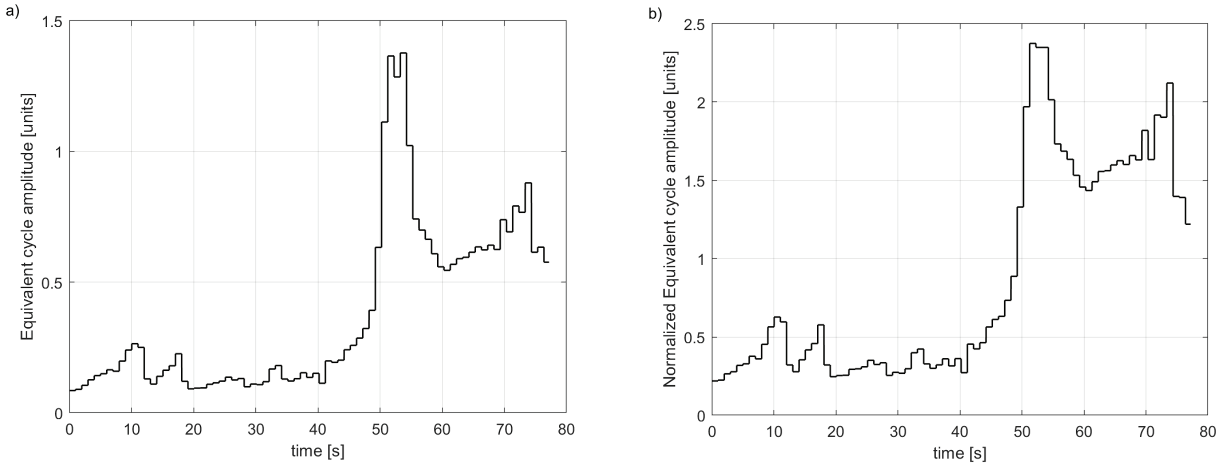

Fig. 8. *Proposed method results; a) damage equivalent signal amplitude $x_{a_{des}}$, and b) normalized damage equivalent signal amplitude $\bar{x}_{a_{des}}$ time histories*

Analysing the temporal profile of the wind speed, which in this case was constant (therefore without a defined frequency content), the minimum and maximum frequencies were defined exclusively starting from the natural frequencies of the tower [26]. Considering as a minimum factor a factor k (Eqs. (7) and (8)) equal to 5, a mobile time window has been defined, characterized by $\Delta T = 10$ s and $dt = 0.005$ s, which satisfies both relations (Eqs. (7) and (8)).

Fig. 6 shows one of the moving windows ($i = 8$) corresponding to an absolute time t_i (Fig. 2) equal to 8 s and the relative Rain Flow matrix; Fig 7 shows the instantaneous damage (d_p) and the cumulated one (D_p) evaluated over the whole test time history.

In order to understand the evaluation of DES carried out following the hypothesis adopted in Eqs. (4) and (5), Fig. 8 shows the time histories of DES obtained by considering the real number of cycles per window m_i (see Eqs. (2) and (3)) and considering it equal to 1 (see Eqs. (4) and (5)).

In the end, the time history of the real cumulated damage (Fig. 5) was compared with the corresponding trend obtained by means of the proposed methodology (Fig. 9). The trend of the instantaneous damage d_{p_i} obtained from the proposed methodology cannot be compared to a similar real value since the damage cannot be defined in absolute terms as an instantaneous value. In order to carry out a qualitative comparison, however, d_{p_i} was compared with the first derivative of the real cumulated damage dD_p/dt (Fig. 9). A comparison between the equivalent signals (DES) is not possible since, by definition, while for the real signal the number of cycles m grows monotonously over time (see Fig. 1) in the sampled one (proposed

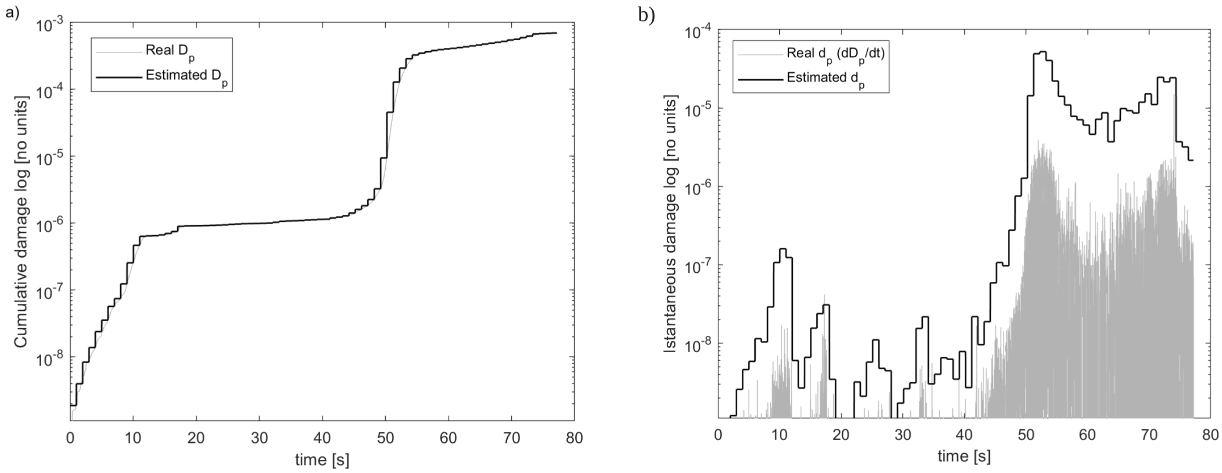

Fig. 9. *Comparison between results obtained by proposed method (Estimated) and standard one (Real); a) cumulative damage D_p, and b) instantaneous damage d_p time histories*

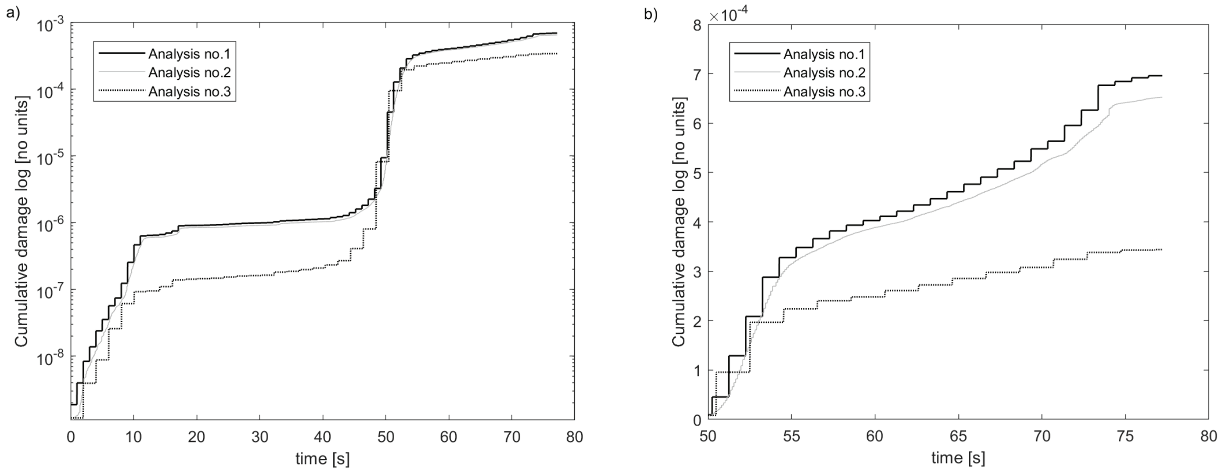

Fig. 10. *Proposed method sensitivity analysis; potential damage cumulatives; a) comparison among results obtained by adopting windowing sizes of Table 1, b) detailed comparison (in linear scale) for the last 30 seconds of the signal*

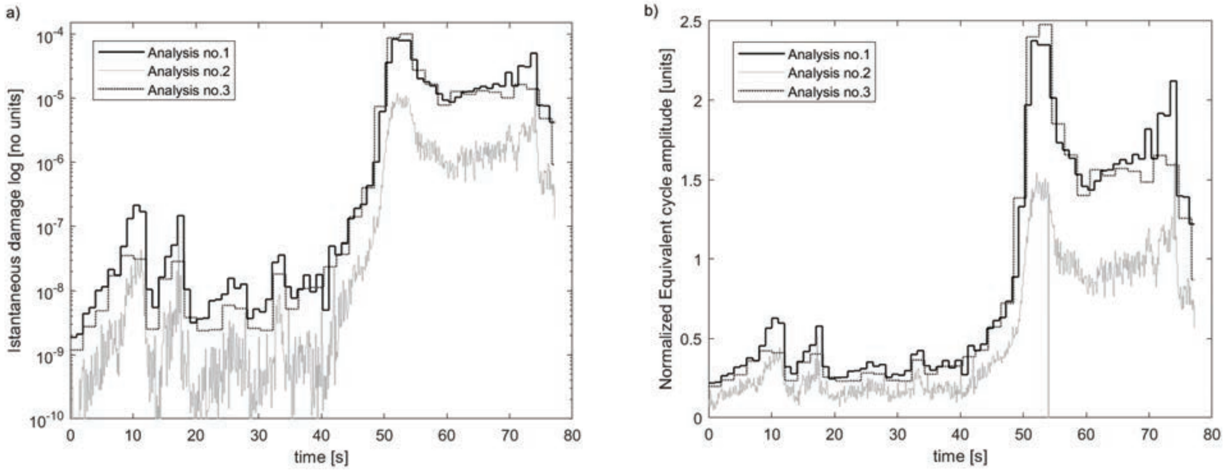

Fig. 11. *Proposed method sensitivity analysis; comparison among results obtained by adopting windowing sizes of Table 1; a) instantaneous damage and b) normalized DES*

method) each window shows a number of increasing or decreasing variable cycles (see Fig. 2).

The comparison between the cumulative damage time histories (Fig. 9) shows how the proposed method is sufficiently accurate to estimate both the trend but also the absolute value of the damage.

In the final part of the paper, how the choice of an incorrect sampling time rather than an incorrect size of the mobile window can negatively affect the obtainable results is shown.

In Figs. 10 and 11 the results previously obtained with $\Delta T = 1.0$ s and $dt = 0.005$ s are compared with those obtained with other two pairs of values of ΔT and dt for which values too small of ΔT have been deliberately adopted, from not being able to count the low-frequency cycles accurately (in this test case the most important), and too large values of dt have also adopted, losing the small-amplitude cycles (in this test case, the greater number) (Table 1).

Table 1. *Windowing parameters adopted for sensitivity analysis*

	Mobile window parameters	
	dt [s]	ΔT [s]
Analysis no.1	0.005	1.00
Analysis no.2	0.005	0.10
Analysis no.3	0.020	1.00

Fig. 10 compares the time histories of the cumulative damage, real and estimated by the proposed method (represented in a logarithmic scale on the left and in a linear scale and for the final part of the signal on the right). In Fig. 11 the trends of the instantaneous damage (Fig. 11a) and of the normalized equivalent signal (Fig. 11b) are instead compared.

It can be noted that the choice of these two parameters significantly influences the results.

4 CONCLUSIONS

In this paper, it has been demonstrated how, starting from the online measurement of any representative signal of the behaviour of the mechanical system, it is possible to define and obtain an instantaneous evaluation of the potential damage of the signal in terms of damage (DES) in the time domain. This possibility provides the scientific and technical community the automatic control the possibility to insert the fatigue among the phenomena to be controlled in feedback in any mechanical system (i.e., automotive vehicles, aircraft, trains, ships, wind turbines) evaluating not only the maximum or minimum values in the signal but also their damaging potential.

In this way, in addition to an instantaneous evaluation, a cumulative evaluation of the potential damage is also obtained, which becomes a further control parameter, given an admissible threshold for this signal.

The author does not want to estimate the final damage related to an assigned time duration of the system by observing a single time window (in this case, that has to be sufficiently long to stabilize damage variance) but only to evaluate an "instantaneous" one and obtain the actual cumulated damage by cumulating these values, which is a characteristic of the approach that allows it to be used as a monitor.

The proposed methodology highlights how particular attention must be paid to the choice of the characteristic parameters of the window, specifically, its time length and sampling time. The results obtained in the final part of the paper show how, although in absolute value the result is influenced by this choice, the trends of the cumulative damage, as well as of the instantaneous one and of the DES, are very similar to different window parameters.

5 ACKNOWLEDGEMENTS

This research activity was financed by Italian PRIN funding source (Research Projects of National Interest - Progetti di Ricerca di Interesse Nazionale) by a financed project entitled SOFTWIND (Smart Optimized Fault-Tolerant WIND turbines).

6 REFERENCES

[1] Ashmore, S.C., Piersol, A.G., Witte, J.J. (1992). Accelerated service life testing of automotive vehicles on a test course. *Vehicle System Dynamics*, vol. 21, no. 2, p. 89-108, **DOI:10.1080/00423119208969004**.

[2] Liu, J., Wang, Y., Li, W. (2010). Simplified fatigue durability assessment for rear suspension structure. *International Journal of Automotive Technology*, vol. 11,. p. 659-664, **DOI:10.1007/s12239-010-0078-1**.

[3] Gao, Q., Wang, Y., Zhang, X. (2011). Prediction of aeronautic rescue mechanism under random vibration based on sample approach. *Zhongguo Jixie Gongcheng/China Mechanical Engineering*, vol. 22, vol. 2, p. 162-165.

[4] Wang, Y. (2010). Spectral fatigue analysis of a ship structural detail - A practical case study. *International Journal of Fatigue*, vol. 32, no. 2, p. 310-317, **DOI:10.1016/j.ijfatigue.2009.06.020**.

[5] Corradini, M.L., Ippoliti, G., Orlando, G. (2018). Fault-tolerant sensorless control of wind turbines achieving efficiency maximization in the presence of electrical faults. *Journal*

of the Franklin Institute, vol. 355, no. 5, p. 2266-2282, **DOI:10.1016/j.jfranklin.2018.01.003**.

[6] Braccesi, C., Cianetti, F., Tomassini, L. (2016). An innovative modal approach for frequency domain stress recovery and fatigue damage evaluation. *International Journal of Fatigue*, vol. 91, p. 382-396, **DOI:10.1016/j.ijfatigue.2016.02.028**.

[7] Braccesi, C., Morettini, G., Cianetti, F., Palmieri, M. (2018). Development of a new simple energy method for life prediction in multiaxial fatigue. *International Journal of Fatigue*, vol. 112, p. 1-8, **DOI:10.1016/j.ijfatigue.2018.03.003**.

[8] Carpinteri, A., Spagnoli, A., Vantadori, S. (2017). A review of multiaxial fatigue criteria for random variable amplitude loads. *Fatigue & Fracture of Engineering Materials & Structures*, vol. 40, no. 7, p. 1007-1036, **DOI:10.1111/ffe.12619**.

[9] Braccesi, C., Cianetti, F., Lori, G., Pioli, D. (2014). Evaluation of mechanical component fatigue behavior under random loads: Indirect frequency domain method. *International Journal of Fatigue*, vol. 61, p. 141-150, **DOI:10.1016/j.ijfatigue.2013.11.017**.

[10] Łagoda, T., Macha, E., Niesłony, A. (2004). Comparison of the rain flow algorithm and the spectral method for fatigue life determination under uniaxial and multiaxial random loading. *Journal of ASTM International*, vol. 1, 8, p. 1-13, **DOI:10.1520/JAI19031**.

[11] Braccesi, C., Cianetti, F., Lori, G., Pioli, D. (2015). Random multiaxial fatigue: A comparative analysis among selected frequency and time domain fatigue evaluation methods. *International Journal of Fatigue*, vol. 74, p. 107-118, **DOI:10.1016/j.ijfatigue.2015.01.003**.

[12] Benasciutti, D., Sherratt, F., Cristofori, A. (2016). Recent developments in frequency domain multi-axial fatigue analysis. *International Journal of Fatigue*, vol. 91, p. 397-413, **DOI:10.1016/j.ijfatigue.2016.04.012**.

[13] Braccesi, C., Cianetti, F., Landi, L. (2005). Random loads fatigue: The use of spectral methods within multibody simulation. *Proceedings of the ASME International Design Engineering Technical Conferences and Computers and Information in Engineering Conference*, vol. 1, p. 1735-1745, **DOI:10.1115/DETC2005-84453**.

[14] Preumont, A., Piefort, V. (1994). Predicting random high-cycle fatigue life with finite elements. *Journal of Vibration and Acoustics, Transactions of the ASME*, vol. 116, no. 2, p. 245-248, **DOI:10.1115/1.2930420**.

[15] Braccesi, C., Cianetti, F. (2005). A procedure for the virtual evaluation of the stress state of mechanical systems and components for the automotive industry: Development and experimental validation. *Proceedings of the Institution of Mechanical Engineers, Part D: Journal of Automobile Engineering*, vol. 219, no. 5, p. 633-643, **DOI:10.1243/095440705X11040**.

[16] Collins, J.A. (1981). *Failure of Materials in Mechanical Design*, Wiley, New York.

[17] Murakami, Y., Morita, T., Mineki, K. (1997). Development and application of super-small size strain history recorder based on rainflow method. *Journal of the Society of Materials Science Japan*, vol. 46, no. 10, p. 1217-1221, **DOI:10.2472/jsms.46.1217**. (in Japanese)

[18] Braccesi, C., Cianetti, F., Moretti, M., Rossi, G. (2015). Random loads fatigue. Experimental approach through thermoelasticity. *Procedia Engineering*, vol. 101, p. 312-321, **DOI:10.1016/j.proeng.2015.02.038**.

[19] Zanarini, A. (2015). Full field experimental modelling in spectral approaches to fatigue predictions. *Proceedings of IFToMM - ICoEV2015 International Conference on Engineering Vibration*, p. 773- 782.

[20] Cetrini, A., Cianetti, F., Corradini, M.L., Ippoliti, G., Orlando, G. (2019). On-line fatigue alleviation for wind turbines by a robust control approach. *International Journal of Electrical Power and Energy Systems*, vol. 109, p. 384-394, **DOI:10.1016/j.ijepes.2019.02.011**.

[21] Cianetti, F., Cetrini, A., Corradini, M.L., Ippoliti, G., Orlando, G. (2018). Dynamic behavior of wind turbines. An on-board evaluation technique to monitor fatigue. *Procedia Structural Integrity*, vol. 12, p. 102-112, **DOI:10.1016/j.prostr.2018.11.103**.

[22] Cianetti, F., Alvino, A., Bolognini, A., Palmieri, M., Braccesi, C. (2018). The design of durability tests by fatigue damage spectrum approach. *Fatigue and Fracture of Engineering Materials and Structures*, vol. 41, no. 4, p. 787-796, **DOI:10.1111/ffe.12686**.

[23] Cianetti, F. (2012). Development of a modal approach for the fatigue damage evaluation of mechanical components subjected to random loads. *SDHM Structural Durability and Health Monitoring*, vol. 8, no. 1, p. 1-29.

[24] Clormann, U., Seeger, T. (1986). Rainflow – HCM – Ein Zählverfahren für Betriebsfestigkeitsnachweise auf werkstoffmechanischer Grundlage. *Stahlbau*, vol. 55, p. 65–117.

[25] ASTM Standard E 1049 (1985). Standard Practices for Cycle Counting in Fatigue Analysis. *ASTM International*, West Conshohocken.

[26] Castellani, F., Astolfi, D., Becchetti, M., Berno, F., Cianetti, F., Cetrini, A. (2018). Experimental and numerical vibrational analysis of a horizontal-axis micro-wind turbine. *Energies*, vol. 11, no. 2, art. ID 456, **DOI:10.3390/en11020456**.

Strojniški vestnik - Journal of Mechanical Engineering 66(2020)10, 567-580
© 2020 Journal of Mechanical Engineering. All rights reserved.
DOI:10.5545/sv-jme.2020.6771
Original Scientific Paper
Received for review: 2020-05-12
Received revised form: 2020-08-19
Accepted for publication: 2020-09-03

Numerical Study of Stress Analysis for the Different Widths of Padding Welds

Adam Kulawik – Joanna Wróbel*
Faculty of Mechanical Engineering and Computer Science, Czestochowa University of Technology, Poland

In the presented study, the cases of regeneration of the element made of C45 steel, using the MAG (Metal Active Gas) method are analysed. The base material is applied to the regeneration process. The analysis of the influence of the padding weld width (0.006 m, 0.01 m, 0.014 m) and the preheating temperature on the phase transformations and effective stresses of the regenerated layer are performed. A non-standard approach to preheating (before each padding weld after the cooling to ambient temperature) is considered. Due to the possibility of simplifying the model from 3D to 2D (symmetry of calculations for long padding welds), calculations were performed using the finite element method in the transverse to the padding direction. Each new padding weld was included as an additional area in the finite element mesh. The developed numerical model includes a temperature model, phase transformations in the liquid and solid states, and the stress model in the elastic-plastic range. The aim of the regeneration is not only to obtain the original geometry of the element, but it is also important that the filler material used (in the considered case identical to the base material) has appropriate properties. These properties largely depend on the phase composition. The used filler material affects not only the hardness, brittleness, and ductility of the material. Its kinetics and changes in the geometry can cause significant stresses and even cracks. Based on the obtained results, it can be concluded that increasing the width of the padding welds causes a decrease in the level of residual effective stress; however, it is technologically difficult to accomplish. The most unfavourable stresses occur in the initial area of the pad welding zone. For lower preheating temperatures and smaller welds, areas with possible cracks are identified. In these cases, lower preheating and tempering should be carried out, which leads to similar energy costs as at higher preheating temperatures. Due to the complex phase transformation process for medium carbon steels and the need for the process parameters control, proper regeneration is possible only in automated workstations.

Keywords: computational mechanics, numerical simulation, padding weld, preheating, strain analysis, stress

Highlights

- *Modelling of multiple mesh geometry in the padding weld process is presented.*
- *The mathematical and numerical models of phenomena occurring during the regeneration process using the welding are applied.*
- *The presented research allows for significantly reducing the number of technological treatments.*
- *The presented paper concerns the shape of the padding weld with an angle of 90°.*
- *The developed numerical model enables the modelling of the various parameters of the regeneration process, such as: preheat temperature, pad geometry, selection of the cooling medium.*

0 INTRODUCTION

The medium C45 carbon steel is suitable for annealing, weldable, and an easy-to-heat treatment. It is a durable steel with significant ductility [1]. C45 steel is used for the moderately loaded and abrasion-resistant machine and equipment parts, such as spindles, axles, shafts, gear wheels, shafts of electric motors, discs, screws, wheel hubs, as well as for moulds in plastics processing. Because the range of regenerated C45 steel parts is extensive, in this paper only the application of new layers to the thin-walled element is analysed. Due to the need to obtain hard coatings, especially during exposure to abrasion, it is necessary to control phase changes during cooling and reheating. Components made of the tested material make it possible to obtain high surface hardness (60 HRC).

The modelling of the multi-pass pad welding process is not a common topic of research papers. Due to the experimental approach for solving these problems, expensive test stands are most often used. For example, thermal analyses obtained from thermovision cameras for process control are used [2]. The data obtained from these analyses can be successfully used to calibrate much cheaper numerical models. Modelling in the field of thermal phenomena in the pad-welding process of a multi-layer or multi-pass is performed even for the complex geometries. However, such models most often refer to the thermal phenomena and compare temperatures obtained from numerical analysis to results obtained from experiments, such as the heat-affected zone (HAZ), hardness, and phase compositions [3]. In the welding or pad welding technology, a highly accurate process temperature is required (at different points of geometry). This approach allows one to, for example,

*Corr. Author's Address: Faculty of Mechanical Engineering and Computer Science, Czestochowa University of Technology, Czestochowa, Poland, joanna.wrobel@icis.pcz.pl

control the grain size as well as the temperature of the start and finish of martensite transformation [4].

Existing works show that the multi-layer thermal cycle for some materials can have a weakening effect on mechanical properties [5]. However, there are contraindications to the use of large cross-sectional welds or padding welds due to unfavourable segregation of dopant and excessive strains.

In pad-welding technology, there are also interesting studies on cladding the parent material with several layers of different materials. However, due to the low thickness of the obtained coating and the depth of HAZ, the stress analysis of these examples cannot be referred to as typical padding welds [6]. Thin layers of padding welds, in cases in which the area of the base material is much larger, are characterized by a small thermal influence on this area. With a significant level of heat dissipation from the padding welds, a martensitic transformation may take place in the case of thin padding layers. Due to the large volume changes during the martensitic transformation, the padding of thin layers is made of materials without phase transformations in a solid state. The residual stress analysis is more often performed by the authors of papers on repair welds, in which the system of the next padding welds has a vertical direction [7] and [8]. In these cases, it is necessary to use the next small cross-sectional layers of padding weld. The use of a large padding weld would be unfavourable, for example, due to higher thermal loads or segregation of the admixture. This fact applies especially to corrosion-resistant materials; however, the influence of phase changes is most often not analysed, which is justified by the fact that such materials have a small change in microstructure, which cannot be said about medium carbon steel analysed in the paper.

Regenerative pad welding is a complex process, and the regeneration of even a geometrically simple surface may involve the necessity of different position and direction of padding welds [9]. In cases of modelling the pad welding processes for large areas with layers of welds with different orientations, three-dimensional (3D) modelling should be performed. It is not possible to perform the analysis only in the cross-section.

The presented research allows one to reduce the number of technological treatments significantly. Due to the need to obtain a specific hardness of the hardfacing for various applications of C45 steel (steel with high carbon equivalent), it is necessary to choose the appropriate preheating temperature range. The ease of formation of the hardening structures of C45 steel during the hardfacing/welding often leads to high stresses and, consequently, cracks. The basic method of preventing cold cracks is preheating, which allows for more flexible transition structures, e.g., bainite [10]. The presented paper concerns the shape of the padding weld with an angle of 90°. In accordance with the requirements of the norm EN ISO 5817 [11] quality D, this weld toe is the worst of the technologically possible solutions. It is also necessary to choose the padding weld width for economic reasons and the obtained stress states (the possibility of surface cracks and on the entire height of the padding weld). In both experimental and numerical studies, the authors most often analyse the shape of the padding welds with a quality level higher than D [12] and [13].

This paper is an extension of the analyses carried out in the research contained in the earlier work [14]. The authors analysed different preheating temperatures for one width of the padding weld. However, they did not discuss the choice of the width of the padding weld for the regeneration process of medium-carbon steel. In this paper, distinct from previous research [14], the application of both smaller and larger padding weld widths (0.006 m, 0.01 m, 0.014 m) was analysed. In order to obtain the correct regenerative padding weld (PW) without any nonconformities 12 cases of combinations of different preheating temperatures and widths of the padding weld are analysed in this paper. The use of numerical simulations reduces the cost of experiments. Using them on a wider scale allows for multi-criteria analysis, based on which we can obtain optimal parameter values. All calculations were performed on a copyrighted application. This model contains appropriate relationships between elements regarding temperature modelling and phase transformation occurring in the range above and below liquidus temperature (T_L) and solidus temperature (T_S). The relationships between the above models and the model of mechanical phenomena are also taken into account.

1 COMPUTATIONAL MODEL

In this paper, the computational model of phenomena taking place during the regeneration of parts is the same as for welding modelling. The model is composed of a module of heat treatment modelling (Fig. 1) and a module taking into account mechanical phenomena (Fig. 3). The phase transformations of austenite to ferrite, pearlite, bainite, martensite and reverse transformations were considered (Fig. 2). The solidification process was analysed in the model. Couplings between the elements of the model were also included.

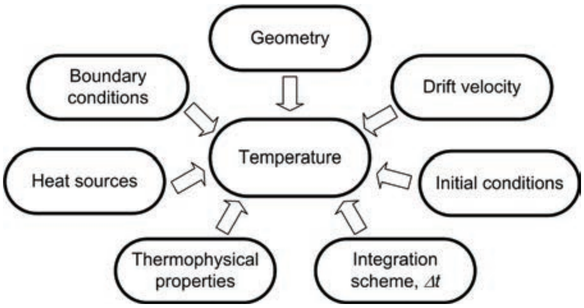

Fig. 1. *Elements of the thermal phenomena model for the regeneration process*

The process of regeneration of steel elements depends mainly on the temperature factor. Therefore, not including the main elements in the heat transfer model can lead to significant simulation errors (Fig. 1). Large temperature changes over time required the solution of the non-steady-state heat transfer equation in the following form:

$$\nabla \cdot (\lambda \nabla T) - \rho C \frac{\partial T}{\partial t} = 0, \qquad (1)$$

where T [K] is the temperature, t [s] the time, λ [W/(mK)] is the thermal conductivity, ρ [kg/m^3] is the mass density, and C [J/(kgK)] is the effective thermal capacity.

The material properties assumed in the computation were dependent on temperature and the phase fractions [15]. The use of constant material properties from temperature causes very large computation errors.

The model of solidification process takes into account the heat of transformation as a change of the effective heat capacity C_{ef} of the material [16] and [17]:

$$C_{ef} = \rho(T) - C(T) - \rho_S L \frac{\partial f_s(T)}{\partial T}\bigg|_{T_S}^{T_L}, \qquad (2)$$

where L [J/(kgK)] is the latent heat of transformation, f_s share of the solid phase, T_L liquidus temperature, and T_S solidus temperature.

In Eq. (2), the f_S is resolved by the lever rule:

$$f_S = f_S(T) = \frac{T_L - T}{T_L - T_S}, \quad T \in [T_L, T_S]. \qquad (3)$$

Changes in the phase composition during the cooling and heating are calculated on the basis of the analysis of continuous cooling transformation (CCT) and continuous heating transformation (CHT) diagrams [18]. The data obtained from the diagrams are input to the macroscopic model, in which the modified Koistinen-Marburger equation was used for the high-rate cooling process [19] and [20]:

$$\tilde{\eta}_\gamma(T,t) = 1 - \exp\left(-\frac{4.60517}{T_{s\gamma} - T_{f\gamma}}\left(T_{s\gamma} - T\right)\right), \qquad (4)$$

where $\tilde{\eta}_\gamma$ is the austenite fraction, $T_{s\gamma}$ is the austenite start temperature, $T_{f\gamma}$ is the austenite finish temperature.

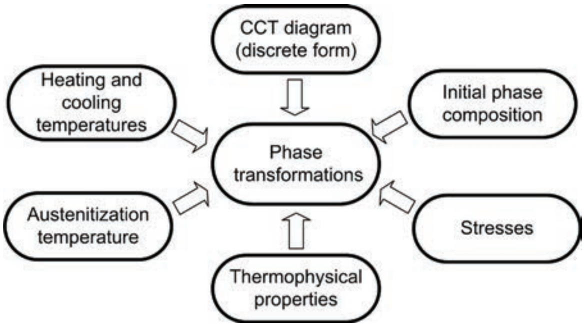

Fig. 2. *Elements of the phase transformations model for the regeneration process*

The phase transformations described by Eq. (4) take place only in the area where the padding welds reheat the element. It is assumed that austenite is the first structure formed after solidification during the cooling process. In the model of phase transformations during the heating, the ferrite and pearlite are treated as a homogeneous mixture.

The phase transformations of the cooling process $\eta_{(i)}(T,t)$ (except for the martensite phase) are determined on the basis of a macroscopic model based on the Avrami equation [21]:

$$\eta_{(i)}(T,t) = \min\left\{\eta_{(i\%)}, \tilde{\eta}_\gamma - \sum_{j \neq i} \eta_j\right\} \cdot \exp\left(-\frac{0.01005}{t_s^{n(T)}} t^{n(T)}\right),$$

$$n(T) = \frac{\ln\left(\dfrac{\ln(1-\eta_f)}{\ln(1-\eta_s)}\right)}{\ln\left(\dfrac{t_f(T)}{t_s(T)}\right)}, \qquad (5)$$

where $\eta_{(i\%)}$ is the final fraction of i phase, η_j is the phase during cooling, $n(T)$ functions depending on the start and finish times of transformation (t_s and t_f).

During the cooling process, the transformations of austenite→ferrite, austenite→pearlite are considered separately.

The kinetics of martensite transformation $\eta_M(T,t)$ for medium-carbon steel is determined on the basis of the Koistinen-Marburger equation [20]:

$$\eta_M\left(T,t\right)= \left(\tilde{\eta}_{\gamma}-\sum_{j\neq M}\eta_i\right)\cdot\left(1-\exp\left(-0.01005\left(M_S-T\right)\right)\right), \quad (6)$$

where M_S is the start temperature of martensite transformation.

When the next padding welds appear, the martensite formed during the cooling process is heated and transformed into tempered martensite $\eta_{TM}(T,t)$. This process is described by the formula:

$$\eta_{TM}(T,t)=\eta_M(1-exp(-\frac{0.01005}{t_s^{n(T)}}t^{n(T)})). \quad (7)$$

The parameters in Eq. (7) describe the transformations of martensite→tempered martensite and are determined based on the equations in the experiment [22].

The phase transformations in the solid-state and temperature changes influence the stress state through the thermal ε^T and structural ε^{Ph} strains described by the following equation:

$$\begin{aligned}\Delta\varepsilon^{TPh}&=\Delta\varepsilon^{T}+\Delta\varepsilon^{Ph},\\ \Delta\varepsilon^{T}&=\Sigma_i\alpha_i(T)\eta_i\Delta T,\\ \Delta\varepsilon^{Ph}&=sign(-\Delta T)\Sigma_i\varepsilon_i^{Ph}(T)\Delta\eta),\end{aligned} \quad (8)$$

where $\alpha_i(T)$ is the coefficients of thermal expansion, $\varepsilon_i^{Ph}(T)$ is the coefficient of strain expansion.

The material properties were taken from the experiment performed for C45 steel [19]. The thermal expansion coefficients and start and end times of tempered martensite were reported in paper [22].

The equilibrium equation, in incremental form, taking into account the influence of temperature on material properties, was used to calculate the stress state. The model did not assume any external forces or the influence of gravity.

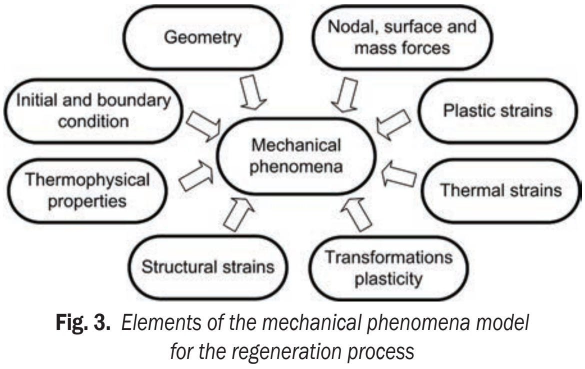

Fig. 3. *Elements of the mechanical phenomena model for the regeneration process*

The elastic deformations are, therefore, the difference between the total, thermal, structural, plastic strains and the transformations plasticity. The influence of temperature on Young's modulus is taken into account.

In the described elastic-plastic model, the isotropic hardening was assumed. The Greenwood-Johnson mechanism in the formation of the transformations' plasticity was also taken into account [23] and [24]. According to the results of the experiments, the temporary yield point is dependent on the temperature and the phase composition (Fig. 4) [25].

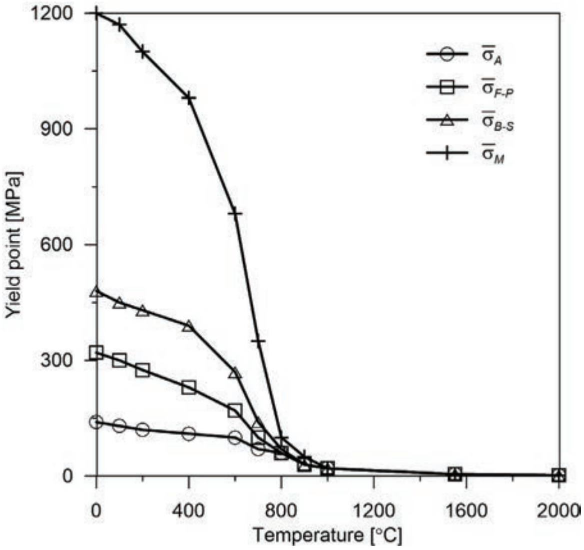

Fig. 4. *Yield point and Young's modulus for particular phases for C45 steel*

All results presented were obtained from the application developed by the authors of this paper. Calculations were made in Visual Studio C++. Linear algebra functions were taken from the Intel® Math Kernel Library [26]. The developed numerical model allows for the modelling of various parameters of the regeneration process, such as preheat temperature, pad geometry, selection of the cooling medium and consideration of heat dissipation by the regeneration station.

2 SIMULATION EXAMPLE

In numerical simulations, it was assumed that the tested plate made of medium carbon steel was a regenerated multipath by applying the next padding welds. In this paper, it was simplified so that the process can be approximated by a 2D model by analysing the cross-section of the element (across the

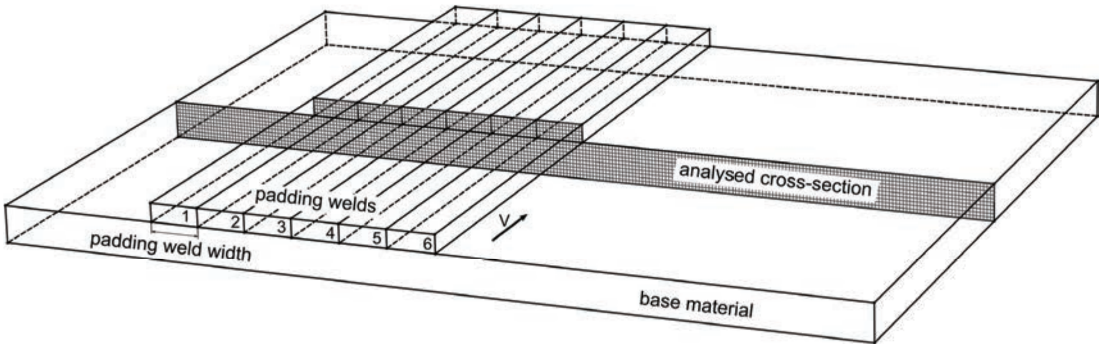

Fig. 5. *Overview figure for analysis No. 3*

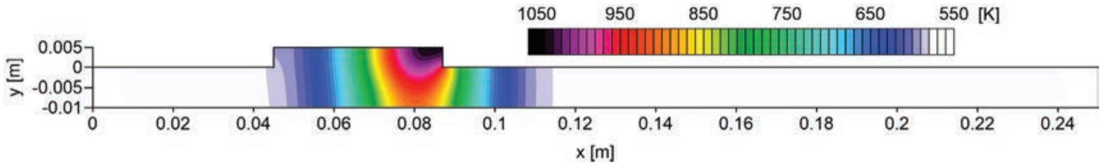

Fig. 6. *The temperature field [K] for the third padding weld of width 0.014 m (T_0 = 573 K) after time t = 9 s*

PW) (Fig. 5). Because the geometry of the padding weld is characterized by a significant predominance of length over width and usually a quite high pad welding speed, critical data concerning stresses, for example, can be obtained mainly from the cross-section. Pad welding with a single path (at one time) and starting subsequent paths after reaching a relatively low temperature of the previous padding weld additionally ensures the correctness of the analysed cross-section. The width of the analysed plate was 0.25 m, the thickness 0.01 m, while the padding weld height was 0.005 m (Fig. 6). Three cases were considered for a different padding weld width: 0.006 m, 0.01 m and 0.014 m (Table 1). To ensure a similar amount of welded material, it was adopted that the PW was composed by the 14 beads for the first case, 8 beads for the second, and 6 beads for the third. In all the analysed cases, the first padding weld is located 0.045 m to the edge. The geometry of the PW is approximated by a quads element (Fig. 5). Finite element mesh with quads elements and bilinear approximation was used for calculations [27]. The padding weld element was discredited by 250 elements in length and 10 in height (element size 0.001 × 0.001). Each padding weld was approximated with finite elements of the same size: analysis No. 1: 6 × 5, analysis No. 2: 10 × 5 and analysis No. 3: 14 × 5 (Fig. 5). According to the welding standard ISO 5817 [11] the weld toe equally 90 ° was adopted (limit for imperfections for quality level D). The technological process was simplified; it was assumed that the padding weld appears as a rectangular element with a given height and width (constant height, 3 cases of width) and an initial temperature of 1800 K (Fig. 7). The constant initial temperature of the PW and its different cross-sectional area were assumed; from the technological side, it requires the delivery of different amounts of heat (different parameters of the welding arc).

For all analysed padding weld widths, the four preheating temperatures: T_0 = 293 K, 373 K, 473 K, 573 K were considered. The cooling on the boundaries was modelled with the Newton condition (Fig. 6). Air cooling was modelled according to the equation [28]:

$$\alpha_{air} = \begin{cases} 0.0668 \times T, & T_0 < T < 773 \text{ K} \\ 0.231 \times T - 82.1, & T \geq 773 \text{ K} \end{cases}. \tag{9}$$

Table 1. *Numerical research plan*

Analysis No.	Preheating temperature [K]	PW width [m]	Number of PW	Field of the PW area [m^2]
1.1	293	0.006	14	0.00042
1.2	373			
1.3	473			
1.4	573			
2.1	293	0.01	8	0.0004
2.2	373			
2.3	473			
2.4	573			
3.1	293	0.014	6	0.00042
3.2	373			
3.3	473			
3.4	573			

For each case, calculations were performed for many finite element method (FEM) meshes. Each subsequent geometry differed in the formation of one padding weld. The number of simulations depended on the number of PW in each case (Table 1). The assumption of a small value of finite elements defining the padding weld allowed one to observe the changes in the analysed phenomena.

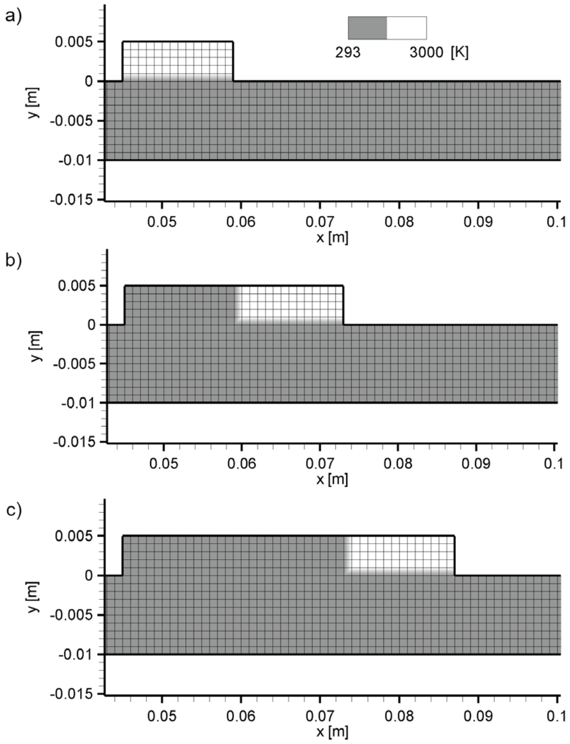

Fig. 7. *Geometry with mesh and initial temperature for the next three padding welds (analysis No. 3): a) one padding weld, b) two padding welds, c) three padding welds*

The appearance of the next PW was dependent on the value of temperature. Subsequent weld passes occurred after reaching the ambient temperature of the previous PW. The next step was to set the preheating temperature for the next padding weld and the whole element. The analysed material for the assumed cooling conditions (after the cooling process) does not contain an austenitic structure. In the model of mechanical phenomena, appropriate degrees of freedom were removed for selected elements; therefore, the model could be solved numerically. The selected nodes and applied zero displacements did not of the obtained stress levels. Due to large changes in material properties, the average values of material properties were determined for each finite element in the mechanical model. These properties depend (among other factors) on temperature level, phase transformations in the solid state, and solidification (Fig. 4).

Each case is a series of a few successive simulations. The model assumes the continuity of values for phase transitions and stress state between successive simulations.

3 RESULTS AND DISCUSSION

One of the main parameters, especially for the materials subject to phase transformations during the regeneration process, is the depth of the heat-affected zone (HAZ) and fusion zone (FZ). Figs. 8 to 10 show the HAZ depth in the base material below the padding weld. The results of calculations for the four preheating temperatures for each of the three widths were presented. The size of the HAZ was determined assuming a temperature of A_{c1} for the steel C45 equal to 1008 K.

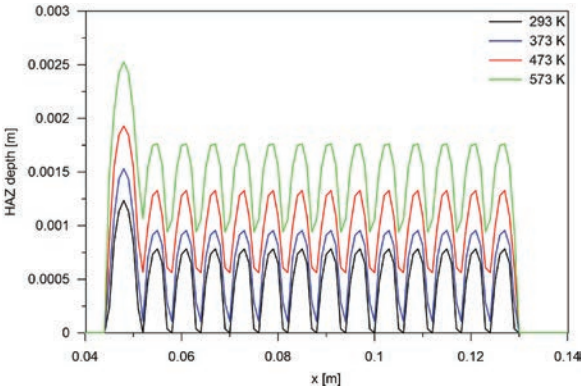

Fig. 8. *Depth of HAZ for padding weld width of 0.006 m*

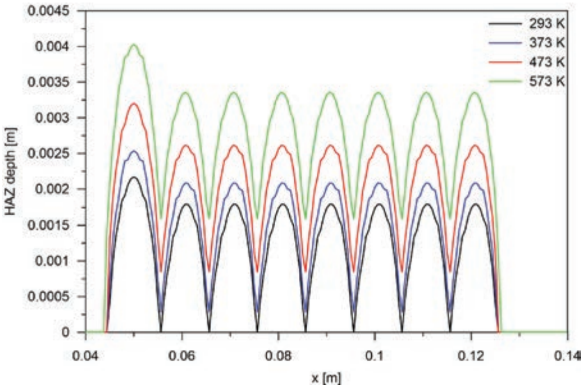

Fig. 9. *Depth of HAZ for padding weld width of 0.01 m*

The change of HAZ depth depending on the preheating temperature in relation to the padding weld width was linearly correlated and increased with the size of the padding weld. In Figs. 8 to 10, it can be observed that the first padding weld causes the deepest HAZ, which is because three walls are cooled by air, and most of the heat is absorbed by the regenerated material. In other cases, contact with the regenerated material was through two walls of the padding weld. The largest difference between the depths of the HAZ was observed for the smallest width of the padding weld (Figs. 8 to 10). In this case, proportionally, the smallest length of the edge is in contact with the regenerated material. According to predictions, the greatest depth of HAZ occurs for the largest volume of the padding weld (Fig. 10). On the basis of the obtained temperature distribution in the area of contact between the padding welds and the base material, the depth of the fusion zone was minimal, and only the nodes of the finite element mesh on the border of the base area exceed the temperature T_L = [illegible] K.

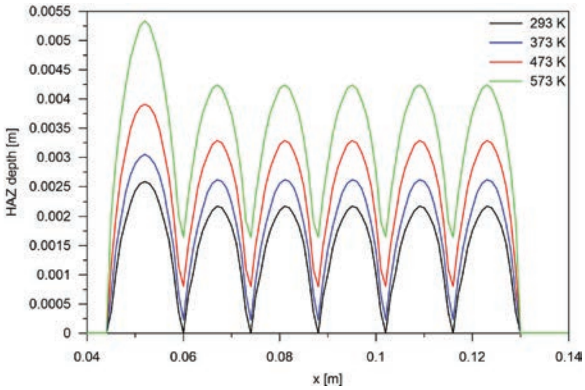

Fig. 10. *Depth of HAZ for padding weld width of 0.014 m*

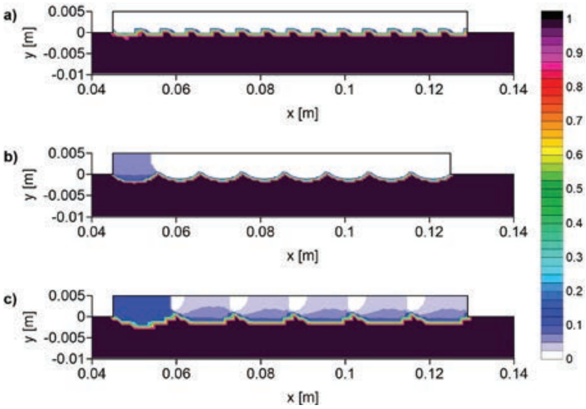

Fig. 11. *Sum of ferrite and pearlite fraction (after process), preheating temperature 293 K and padding weld width of: a) 0.006 m, b) 0.01 m, c) 0.014 m*

It can be observed that for the smallest padding weld for the first two preheating temperatures, the cooling rate exceeds critical velocity (rate of obtaining the quenching phase), which also applies to the first

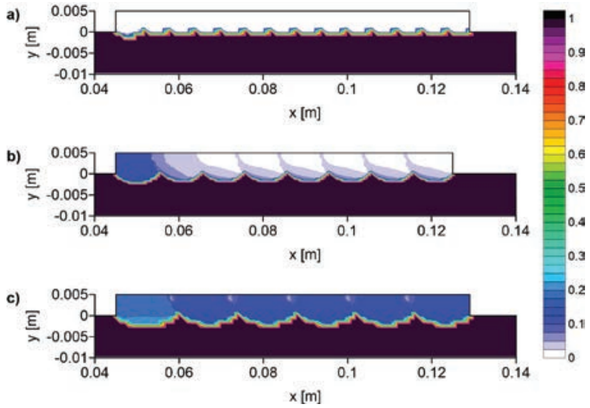

Fig. 12. *Sum of ferrite and pearlite fraction (after process), preheating temperature 373 K and padding weld width of: a) 0.006 m, b) 0.01 m, c) 0.014 m*

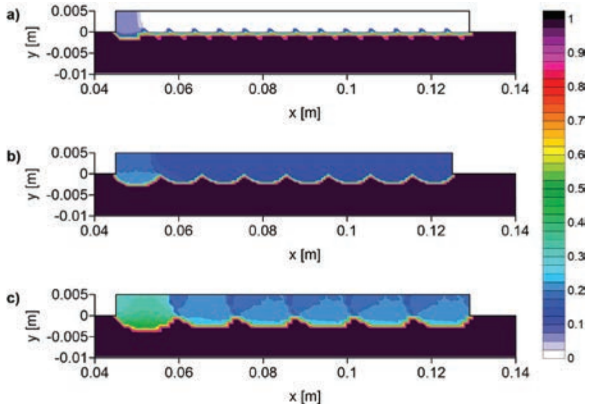

Fig. 13. *Sum of ferrite and pearlite fraction (after process), preheating temperature 473 K and padding weld width of: a) 0.006 m, b) 0.01 m, c) 0.014 m*

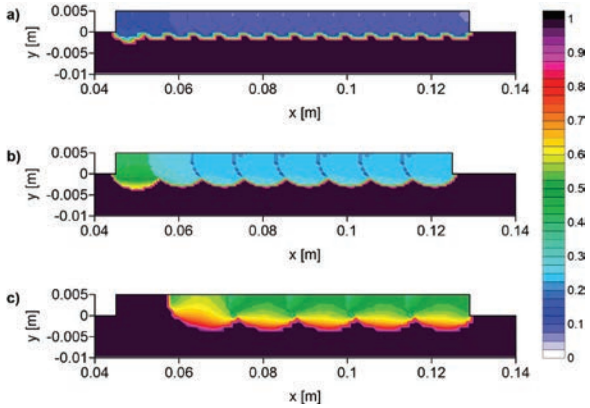

Fig. 14. *Sum of ferrite and pearlite fraction (after process), preheating temperature 573 K and padding weld width of: a) 0.006 m, b) 0.01 m, c) 0.014 m*

padding weld, for which the cooling is the slowest (the longest air-cooled boundary) (Figs. 11a and 12a). With the increase of the PW width and the preheating temperature, the cooling rate decreases to such a value that in the last case 34 (see Table 1, Fig. 14) the first padding weld is composed only of a ferrite-pearlite mixture, whereas the others only in about 30 % (Figs. 11 to 14).

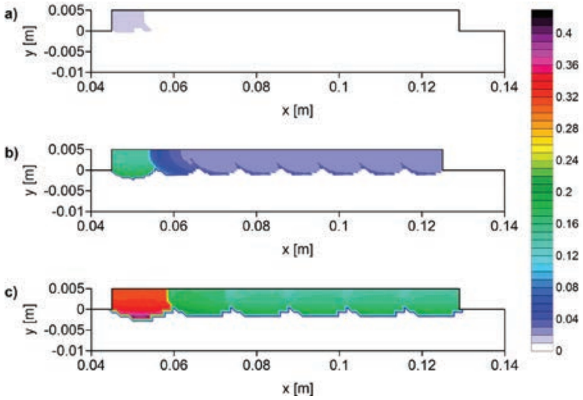

Fig. 15. *Bainite fraction (after process), preheating temperature 293 K and padding weld width of: a) 0.006 m, b) 0.01 m, c) 0.014 m*

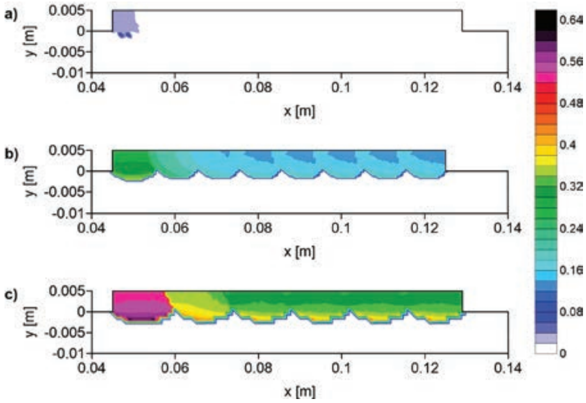

Fig. 16. *Bainite fraction (after process), preheating temperature 373 K and padding weld width of: a) 0.006 m, b) 0.01 m, c) 0.014 m*

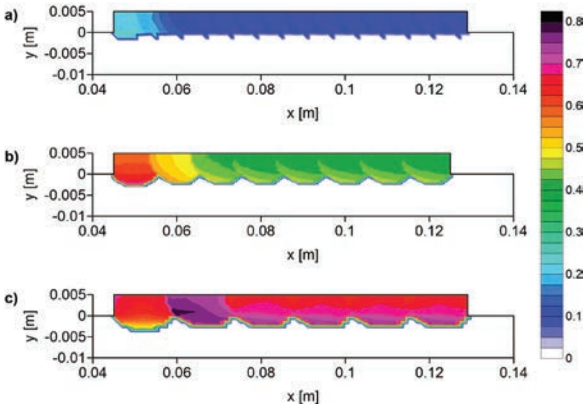

Fig. 17. *Bainite fraction (after process), preheating temperature 473 K and padding weld width of: a) 0.006 m, b) 0.01 m, c) 0.014 m*

The big differences in the distribution of the bainite structure, between the first and the other padding weld, were obtained. It was due to the

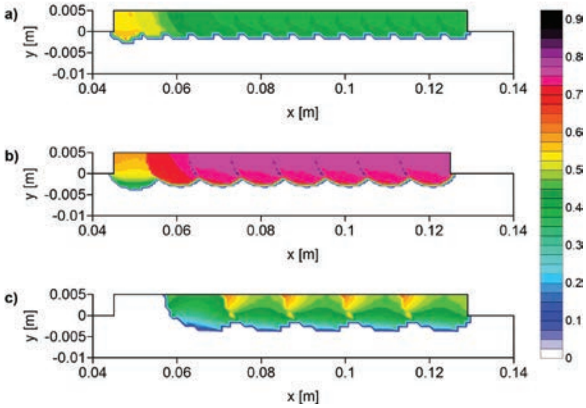

Fig. 18. *Bainite fraction (after process), preheating temperature 573 K and padding weld width of: a) 0.006 m, b) 0.01 m, c) 0.014 m*

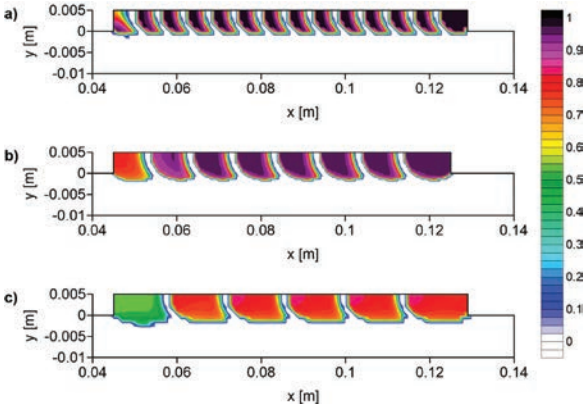

Fig. 19. *Martensite fraction (after process), preheating temperature 293 K and padding weld width of: a) 0.006 m, b) 0.01 m, c) 0.014 m*

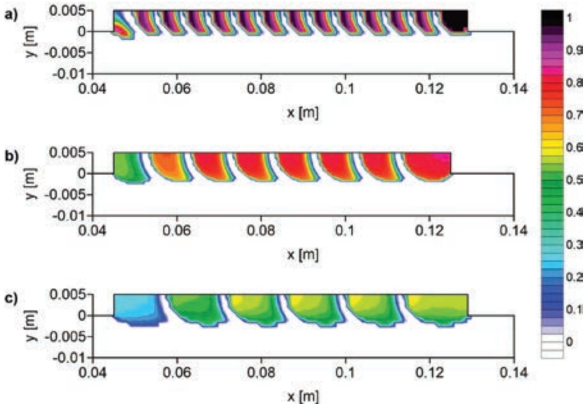

Fig. 20. *Martensite fraction (after process), preheating temperature 373 K and padding weld width of: a) 0.006 m, b) 0.01 m, c) 0.014 m*

different cooling conditions. The amount of bainite increases with the increase of the preheating temperature in the range 29 K to 4 K and the padding weld width. The amount of bainite structure increases with the change of the PW width from 0.006 m to 0.01 m. Whereas for the width of 0.014 m (Figs.

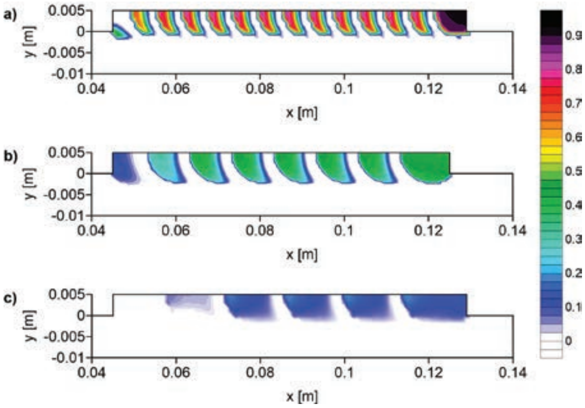

Fig. 21. *Martensite fraction (after process), preheating temperature 473 K and padding weld width of: a) 0.006 m, b) 0.01 m, c) 0.014 m*

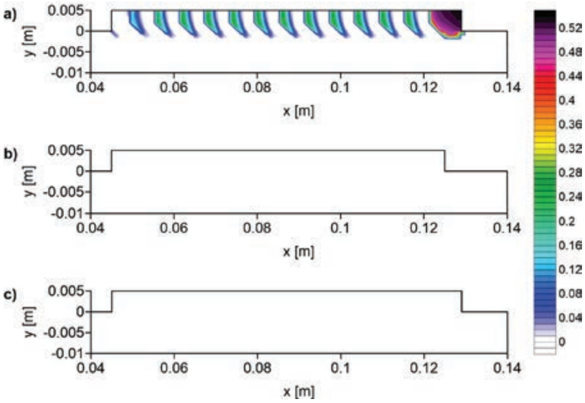

Fig. 22. *Martensite fraction (after process), preheating temperature 573 K and padding weld width of: a) 0.006 m, b) 0.01 m, c) 0.014 m*

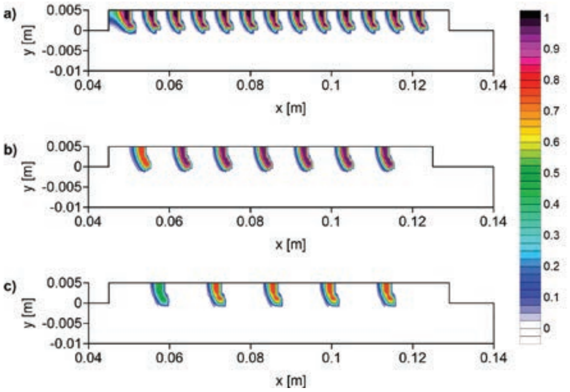

Fig. 23. *Tempered martensite (after process), preheating temperature 293 K and padding weld width of: a) 0.006 m, b) 0.01 m, c) 0.014 m*

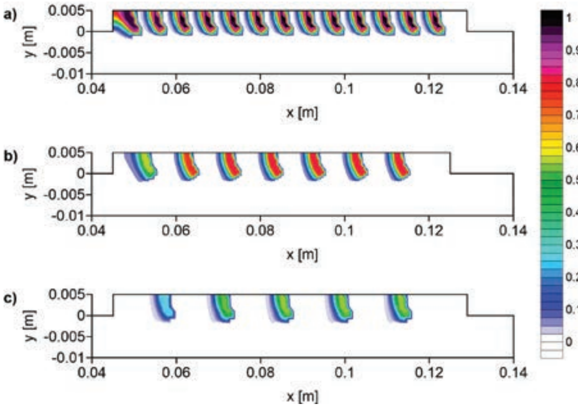

Fig. 24. *Tempered martensite fraction (after process), preheating temperature 373 K and padding weld width of: a) 0.006 m, b) 0.01 m, c) 0.014 m*

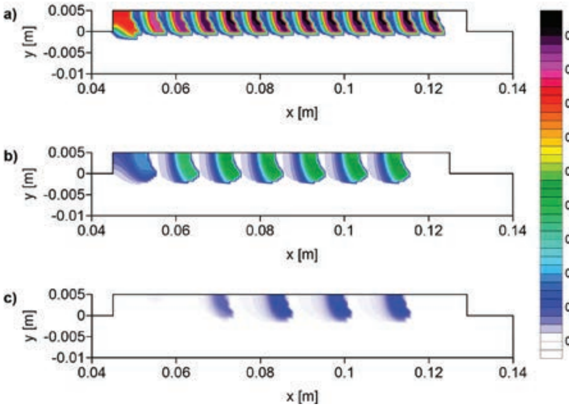

Fig. 25. *Tempered martensite fraction (after process), preheating temperature 473 K and padding weld width of: a) 0.006 m, b) 0.01 m, c) 0.014 m*

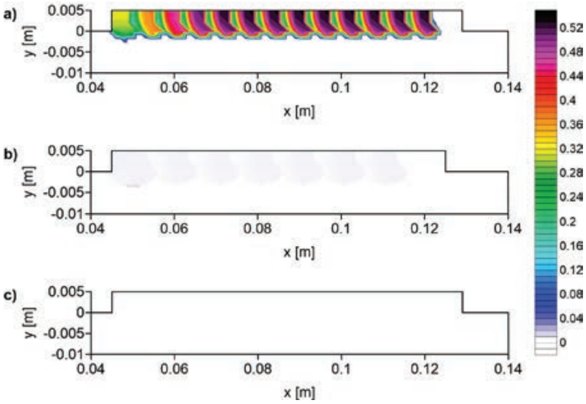

Fig. 26. *Tempered martensite fraction (after process), preheating temperature 573 K and padding weld width of: a) 0.006 m, b) 0.01 m, c) 0.014 m*

5 to 8) influence of the heat of the padding weld on the shape of the cooling curve on the CCT diagram, and thus a greater share of the ferrite-pearlite structure was noted (Figs. 11 to 4). The high repeatability of the distribution of phase composition in the central part of the material occurs for all cases.

The composition of the quenching phases (bainite, martensite, and tempered martensite; Table 2) indicates the rightness of using preheating in order to control the shape of cooling curves and the ferrite-pearlite structure (Figs. 9 to 26). The control of cooling curves, especially for hardly weldable materials, may cause a lower value of effective stress and in consequence elimination of cold cracks. As indicated by the results presented in Tables 2 and 3, the application of preheating at the level of 4 K and 5 K causes a much higher fraction of the bainite structure, which consequently reduces the yield point and the maximum values of effective stresses. This difference is especially visible for small volumes of the padding welds, where between the highest and the lowest preheating temperature, the difference in effective stresses reaches 6 %. It is less visible for wider padding welds, which, due to their volume, cool down more slowly (the difference between the bainite fraction for the smallest and the largest width of the padding weld without preheating temperature is over 0 %). The use of preheating only increases the fraction of bainite at the expense of martensite, until a ferrite-pearlite structure appears during cooling.

Table 2. *The maximum values of the quenching structures*

Analysis No.	Bainite [%]	Martensite [%]	Tempered martensite [%]
1.1	1.82	99.00	99.00
1.2	9.49	97.89	97.87
1.3	25.25	90.62	90.54
1.4	59.25	53.58	53.26
2.1	20.12	96.58	96.58
2.2	37.07	82.80	82.83
2.3	72.21	46.53	46.57
2.4	85.52	0.42	1.13
3.1	41.89	84.72	79.80
3.2	61.17	60.42	56.16
3.3	79.99	18.14	12.77
3.4	63.60	0	0

The distribution of plastic strains (Figs. 3 to 3) correctly indicates the areas where cracks can occur. Including recrystallization and loss of stress during heating significantly changes the results of calculations. The plastic strains were taken into account only below 7 % of the solidus temperature of C4 steel. The highest amount of tempered martensite occurred in the structure with a width of 0.006 m and a preheating temperature of 29 K (Fig. 23).

Table 3. *Summary of the calculation results for the considered cases after the regeneration process*

Analysis No.	Maximum effective stresses [MPa]	Maximum effective plastic strain	Yield point [MPa]
1.1	947.00	0.0066	314.12–1217.05
1.2	862.90	0.0057	312.68–1202.54
1.3	876.54	0.0044	312.12–1132.65
1.4	577.56	0.0044	311.87–844.20
2.1	827.53	0.0070	313.42–1210.20
2.2	605.72	0.0055	312.51–1088.32
2.3	659.55	0.0054	312.07–804.80
2.4	466.05	0.0057	294.01–472.88
3.1	451.99	0.0051	313.11–1089.22
3.2	421.45	0.0040	312.38–886.11
3.3	416.08	0.0034	312.00–582.29
3.4	403.88	0.0033	310.48–434.41

The stress distributions for the first three preheating temperatures, with the assumed cooling conditions, were similar to the maximum values (Figs. 27 to 29). The influence of the padding weld width on the stress level was observed. The differences between the maximum values of effective stresses for the case without preheating even reach 00 % (analysis No. 3.1 and 1.1). This difference decreases for the analysis No. 3 to less than 5 % (Table 3). The most favourable was the distribution for a 0.04 m of padding width. The effective stress value for temperature 5 K was caused by the yield point value for analysed material (Table 3). The yield point value was due to the high proportion of the ferrite-pearlite structure in relation to martensite. Reduction in the level of effective stresses with an increased number of padding welds was observed. Along with the increase of the padding weld width, the stresses were initialized deeper in the base material (Figs. 27 to 0).

The distribution and kinetics of phase transformations in the solid state determines the distribution of the yield point. Higher values of yield point occurred for areas with the highest cooling rate and martensite transformation (Table 3). The assumed yield point of tempered martensite, at the level of bainite, were caused by the reduction of the yield point in the interpass areas. The temperature-dependent yield point values for the individual phases are shown in Fig. 4.

The level of plastic strains decreased when the preheating temperature and padding weld width were increased. The greatest plastic strains occurred for the smallest width of the padding weld. The plastic strains increase towards the padding weld surface. They decrease with the width of the padding weld (Table 3). The distribution of plastic strains suggests the formation of cracks between welds, especially for smaller widths of the padding weld and a lower preheating temperature. The influence of the

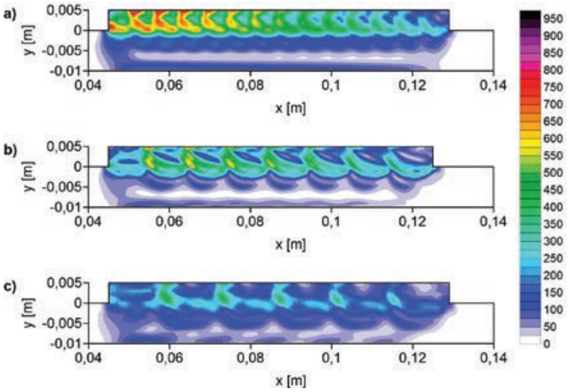

Fig. 27. *Effective stresses [MPa] (after process), preheating temperature 293 K and padding weld width of: a) 0.006 m, b) 0.01 m, c) 0.014 m*

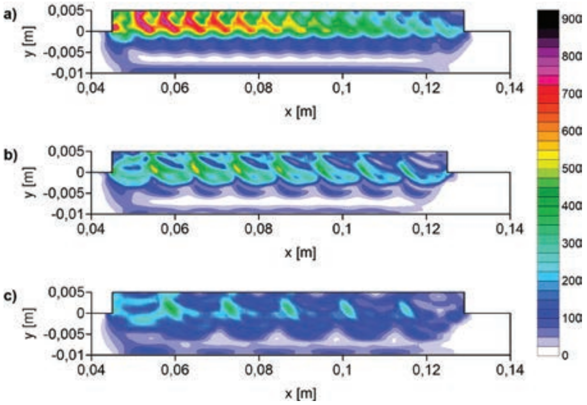

Fig. 28. Effective stresses [MPa] (after process), preheating temperature 373 K and padding weld width of: a) 0.006 m, b) 0.01 m, c) 0.014 m

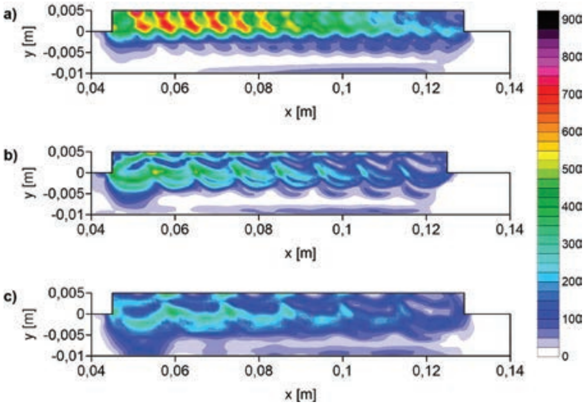

Fig. 29. Effective stresses [MPa] (after process), preheating temperature 473 K and padding weld width of: a) 0.006 m, b) 0.01 m, c) 0.014 m

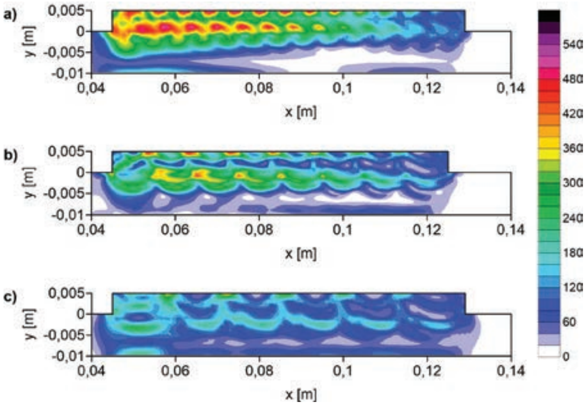

Fig. 30. *Effective stresses [MPa] (after process), preheating temperature 573 K and padding weld width of: a) 0.006 m, b) 0.01 m, c) 0.014 m*

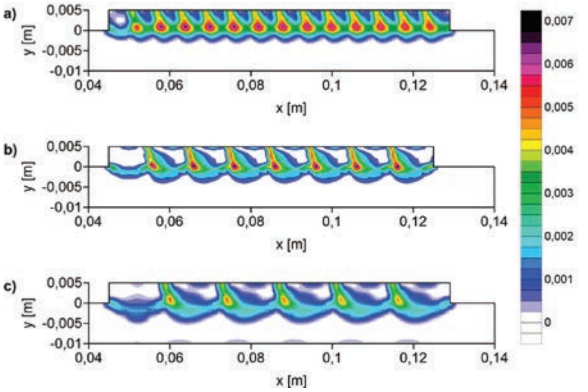

Fig. 31. *Effective plastic strain (after process), preheating temperature 293 K and padding weld width of: a) 0.006 m, b) 0.01 m, c) 0.014 m*

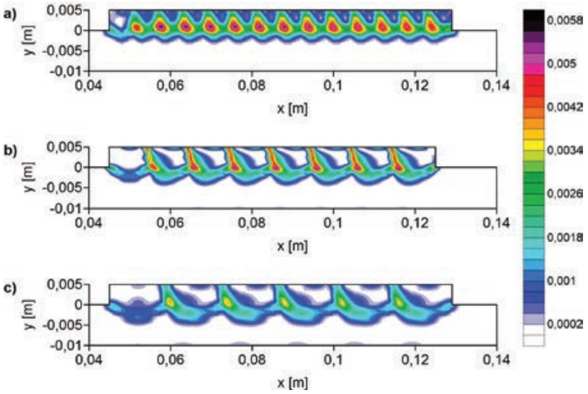

Fig. 32. *Effective plastic strain (after process), preheating temperature 373 K and padding weld width of: a) 0.006 m, b) 0.01 m, c) 0.014 m*

martensite tempering and recrystallization process was observed (Figs. 31 to 34).

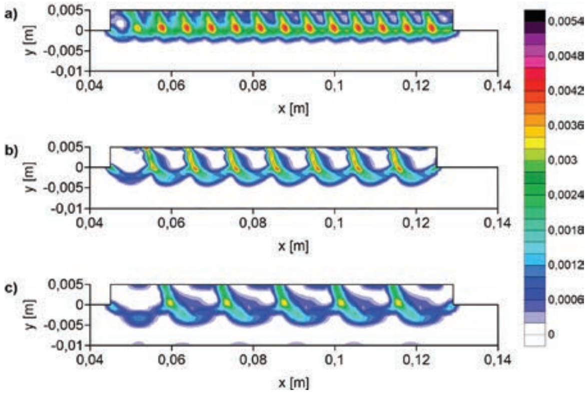

Fig. 33. *Effective plastic strain (after process), preheating temperature 473 K and padding weld width of: a) 0.006 m, b) 0.01 m, c) 0.014 m*

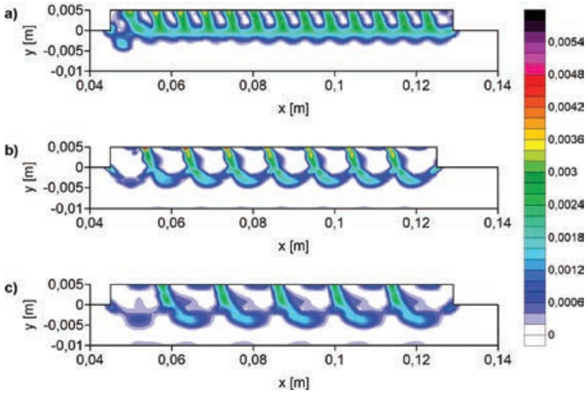

Fig. 34. *Effective plastic strain (after process), preheating temperature 573 K and padding weld width of: a) 0.006 m, b) 0.01 m, c) 0.014 m*

4 CONCLUSIONS

In the present paper, the influence of padding weld width and preheating temperature on phase transformations and stresses of the regenerated layer were analysed. The obtained results indicate that the use of preheating in order to change the shape of cooling curve, even until complete cooling, makes it possible to control the fraction of individual phases. However, the economic analysis of this process indicates that it would be more convenient, cheaper and more effective to control cooling conditions than heating. The obtained results give answers to questions about structures in the regeneration process, during which we did not have full control over the process conditions (the process was not controlled by the interpass temperature). This is applicable if the cooling process has not been stopped when the interpass temperature is reached at the level of preheating temperature only at the level of the ambient temperature. An example of such a process may be the performance of the next long padding welds with a long technological break, where the beginning of the padding weld is cooled to ambient temperature before the next pad.

On the basis of the presented results and taking into account the stress distribution, it can be concluded that the use of the widest padding weld is highly advantageous. The use of preheating for analysis No. 3 is not required to obtain a hard but also brittle surface (high fraction of martensite). The selection of the optimal preheating value is possible only when we define the conditions under which the pad welding surface will work. If we want to obtain a large amount of bainite structure and small amount of martensite, the lowest suggested preheating is between 373 K and 473 K. Obtaining areas of tempered martensite is beneficial for regenerated surfaces. However, due to the specificity of pad welding, the area of tempered martensite cannot, especially for small padding welds, reach too deep into the pad welding without additional treatment. Therefore, during pad welding, we should focus on obtaining a bainite structure with the addition of martensite, whereas the area of tempered martensite treat as an additional advantage. However, it should be noted that in choosing large cross-sectional padding welds, problems may occur with the segregation of the admixture, the influence of the temperature of the padding weld on the base material or the noticeable higher values of plastic strains and the stresses inside the regenerated material.

The results obtained from the analysis of the phase transformations in the solid state and stresses suggest that it is unreasonable to use heating and cooling sequentially to ambient temperature; this is also not economically viable. Therefore, it is reasonable to consider the case in which the next padding weld is applied when the temperature of the previous padding has reached the preheating temperature. The differences between the obtained distributions of plastic strains result from the influence of the preheating temperature, before each padding weld, on the cooling rate.

As previously mentioned, the analysed material is very difficult to regenerate. The presented analysis allows one to assess whether there may be defects after the regeneration process in the absence of appropriate supervision. With unfavourable distribution of structural and thermal strains, cracks may occur in the cross-section of the PW (this would require a 3D analysis).

In this paper, a geometrically simple case that can be easily referred to in experimental research or other computer simulation models was considered. However, in practical applications, where the shape of the pad welding object may be very different, the presented results cannot be transferred.

5 ACKNOWLEDGEMENTS

The research has been performed within a statutory research BS/PB-1 00- 30/ 2020/P.

6 REFERENCES

[1] Odebiyi, O.S., Adedayo, S.M., Tunji, L.A., Onuorah, M.O. (2019). A review of weldability of carbon steel in arc-based welding processes. *Cogent Engineering*, vol. 6, no. 1, p. 1609180, **DOI:10.1080/23311916.2019.1609180**.

[2] Nowacki, J., Wypych, A. (2010). Application of thermovision method to welding thermal cycle analysis. *Journal of Achievements in Materials and Manufacturing Engineering*, vol. 40, no. 2, p. 131-137.

[3] Hu, Z., Qin, X., Shao, T. (2017). Welding thermal simulation and metallurgical characteristics analysis in WAAM for 5CrNiMo hot forging die remanufacturing. *Procedia Engineering*, vol. 207, p. 2203-2208, **DOI:10.1016/j.proeng.2017.10.982**.

[4] Zhou, X., Liu, Y., Liu, C., Yu, L., Li, H. (2018). Austenitizing temperature effects on the martensitic transformation, microstructural characteristics, and mechanical performance of modified ferritic heat-resistant steel. *Metallurgical and Materials Transactions A*, vol. 49, p. 3525-3538, **DOI:10.1007/s11661-018-4723-z**.

[5] Chen, X.Z., Huang, Y.M., Shen, Z., Chen, J., Lei, Y.C., Zhou, J.Z. (2013). Effect of thermal cycle on microstructure and mechanical properties of CLAM steel weld CGHAZ. *Science and Technology of Welding and Joining*, vol. 18, no. 4, p. 272-278, **DOI:10.1179/1362171812Y.0000000095**.

[6] Marques, M.J., Ramasamy, A., Batista, A.C., Nobre, J.P., Loureiro, A. (2015). Effect of heat treatment on microstructure and residual stress fields of a weld multilayer austenitic steel clad. *Journal of Materials Processing Technology*, vol. 222, p. 52-60, **DOI:10.1016/j.jmatprotec.2015.03.004**.

[7] Jiang, W.C., Wang, B.Y., Gong, J.M., Tu, S.T. (2011). Finite element analysis of the effect of welding heat input and layer number on residual stress in repair welds for a stainless steel clad plate. *Materials & Design*, vol. 32, no. 5, p. 2851-2857, **DOI:10.1016/j.matdes.2010.12.037**.

[8] Liu, S., Sun, J., Wei, F., Lu, M. (2018). Numerical simulation and experimental research on temperature and stress fields in TIG welding for plate of RAFM steel. *Fusion Engineering and Design*, vol. 136, part A, p. 690-693, **DOI:10.1016/j.fusengdes.2018.03.058**.

[9] Jeffus, L. (2020) *Welding: Principles And Applications* (9th ed.). Cengage Learning, Boston.

[10] Kuzniecow, V.D., Popowicz, P.W. (2011). Problems of restoration medium and high-carbon steels by hard-facing. *Welding Technology Review*, vol. 83, no. 10, p. 4-7, **DOI:10.26628/wtr.v83i10.460**. (in Polish)

[11] ISO 5817 (2014). *Welding - Fusion-Welded Joints in Steel, Nickel, Titanium and Their Alloys (Beam Welding Excluded) - Quality Levels for Imperfections*. International Organization for Standardization, Geneva.

[12] Pfeifer, T., Czwórnóg, B. (2015). The effect of plasma surfacing parameters on the geometry and structure of overlay welds. *Institute of Welding Bulletin*, vol. 59, no. 4, p. 6-14, **DOI:10.17729/ebis.2015.4/1**.

[13] Winczek, J. (2017). Modeling of temperature field during multi-pass GMAW surfacing or rebuilding of steel elements taking into account the heat of the deposit metal. *Applied Sciences*, vol. 7, no. 1, p. 6, **DOI:10.3390/app7010006**.

[14] Bęczkowski, R., Wróbel, J., Kulawik, A. (2017). The use of numerical modelling to determine the conditions of regeneration of medium carbon steel. *Archives of Metallurgy and Materials*, vol. 62, no. 4, p. 2223-2230, **DOI:10.1515/amm-2017-0328**.

[15] Wróbel, J., Kulawik, A. (2018). Analysis of the influence of material parameters of the numerical model on the obtained shape of the heat affected zone for the TIG heating process. *AIP Conference Proceedings*, vol. 1978, p. 470029, **DOI:10.1063/1.5044099**.

[16] Bokota, A. (2012). *Modelling of Hardening Tool Steels: Thermal Phenomena, Phase Transformations, Mechanical Phenomena*. Wydawnictwo Politechniki Częstochowskiej, Czestochowa. (in Polish)

[17] Piekarska, W., Kubiak, M., Bokota, A. (2011). Numerical simulation of thermal phenomena and phase transformations in laser-arc hybrid welded joints. *Archives of Metallurgy and Materials*, vol. 56, no. 2, p. 409-421, **DOI:10.2478/v10172-011-0044-6**.

[18] Wever, F., Rose, A. (1961). *Atlas zur Wärmebehandlung von Stähle, I Zeit Temperatur Umwandlungs Schaubilder*, Verlag Stahleisen, Düsseldorf.

[19] Bokota, A., Kulawik, A. (2007). Model and numerical analysis of hardening process phenomena for medium-carbon steel. *Archives of Metallurgy and Materials*, vol. 52, no. 2, p. 337-346.

[20] Koistinen, D.P., Marburger, R.E. (1959). A general equation prescribing the extent of the austenite-martensite transformation in pure iron-carbon alloys and plain carbon steels. *Acta Metallurgica*, vol. 7, no. 1, p. 59-60, **DOI:10.1016/0001-6160(59)90170-1**.

[21] Avrami, M. (1939). Kinetics of phase change. I General theory. *Journal of Chemical Physics*, vol. 7, no. 12, p. 1103-1112, **DOI:10.1063/1.1750380**.

[22] Winczek, J., Kulawik, A. (2015). Dilatometric and hardness analysis of C45 steel tempering with different heating-up rates. *Metalurgija*, vol. 51, no. 1, p. 9-12.

[23] Fischer, F.D., Reisner, G., Werner, E., Tanaka, K., Cailletaud, G., Antretter, T. (2000). A new view on transformation induced plasticity (TRIP). *International Journal of Plasticity*, vol. 16, no. 7-8, p. 723-748, **DOI:10.1016/S0749-6419(99)00078-9**.

[24] Taleb, L., Cavallo, N., Waeckel, F. (2001). Experimental analysis of transformation plasticity. *International Journal of Plasticity*, vol. 17, no. 1, p. 1-20, **DOI:10.1016/S0749-6419(99)00090-X**.

[25] Coret, M., Combescure, A. (2002). A mesomodel for numerical simulation of the multiphasic behavior of materials under anisothermal loading (application to two low-carbon steels). *International Journal of Mechanical Sciences*, vol. 44, no. 9, p. 1947-1963, **DOI:10.1016/S0020-7403(02)00053-X**.

[26] Intel® (2020). Math Kernel Library, *from https://software.intel.com/en-us/mkl*, accessed on 28.02.2020.

[27] Zienkiewicz, O.C., Taylor, R.L. (2000). T*he Finite Element Method,* Butterworth-Heinemann, Oxford.

[28] Li, C., Wang, Y., Zhan, H., Han, T., Han, B., Zhao, W. (2010). Three-dimensional finite element analysis of temperatures and stresses in wide-band laser surface melting processing. *Materials & Design*, vol. 31, no. 7, p. 3366-3373, **DOI:10.1016/j.matdes.2010.01.054**.

Strojniški vestnik - Journal of Mechanical Engineering 66(2020)10, 581-590

DOI:10.5545/sv-jme.2020.6883
Original Scientific Paper
Received for review: 2020-07-25
Received revised form: 2020-09-14
Accepted for publication: 2020-09-21

Effect of Thermal Barrier Coating on the Thermal Stress of Gas Microturbine Blades and Nozzles

Oscar Tenango-Pirin[1] – Elva Reynoso-Jardón[1] – Juan Carlos García[2,*] – Yahir Mariaca[1] – Yuri Sara Hernández[3] – Raúl Ñeco[1] – Omar Dávalos[1]

[1] Departamento de Ingeniería Industrial y Manufactura, Universidad Autónoma de Ciudad Juárez, México
[2] Centro de Investigación en Ingeniería y Ciencias Aplicadas, Universidad Autónoma del Estado de Morelos, México
[3] Tecnológico Nacional de México/Campus Pachuca, Pachuca de Soto, Hidalgo, México

Thermal barrier coatings play a key role in the operational life of microturbines because they reduce thermal stress in the turbine components. In this work, numerical computations were carried out to assess new materials developed to be used as a thermal barrier coating for gas turbine blades. The performance of the microturbine components protection is also evaluated. The new materials were 8YSZ, Mg_2SiO_4, $Y_3Ce_7Ta_2O_{23.5}$, and $Yb_3Ce_7Ta_2O_{23.5}$. For testing the materials, a 3D gas microturbine model is developed, in which the fluid-structure interaction is solved using CFD and FEM. Temperature fields and stress magnitudes are calculated on the nozzle and blade, and then these are compared with a case in which no thermal barrier is used. Based on these results, the non-uniform temperature distributions are used to compute the stress levels in nozzles and blades. Higher temperature gradients are observed on the nozzle; the maximum temperature magnitudes are observed in the blades. However, it is found that Mg_2SiO_4 and $Y_3Ce_7Ta_2O_{23.5}$ provided better thermal insulation for the turbine components compared with the other evaluated materials. Mg_2SiO_4 and $Y_3Ce_7Ta_2O_{23.5}$ presented the best performance regarding stress and thermal insulation for the microturbine components.
Keywords: thermal barrier coating, gas microturbine, turbine blade, thermal stress

Highlights
- *An investigation of the effectiveness of novel ceramics for TBC applications is carried out for their use in gas microturbine blades.*
- *The Mg_2SiO_4 and $Y_3Ce_7Ta_2O_{23}$ provided the best performance on thermal insulation under operational environments of the turbine.*
- *The Mg_2SiO_4 and $Y_3Ce_7Ta_2O_{23}$ showed similar thermal and mechanical stress magnitudes on the blades, which were the lowest among the materials studied.*
- *The use of those ceramics led diminishing the temperature and stress developed on the blades, which in turn, enables an increase in the operating life of the turbine.*

0 INTRODUCTION

Gas microturbines (GMT) are small turbomachines that work using gases at high temperatures, with power capacities ranging from 15 kW to 300 kW and offer variable speeds from 30,000 rpm up to 120,000 rpm [1]. They operate with the same operation principle of all the conventional gas turbines; therefore, the efficiency of these devices depends on the gas temperature, which can become higher than 1000 K [2] and [3]. Blades and nozzles of the turbines are subjected to different loads like high temperature, corrosion, centrifugal forces, etc., which could lead to failures [4] and [5]. Regarding high temperature, one of the main drawbacks of GMTs is their small size, which augments heat transfer among their components, leading to failures by burning out or highly stressed zones. Highly stressed zones are often located near the root of the blades as a consequence of non-uniform temperature fields because of sudden changes in geometry and restrictions at the root [6] to [9]. In conventional turbines, in order to cool the blades, internal cooling passages are manufactured; however, this method can not be implemented for microturbines, given the size of such machines [10]. Therefore, the thermal barrier coating (TBC) is used to protect turbine blades and to resist high temperatures environments.

A TBC often has a cover that is composed of three layers: the first is a ceramic topcoat (TC) layer, which has direct contact with hot gases; the second is a bond coat (BC) layer, which offers corrosion resistance; the third is a thermally grown oxide (TGO) layer, which is frequently formed between the TC and BC. Ni-based superalloys are often used as a substrate in gas turbines where TBC provides them with thermal insulation. In this way, TBC allows reducing substrate temperature, prolonging the operation life of the turbine and improving turbine efficiency by increasing its operating temperature [11].

*Corr. Author's Address: Universidad Autonoma del Estado de Morelos, Av. Universidad 1001, Cuernavaca, Mor., Mexico, jcgarcia@uaem.mx

The design of proper TBC plays a key role in the operating life of turbine blades; as a consequence, several studies are focused on the study of TBC characteristics. Li et al. [12] studied the thickness of TBC for a gas turbine blade. The materials used were ZrO_2-8 wt% Y_2O_3 (8YSZ) as a TC layer, α-Al_2O_3 as TGO layer and NiCrAlY as a BC layer. TC thickness was varied from 100 µm to 1000 µm. It was observed that when increasing the TC layer thickness, the thermal insulation capability and stress levels within the coatings are enhanced. Radwan & Elusta [13] performed one-dimensional (1D) calculations to assessing a four-TBC layer made of Zirconia. They concluded that the TBC layer allowed reducing the blade temperature, thus enhancing the blade durability. Also, the material influenced the temperature distribution. Thickness optimization of a barrier coating of partially stabilized zirconia (PSZ) of a turbine blade was executed by Sankar et al. [6]. TBC thickness was varied from 100 µm to 600 µm, and they found a critical thickness that occurred when thickness reached 65 µm, where heat transfer rate was the lowest. In other research [14], the temperature distribution and thermal stress field of TBC were obtained by employing a 2D decoupled method. TBC included the BC, TGO and TC, where the TC was made of 8YSZ. Non-uniform temperature fields were obtained, and zones with high stress were detected at the suction and the leading edge of the blade. In another study, it was shown that the impact of foreign object damage (FOD) could cause erosion on blade samples with TBC, and was most dangerous as it becomes perpendicular to the surface [5].

Several materials have been developed to be used as TBC and studies have been performed to compare their effectiveness of substrate protection. In a review of the main materials used as TC and TGO presented by Sahith et al. [15], it was concluded that the most common material used as substrate material and bond coat was nickel-based superalloys. Meanwhile, yttria-stabilized zirconia (YSZ) (7 %) was most commonly used as the topcoat. YSZ appears as one of the best options to thermally protect the substrate blade, given its thermo-physical and mechanical properties, such as low thermal conductivity. Regarding the gas microturbines, YSZ was also the preferred material to be used as TBC [16].

In recent studies, some researchers have proposed new materials to be used as TBC for gas turbine applications. Chen et al. [17] proposed the synthesized forsterite-type Mg_2SiO_4 material as an alternative to zirconia. They showed a comparison with zirconia (8YSZ) in terms of mechanical properties. The new material proved to have a lower thermal conductivity at 1073 K (1.5 W/(mK) and 2.2 W/(mK) for the new material and 8YSZ, respectively) and better thermal-shock resistance than those made of 8YSZ. Other mechanical properties, such as hardness, fracture toughness and Young´s modulus were similar to those of zirconia. Shi-min et al. [18] also introduced two novel ceramics for thermal barrier coatings. The proposed synthesized materials, $Y_3Ce_7Ta_2O_{23.5}$ and $Yb_3Ce_7Ta_2O_{23.5}$, were new rare-earth tantalite oxides with thermal conductivities lower than that of 8YSZ at 1000 K. Beyond this temperature, the new materials showed good stability which makes them appropriate for high-temperature applications. In another study, Yang et al. [19] synthesized high-purity $Dy_{0.02}Gd_{0.025}Yb_{0.025}Y_{0.05}Zr_{0.8}O_{1.9}$ (DZ), $Ti_{0.02}Dy_{0.02}Gd_{0.025}Yb_{0.025}Y_{0.05}Zr_{0.86}O_{1.9}$ (TZ), and the YSZ powder and coating. According to their results, the TZ TBCs could effectively protect the superalloy substrate at 28 K. Also, the thermal conductivity of the TZ coating was lower than both DZ and YSZ, showing its potential to be used as TBC. However, most of those new materials have been tested under controlled conditions in a laboratory, and their effectiveness under realistic turbine operating conditions need to be considered.

Numerical methods are the preferred tools to predict the thermal and structural fields on blades coated with TBC. Abubakar et al. [20] performed a general review of some methods for predicting residual stress in thermal spray coatings, concluding that some finite element method (FEM) schemes provide results of those stresses reasonably close to experiments; thus, they can be used to predict them in coatings. In contrast, Zhu et al. [7], evaluated the effectiveness of three versions of the k-ϵ turbulence model to predict temperature fields by means of computational fluid dynamics (CFD). The k-ϵ realizable offered the most accurate results when modelling blades with one-layer TBC. Li et al. [12] employed the FEM to design the TBC for a gas turbine blade. They found that thermal insulation was enhanced with the increase of the TC. Also, as mentioned before, Tang et al. [14] carried out a fluid-structure interaction (FSI) coupling method to predict stress fields in a turbine blade. However, their model was restricted to a 2D model. In other works [12] and [21], the uniform temperature on blade surfaces and static blade boundary conditions were used. However, these simplified conditions could drive to imprecise results since temperature fields on blade surfaces, induced by high-temperature combustion gases and the blade, are highly three dimensional and non-uniform.

In this work, a 3D FSI decoupling method of a gas microturbine is carried out to assess novel TBC materials proposed in the technical literature for applications in turbine blades. The coating materials studied are taken from literature: 8YSZ, Mg_2SiO_4, $Y_3Ce_7Ta_2O_{23.5}$ and $Yb_3Ce_7Ta_2O_{23.5}$. To accurately predict the non-uniform temperature fields, stationary guide vanes are taken into account for the numerical domain, giving rise to a single axial passage that includes a static guide vane (nozzle), a rotating blade and their corresponding fluid domains. Results in terms of temperature and stress are discussed to identify the most effective thermal barrier coating for the microturbine.

1 METHODS

1.1 Microturbine Characteristics

The main components of a gas microturbine engine are the expansion microturbine, the combustion chamber and the compressor. The expansion turbine section is referred to here as the microturbine. Computational modelling of an axial gas microturbine is performed using Ansys (Fluent and Mechanical structural). The microturbine geometry is taken from the technical literature [22], which is designed to supply output power of about 29 kW at the rated speed of [illegible] rpm. The microturbine geometry consists of one stage with [illegible] guide vanes of the stator (nozzle) and [illegible] rotating blades. Given its axisymmetric geometry, one 3D single passage that includes one nozzle and one blade is constructed for CFD and FEM computations.

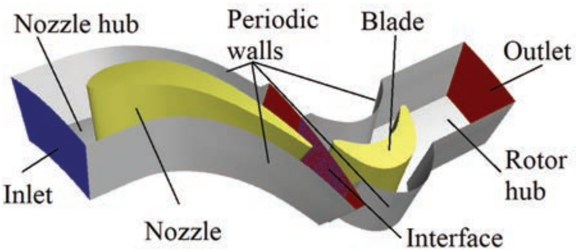

Fig. 1. *Turbine geometry and boundary conditions*

In Fig. 1 the numeric domain is depicted; the shroud is hidden to provide better visualization of the components. The whole computational domain is integrated by both fluid and solid domains corresponding to air and substrate (and TBC) domains. The dimensions of the turbine are [illegible] mm in nozzle height, 7 mm in blade height, [illegible] mm in nozzle chord, 8 mm in blade chord, and [illegible] mm in maximum turbine diameter.

1.2 Methodology for the CFD and Mesh Characteristics

The numerical domain is discretized to generate the mesh needed for calculations. A mesh dependence analysis is carried out to obtain the optimal mesh for the passage. Given that the nozzle and the rotor domains have meshed separately, an interface boundary condition is used to join both domains. It is noteworthy than both solid and fluid domains been have meshed to predict temperature fields and heat transfer flux. Element sizes of 0.1 mm and 0.2 mm and hexahedral element types are used.

A mesh refinement to model the boundary layer was used in the near-wall region of nozzles and blades. Refinement is defined using 5 to 20 layers with a growth rate of 1.2. As a result, nine different meshes with densities ranging from [illegible] to [illegible] elements are constructed. After the analysis, a mesh with [illegible] (Fig. 2) elements is selected to carry out all computations because it has a variation of about 1 % of the computed substrate temperature with respect to a finer mesh. It should be mentioned that the mesh region corresponding to substrates (nozzles and blades) is used for the FEM solution to solve the stress generation.

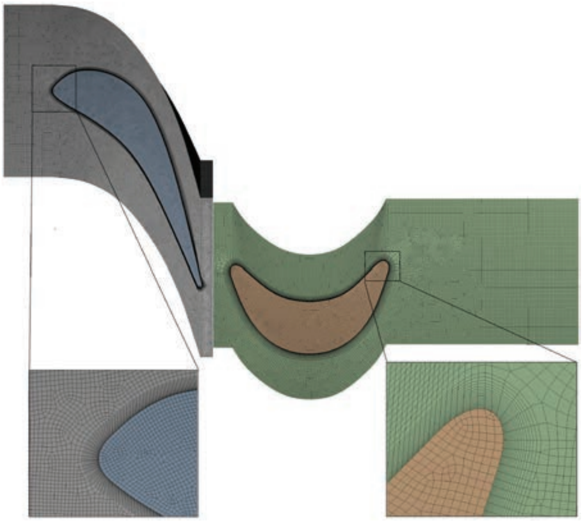

Fig. 2. *Computational mesh for flow field and substrate domains*

1.3 Boundary Conditions of the CFD and Cases of Study

As a consequence of modelling one single passage of the turbine (Fig. 1), boundary conditions are defined as follows: periodic boundary conditions are used at lateral sides of passage, and an interface is created between the nozzle and blade domains to ensure fluid continuity through the passage. The hub and shroud are defined as walls with a no-slip condition. When modelling TBC, thickness and type of material are assigned at coupling walls to model the heat transfer through the coating material. Mass flow rate and pressure outlet conditions are assigned at the inlet and outlet of the passage, respectively. The total mass flow rate incoming to the turbine is equal to 0.23 kg/s at rated speed. Since one single passage is used, this flow rate is divided by the 17 guide vanes resulting in 0.013 kg/s per passage. The fluid is considered as high-temperature compressible air, and a temperature of 1053 K is also specified at the inlet. The solid domain is defined according to the substrate material (nozzles or blades) and their corresponding TBC.

The investigated TBCs are Mg_2SiO_4, $Y_3Ce_7Ta_2O_{23.5}$ and $Yb_3Ce_7Ta_2O_{23.5}$, which are compared to 8YSZ. Coating material properties are taken from [17] to [19], and their properties are defined based on a temperature range of 973 K to 1073 K to match with the operating temperature of the microturbine. The TBC properties used to predict heat transfer by CFD are indicated in Table 1, which also contains substrate (nozzles and blades) properties [23]. Coating thickness is considered uniform and constant for the whole cases with a value of 500 µm based on some investigations [6] and [12], and it is added as a virtual layer into the CFD software. This virtual technique uses the TBC properties (thermal conductivity, specific heat, density and thickness) to compute heat transfer to the blades.

Table 1. *Top coating and substrate properties*

Material	Thermal conductivity [W/(mK)]	Density [kg/m³]	Specific heat [J/(kgK)]
Nimonic 105 (substrate) [23]	22.23	8010	628
8YSZ [19]	2.2	3610	505
Mg_2SiO_4 [17]	1.76	3210	177000
$Y_3Ce_7Ta_2O_{23.5}$ [18]	1.78	7245	472.1
$Yb_3Ce_7Ta_2O_{23.5}$ [18]	1.4	6321	431.1

1.4 Governing Equations and Turbulence Model

A numerical FSI analysis is conducted using Ansys Workbench commercial code, which is used to solve thermal (Ansys Fluent) and structural (Ansys-Structural) analyses. First, the steady-state Reynolds-averaged Navier Stokes equations (RANS) approach is used to solve governing equations using CFD. Then the FEM is employed to calculate thermal stresses.

CFD is used to compute the flow and temperature fields at steady-state conditions, taking into account the turbine operating conditions, like mass flow, pressure, temperature, wall thermal condition and rotating speed. Governing equations of continuity and momentum, given by Eqs. (1) and (2), are solved using Ansys Fluent. To compute the conjugate heat transfer (CHT), the energy equation, depicted by Eq. (3), is also solved.

$$\frac{\partial \rho}{\partial t} + \left(\rho v_i\right)_{,i} = 0, \tag{1}$$

$$\rho \frac{\partial v_j}{\partial t} + \rho v_{j,i} v_i + p_j - \tau_{ij,i} - \rho F_j = 0, \tag{2}$$

$$\rho \frac{\partial \varepsilon}{\partial t} + \rho \varepsilon_i v_i + p v_{i,i} - \tau_{ij} v_{j,i} + q_{i,i} - \rho r = 0, \tag{3}$$

where t is the time, ρ is the density per unit mass, v_i is the i component of the velocity vector, ε is the internal energy per unit mass, F_i is the i component of the body force vector, p is the pressure, q_i is the heat flux, r is the heat supply per unit mass and τ_{ij} is the viscous stress tensor, respectively, and the comma means is partially derived with respect to the independent variables [24].

As stated before, since the air is considered as compressible, continuity and momentum equations are coupled to the energy equation, which provided the temperature distribution in the flow field. Therefore, in order to solve turbulence and accurately predict the CHT, the realizable k–ε turbulence model is selected based on the study of Zhu et al. [7]. This model is based on the k–ε model [25] and differs in the formulation for the turbulent viscosity and for the transport equation for the dissipation rate as follows:

$$\frac{\partial}{\partial t}\left(\rho k\right) + \frac{\partial}{\partial x_j}\left(\rho k u_j\right) = \frac{\partial}{\partial x_j}\left[\left(\mu + \frac{\mu_t}{\sigma_k}\right)\frac{\partial k}{\partial x_j}\right] + G_k + G_b - \rho\varepsilon - Y_M + S_k, \tag{4}$$

$$\frac{\partial}{\partial_t}\left(\rho \varepsilon\right) + \frac{\partial}{\partial x_j}\left(\rho \varepsilon u_j\right) = \frac{\partial}{\partial x_j}\left[\left(\mu + \frac{\mu_t}{\sigma_\varepsilon}\right)\frac{\partial \varepsilon}{\partial x_j}\right] + \rho C_1 S\varepsilon - \rho C_2 \frac{\varepsilon^2}{k + \sqrt{\nu\varepsilon}} + C_{1\varepsilon}\frac{\varepsilon}{k} C_{3\varepsilon} G_b + S_\varepsilon, \tag{5}$$

where $C_1 = \max\left[0.43, \frac{\eta}{\eta + 5}\right]$, $\eta = S\frac{k}{\varepsilon}$, $S = \sqrt{2S_{ij}S_{ij}}$, k is the turbulent kinetic energy and ε is its rate of dissipation. G_k represents the generation of turbulence kinetic energy due to the mean velocity gradients, G_b is the generation of turbulence kinetic energy due to buoyancy, Y_M represents the contribution of the fluctuating compressible turbulence to the overall dissipation rate, C_2, $C_{1\varepsilon}$ and $C_{3\varepsilon}$ are constants, σ_k and σ_ε are the turbulent Prandtl numbers for k and ε, respectively. Finally, S_k and S_ε are user-defined source terms. In contrast, to model the rotation of blades, the multiple reference frame (MRF) model is used. This model is suggested when a steady-state approach is used, and it allows to observe the instantaneous flow field of the moving part as to freezing it. Both stationary and moving domains are governed by continuity and momentum equations (Eqs. (1) and (2)).

To calculate the heat flux transferred from the flow to solid, a conductive and convective problem is modelled by solving the CHT. Newton's law of cooling and Fourier's law are solved to obtain the energy exchange by convection and conduction mechanisms, respectively. Fourier's law to compute the three-dimensional heat conduction is described by Eq. (6):

$$\frac{\partial^2 T}{\partial x^2}+\frac{\partial^2 T}{\partial y^2}+\frac{\partial^2 T}{\partial z^2}+\frac{\dot{q}}{k}=\frac{1}{\alpha}\frac{\partial T}{\partial \tau}, \qquad (6)$$

where $\dot{q}$ is the heat transfer rate, k is thermal conductivity, α is the thermal diffusivity of the material, T is the temperature, and x, y and z, are coordinate directions. The convection is solved using Newton law which is given by Eq. (7) as follows:

$$\dot{q}=hA\left(T_w-T_\infty\right), \qquad (7)$$

where h is the convection heat-transfer coefficient, A is the surface area, and T_w and T_∞ are the surface and the free stream fluid temperature, respectively. In this case, h is highly influenced by the fluid motion driving to a forced convection case.

In contrast, the thickness of the coating is specified on the walls to obtain the thermal insulation and temperature decrement on turbine components. Temperature fields are needed to calculate stress fields in the blades. Mechanisms for corrosion and erosion, phase transformation of the ceramic coating or its fracture behaviour are neglected to simplify the computations of the effectiveness of thermal insulation of TBCs and the thermal stress induced on nozzles and blades.

1.5 Finite Element Procedure

Once temperature fields are solved using CFD, FEM is employed to compute stress on the components using Ansys Mechanical software. A decoupling method is used, in which the temperature in the components computed by CFD is sent to FEM software. The surface and internal temperature fields of substrates are used as a boundary condition in conjunction with restrictions to elongation of turbine components. Constraints are specified as follows: the nozzle is fixed at the top and bottom surfaces, and the blade is fixed only at its root. The properties of nozzle and blade are assigned based on Nimonic alloy 105 substrate material, as indicated in Table 1. This material is assumed to be homogeneous, continuous, and isotropic. Other properties used are the Young modulus of 19 GPa, the Poisson's Ratio of 0.3 and the thermal expansion coefficient of 13 × 10^{-6}/K [23]. The same solid meshes depicted in Fig. 2 are used to predict three-dimensional stress fields accurately.

1.6 Governing Equations

Thermal stress distribution was calculated following Eqs. (8) to (10); non-uniform and three-dimensional stress fields were obtained. Those equations describe three thermal stress components in the tangential, radial, and longitudinal directions, respectively [26]. The equations allow taking into account partial mechanical constraints and internal constraints due to differences in thermal expansion of elements due to different temperatures. Also, when solving them, it was assumed that thermal equilibrium is reached at the rated speed of the turbine.

$$\sigma_t=\frac{E\alpha}{1-v}\frac{1}{r^2}\left(\frac{r^2+r_i^2}{r_o^2-r_i^2}\int_{r_i}^{r_o}T\cdot r d_r+\int_{r_i}^{r}T\cdot r d_r-T\cdot r^2\right), \qquad (8)$$

$$\sigma_r=\frac{E\alpha}{1-v}\frac{1}{r^2}\left(\frac{r^2+r_i^2}{r_o^2-r_i^2}\int_{r_i}^{r_o}T\cdot r d_r+\int_{r_i}^{r}T\cdot r d_r\right), \qquad (9)$$

$$\sigma_z=\frac{E\alpha}{1-v}\left(\frac{2}{r_o^2-r_i^2}\int_{r_i}^{r_o}T\cdot r d_r-T\right), \qquad (10)$$

where d_r indicates that the definite integrals are solved through the radial direction from inner radius, r_i, to the outer radius, r_o (or an arbitrary intermediate radius, r); E is the Young Modulus, α is the thermal expansion coefficient, v is the Poisson ratio, T is temperature, and t, r, and z are the tangential, radial and longitudinal directions, respectively. Results are represented using the equivalent stress or Von Mises stress, which is derived from the Cauchy stress tensor. The equivalent stress is defined by Eq. (11):

$$\sigma_{eq}=\left(\sigma_t^2+\sigma_r^2+\sigma_z^2-\left(\sigma_t\sigma_r+\sigma_r\sigma_z+\sigma_z\sigma_t\right)\right)^{1/2}, \qquad (11)$$

where σ_{eq} is equivalent stress, and t, r, and z are the tangential, radial, and longitudinal directions, respectively. This equivalent stress was taken as the criterion to select the better TBC in terms of the thermal stress generated in the substrate.

2 RESULTS

2.1 Analysis of Temperature Distribution

Analyses of temperature distribution on the components of the whole turbine, with and without TBC, are carried out. For the case of nozzle coated with 8YSZ, the temperature distribution is plotted in Fig. 3. Data show profiles of non-dimensional surface temperature variation at midspan from both pressure and suction sides with non-dimensional blade chord length (Cx). Profiles show that maximum temperature occurs at the trailing edge, then decreases along the substrate forming valleys, and finally, it rises in the leading edge. The trend of temperature is compared with experimental data of Dong et al. [27], and a good agreement is obtained as shown in Fig. 3

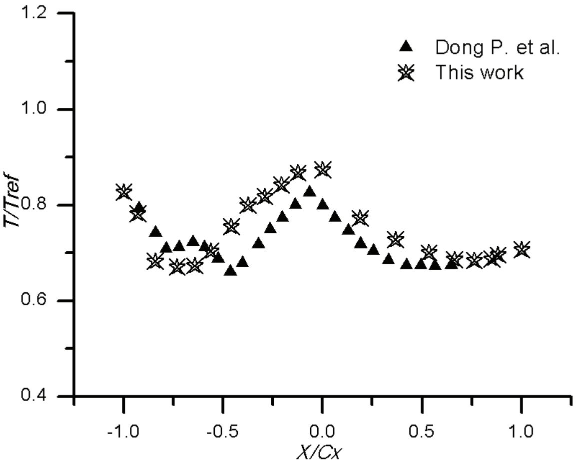

Fig. 3. *Comparison of temperature distribution of vane surface with literature*

The substrate temperature of turbine components is analysed to assess the insulating effectiveness of coating materials. In Fig. 4 the temperature field contours on nozzle and blade without TBC are shown. It can be observed that zones of highest temperature on the nozzle substrate appear at the top of trailing edge (Fig. 4a). Meanwhile, regions of lowest temperature are located at the top of the nozzle and near the middle of the chord line distance where it has its maximum thickness and maximum camber. Also, temperatures on the pressure side are higher than those of the suction side.

In contrast, temperatures of the blade at leading-edge are higher than those of the trailing edge as shown in Fig. 4b, which can be attributed to higher convective heat transfer promoted by gas expansion in this section and blade rotation. Furthermore, a small zone of high temperature is formed at the lower part of the trailing edge near the base of the blade as a consequence of a reduction in blade thickness. The temperature on the blade pressure side is higher than the suction side, where the lowest temperature is identified near the base. According to these results, highly heated zones are detected on the substrates and, with regards to the blade, it reaches temperatures close to the gas temperature. That phenomenon led to the necessity of using TBCs as an insulating method to decrease the temperature and thermal stress in the turbine components.

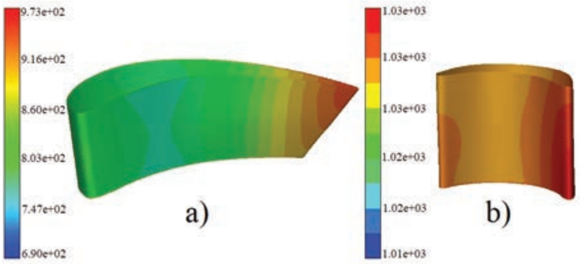

Fig. 4. *Surface temperature in K without TBC; a) nozzle, and b) blade*

Temperature variation with the usage of TBCs is also analysed. The contour plot of surface temperature on turbine components with the TBCs is shown in Figs. 5 and 6. In Fig. 5 surface temperature fields on nozzle are illustrated. The contours reveal a decrease in temperature levels when using TBCs as compared with the case without TBC of Fig. 4a. The temperature distribution between Mg_2SiO_4 and $Y_3Ce_7Ta_2O_{23.5}$ is very similar, and it displays the higher areas of low temperature from all the calculations. However, in the case of $Yb_3Ce_7Ta_2O_{23.5}$, contours show higher temperature than the other TBCs and temperature levels are close to the case without TBC. It can also be observed in Fig. 5 that, even with TBC, the magnitude of temperature at trailing edge is still higher than other zones of the nozzle for all the cases, which is consistent with investigations found in the literature [27] to [29] and the ones shown previously in Fig. 3. Meanwhile, the temperature on the suction side is lower than the pressure side for the whole cases as a consequence of the higher area being protected by the thermal barrier coating and nozzle thickness.

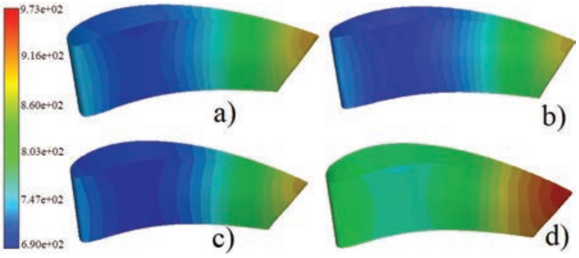

Fig. 5. *Surface temperature of nozzle in K with the coating materials; a) 8YSZ, b) Mg_2SiO_4, c) $Y_3Ce_7Ta_2O_{23.5}$, and d) $Yb_3Ce_7Ta_2O_{23.5}$*

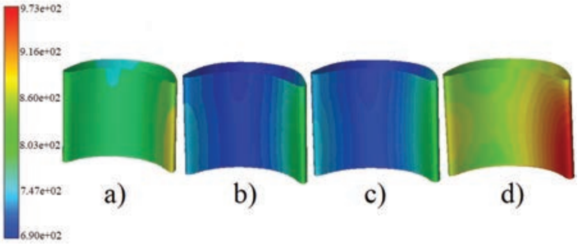

Fig. 6. *Surface temperature of blade in K with the coating materials; a) 8YSZ, b) Mg_2SiO_4, c) $Y_3Ce_7Ta_2O_{23.5}$, and d) $Yb_3Ce_7Ta_2O_{23.5}$*

In contrast, temperature fields developed on the blade are depicted in Fig. 6. Temperature levels are under those obtained from the case without TBC (Fig. 4). As can be seen from Fig. 6, the temperature on the leading edge is higher than the other regions. Those temperatures are a result of an increase of heat transfer due to the impact of flow with the leading edge driving to the development of a stagnation zone and the decrease of gas velocity. Also, the same small zone of high temperature formed at the lower part of the trailing edge, similar to the case without TBC, can be observed. Regarding thermal insulation, interesting results can be inferred from the contour plots. Temperature distribution between Mg_2SiO_4 and $Y_3Ce_7Ta_2O_{23.5}$ displays the lowest temperatures as it occurs in the nozzle. However, when 8YSZ is applied, temperatures are close to those of $Yb_3Ce_7Ta_2O_{23.5}$. Although these two materials showed the higher temperatures among the TBCs, temperature fields are still lower and distinct to substrate without TBC. Furthermore, similar to the nozzle, $Yb_3Ce_7Ta_2O_{23.5}$ shows the highest temperature among all the coating materials.

To assess the thermal insulation effectiveness of the barrier coatings, maximum and minimum temperature values on the substrates are summarized in Table 2. Data are classified by the turbine component and their corresponding TBC, including the calculation without TBC. Maximum temperatures on each component are located at trailing edge and leading edge for the nozzle and the blade, respectively, as shown before in Figs. 4 and 5. In the nozzle substrate, the maximum and minimum temperatures are obtained with the No TBC and the Mg_2SiO_4 cases, respectively. However, the temperatures between $Y_3Ce_7Ta_2O_{23.5}$ and Mg_2SiO_4 cases are very close. The highest of the maximum temperature is 972.6 K, while the lowest value of the maximum temperature is equivalent to 893.5 K. Hence, the drop of temperature, when Mg_2SiO_4 is applied, is about 80.0 K. In contrast, when analysing the blade substrate, the maximum and minimum temperatures also appear when no TBC is used and when Mg_2SiO_4 is assigned, respectively.

Table 2. *Temperature levels on the components with and without TBC*

Material	Temperature [K]			
	Nozzle		Blade	
	minimum	maximum	minimum	maximum
No TBC	779.04	972.64	1022.48	1032.97
8YSZ	704.75	907.79	1018.69	1026.05
Mg_2SiO_4	689.54	893.54	1012.67	1021.87
$Y_3Ce_7Ta_2O_{23.5}$	690.34	894.4	1012.94	1022.01
$Yb_3Ce_7Ta_2O_{23.5}$	771.81	957.24	1023.28	1032.90

Among the maximum temperatures, the peak value is 1032.9 K, and the lowest one is 1021.8 K. As a result, drop of temperature when using Mg_2SiO_4 is a little more of 11 K. This drop of temperature is due to cooling the blade is a hard task owing to high heat transfer rate product of the forced convection of the turbine operation. Other parameters, including gas pressure, temperature or velocity, were not affected at all by the change of TBCs, and they were neglected from analysis of the results. In conclusion, the better thermal insulation on both components is provided by Mg_2SiO_4 and $Y_3Ce_7Ta_2O_{23.5}$ barriers. These results reveal that the thermal protection of these new materials is better than that provided by YSZ.

2.2 Analysis of Stress Distribution

Thermal stress fields are determined by considering temperature obtained by CFD as thermal load in the FEM model using a decoupled method. In Fig. 7, thermal stress distribution on the substrate of components (nozzles and blades) without TBC is illustrated through the Von Mises stress. In the nozzle, maximum stress is gotten at the trailing edge bottom due to the combination of the highest temperature in this region and constraints at the root (Fig. 4). Some concentration of stress also can be observed at the middle of the chord length and top of the nozzle as a consequence of the temperature gradient. In contrast, the highest stress magnitude on the blade is located at the bottom of the leading edge, as observed in Fig. 7b. Also, high stress can be distinguished at the bottom of the trailing edge. In general, most of the stress of this component is distributed along the base because of the constraints to deformation in this zone. Additionally, the stress in the suction side is higher than the pressure side.

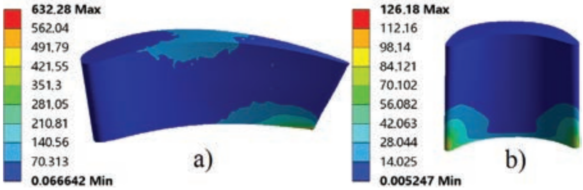

Fig. 7. *Von Mises stress in MPa on the components without TBC; a) nozzle, and b) blade*

Stress distributions on the nozzle substrate when using TBCs are shown in Fig. 8. It can be seen that the distribution of stress is very similar to Fig. 7a when no TBC is used. Maximum stress is also located at the trailing edge, and a stressed zone also appears at the middle chord length of the nozzle for all the cases with TBC. The main differences, however, can be found on stress levels. When 8YSZ is applied, substrates exhibit the highest stress magnitude, which can be attributed to a higher temperature gradient owing to non-uniform inner temperature, as observed in Fig. 5a. Calculations with Mg_2SiO_4, $Yb_3Ce_7Ta_2O_{23.5}$ and $Y_3Ce_7Ta_2O_{23.5}$ indicate a similarity in stress magnitudes.

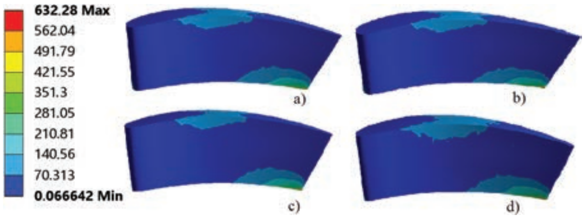

Fig. 8. *Von Mises stress in MPa on the nozzle with TBC; a) 8YSZ, b) Mg_2SiO_4, c) $Y_3Ce_7Ta_2O_{23.5}$, and d) $Yb_3Ce_7Ta_2O_{23.5}$*

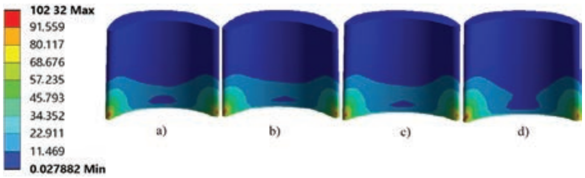

Fig. 9. *Von Mises stress in MPa on the blade with TBC; a) 8YSZ, b) Mg_2SiO_4, c) $Y_3Ce_7Ta_2O_{23.5}$, and d) $Yb_3Ce_7Ta_2O_{23.5}$*

In Fig. 9, Von Mises contour results on the blade substrate are shown for the TBC cases. Distribution of high stress was also similar to Fig. 7b when no thermal protection is used, including the $Yb_3Ce_7Ta_2O_{23.5}$. The four TBCs yielded similar stress distribution inside the blade. Most of the highest stresses are calculated at the leading edge, the trailing edge, and the blade root. Also, stress on the suction side is higher than the pressure side zone. The maximum stress magnitude, however, is under the values obtained when no TBC is used. Hence, these results reveal that all the thermal barriers protect the blade in terms of diminishing the stress generated by the high temperatures and constraints.

3 DISCUSSION

For a better understanding of the effect of the thermal barrier coating on the stress of substrates, the maximum equivalent stress magnitudes from each TBC case are shown in Table 3. It is observed that the maximum stress values on the nozzle substrate when using TBC are close to each other, but they are under yield stress of the material. Among them, the highest stress is produced when using 8YSZ with a stress drop of about 31 MPa. In contrast, the lowest stress values are obtained from the Mg_2SiO_4 and $Y_3Ce_7Ta_2O_{23.5}$ barriers yielding a stress reduction of around 40 MPa. However, it should be pointed out that the difference in stress reduction between Mg_2SiO_4, $Y_3Ce_7Ta_2O_{23.5}$ and $Yb_3Ce_7Ta_2O_{23.5}$ is barely observable. Therefore, those three materials provide almost the same stress reduction in the nozzle substrate. In contrast, from Table 3, it can be seen that while temperature decreases in the blade, TBCs stress is also reduced. The maximum stress magnitudes of the substrate are quite similar for all the calculations. The four thermal barriers yield a stress reduction on the blade of around 24 MPa compared with the no TBC case.

Table 3. *Maximum Von Mises stress on the components with and without TBC*

Material	Equivalent stress [MPa]	
	Nozzle	Blade
No TBC	632.28	126.18
8YSZ	601.01	102.58
Mg_2SiO_4	591.40	102.31
$Y_3Ce_7Ta_2O_{23.5}$	591.91	102.32
$Yb_3Ce_7Ta_2O_{23.5}$	593.29	102.41

4 CONCLUSIONS

A 3D model of a microturbine is simulated to assess the effect of TBC on temperature distribution and thermal stress fields on nozzles and blades. Four different thermal barrier coatings materials are tested: 8YSZ, Mg_2SiO_4, $Y_3Ce_7Ta_2O_{23.5}$ and $Yb_3Ce_7Ta_2O_{23.5}$, and compared with a no TBC case. The temperature fields are calculated solving a conjugated heat transfer problem that includes fluid-structure interaction using CFD. The thermal stress distribution is calculated with FEM, using the temperature inside the solid substrates obtained from CFD. The results show a highly three-dimensional and non-uniform temperature distribution on the turbine components, which affected the thermal stress. The maximum temperatures are located at the trailing edge and the leading edge for the nozzle and blade, respectively. The best thermal insulation from both components is obtained with the Mg_2SiO_4 and $Y_3Ce_7Ta_2O_{23.5}$ materials which allow to obtain the highest temperature reduction of substrate. In contrast, when using a TBC to protect the blade substrate, the stress is less affected, producing almost the same magnitudes among the four cases. However, if thermal protection is considered, Mg_2SiO_4 and $Y_3Ce_7Ta_2O_{23.5}$ materials show an advantage over the other thermal barriers to protect the microturbine components. Data obtained with the usage of these new materials provide better results than YSZ, which is currently one of the most materials used for gas turbine applications, regarding temperature reduction and the stress generated.

5 REFERENCES

[1] Nascimento, M.A.R., Rodrigues, L., Santos, E., Gomes, E.E.B., Dias, F.L.G., Velásques, E.I.G., Carrillo, R.A.M. (2013). Micro gas turbine engine: A review, Benini, E. (ed.), *Progress in Gas Turbine Performance*. IntechOpen, London, p. 107-141, **DOI:10.5772/54444**.

[2] Xie, Y., Lu, K., Liu, L., Xie, G. (2014). Fluid-thermal-structural coupled analysis of a radial inflow micro gas turbine using computational fluid dynamics and computational solid mechanics. *Mathematical Problems in Engineering*, vol. 2014, art. ID 640560, **DOI:10.1155/2014/640560**.

[3] Swar, R., Hamed, A., Shin, D., Woggon, N., Miller, R. (2012). Deterioration of thermal barrier coated turbine blades by erosion. *International Journal of Rotating Machinery*, vol. 2012, art. ID 601837, **DOI:10.1155/2012/601837**.

[4] Carter, T.J. (2005). Common failures in gas turbine blades. *Engineering Failure Analysis*, vol. 12, no. 2, p. 237-247, **DOI:10.1016/j.engfailanal.2004.07.004**.

[5] Golewski, P., Sadowski, T. (2019). The influence of TBC aging on crack propagation due to foreign object impact. *Materials*, vol. 12, no 9, art ID 1488, **DOI:10.3390/ma12091488**.

[6] Sankar, V., Ramkumar, P.B., Sebastian, D., Joseph, D., Jose, J., Kurian, A. (2019). Optimized thermal barrier coating for gas turbine blades. *Materials Today: Proceedings*, vol. 11, part 3, p. 912-919, **DOI:10.1016/j.matpr.2018.12.018**.

[7] Zhu, W., Wang, J.W., Yang, L., Zhou, Y.C., Wei, Y.G., Wu, R.T. (2017). Modeling and simulation of the temperature and stress fields in a 3D turbine blade coated with thermal barrier coatings. *Surface and Coatings Technology*, vol. 315, p. 443-453, **DOI:10.1016/j.surfcoat.2017.03.012**.

[8] Guo, J., Xie, D., Zhang, H., Jiang, W., Zhou, Y. (2016). Effect of heat transfer coefficient of steam turbine rotor on thermal stress field under off-design condition. *Frontiers in Energy*, vol. 10, p. 57-64, **DOI:10.1007/s11708-015-0385-3**.

[9] Sadowski, T., Golewski, P. (2015). Cracks path growth in turbine blades with TBC under thermo – mechanical cyclic loadings. *Frattura ed Integrità Strutturale*, vol. 10, no. 35, p. 492-499, **DOI:10.3221/IGF-ESIS.35.55**.

[10] Soares, C. (2011). *Microturbines: Applications for Distributed Energy Systems*. Elsevier, Belington.

[11] Clarke, D.R., Oechsner, M., Padture, N.P. (2012). Thermal-barrier coatings for more efficient gas-turbine engines. *MRS Bulletin*, vol. 37, no. 10, p. 891-898, **DOI:10.1557/mrs.2012.232**.

[12] Li, B., Fan, X., Li, D., Jiang, P. (2017). Design of thermal barrier coatings thickness for gas turbine blade based on finite element analysis. *Mathematical Problems in Engineering*, vol. 2017, art ID. 2147830, **DOI:10.1155/2017/2147830**.

[13] Radwan, M.M., Elusta, S.A. (2016). Thermal barrier coatings for temperature management of gas-turbine blades. International Journal of Research in Chemical. *Metallurgical and Civil Engineering*, vol. 3, no. 2, p. 219-222, **DOI:10.15242/ijrcmce.iae0716412**.

[14] Tang, W.Z., Yang, L., Zhu, W., Zhou, Y.C., Guo, J.W., Lu, C. (2016). Numerical simulation of temperature distribution and thermal-stress field in a turbine blade with multilayer-structure TBCs by a fluid–solid coupling method. *Journal of Materials Science & Technology*, vol. 32, no. 5, p. 452-458, **DOI:10.1016/j.jmst.2016.03.009**.

[15] Sahith, M.S., Giridhara, G., Kumar, R.S. (2018). Development and analysis of thermal barrier coatings on gas turbine blades – a review. *Materials Today: Proceedings*, vol. 5, no. 1, p. 2746-2751, **DOI:10.1016/j.matpr.2018.01.060**.

[16] Naraparaju, R., Lau, H., Lange, M., Fischer, C., Kramer, D., Schulz, U., Weber, K. (2018). Integrated testing approach using a customized micro turbine for a volcanic ash and CMAS related degradation study of thermal barrier coatings. *Surface and Coatings Technology*, vol. 337, p. 198-208, **DOI:10.1016/j.surfcoat.2018.01.030**.

[17] Chen, S., Zhou, X., Song, W., Sun, J., Zhang, H., Jiang, J., Deng, L., Dong, S., Cao, X. (2019). Mg2SiO4 as a novel thermal barrier coating material for gas turbine applications. *Journal of the European Ceramic Society*, vol. 39, no. 7, p. 2397-2408, **DOI:10.1016/j.jeurceramsoc.2019.02.016**.

[18] Shi-min, W., Wei-wei, Z., Hong-song, Z., Fei, W., Debing, S., Xian-feng, Y., Zhi-he, S., Qun-peng, D., Wen-peng, M. (2019). $Y_3Ce_7Ta_2O_{23.5}$ and $Yb_3Ce_7Ta_2O_{23.5}$—two kinds of novel ceramics for thermal barrier coatings. *Ceramics International*, vol. 45, no. 8, p. 10414-10419, **DOI:10.1016/j.ceramint.2019.02.100**.

[19] Yang, M., Zhu, Y., Wang, X., Wang, Q., Ai, L., Zhao, L., Chu, Y., Guo, S., Hu, J., Zhang, Q. (2019). Preparation and thermophysical properties of Ti^{4+} doped zirconia matrix

thermal barrier coatings. *Journal of Alloys and Compounds*, vol. 777, p. 646-654, **DOI:10.1016/j.jallcom.2018.11.034**.

[20] Abubakar, A.A., Arif, A.F.M., Al-Athel, K.S., Akhtar, S.S., Mostaghimi, J. (2017). Modeling residual stress development in thermal spray coatings: Current status and way forward. *Journal of Thermal Spray Technology*, vol. 26, p. 1115-1145, **DOI:10.1007/s11666-017-0590-1**.

[21] Yang, L., Liu, Q.X., Zhou, Y.C., Mao, W.G., Lu, C. (2014). Finite element simulation on thermal fatigue of a turbine blade with thermal barrier coatings. *Journal of Materials Science & Technology*, vol. 30, no. 4, p. 371-380, **DOI:10.1016/j.jmst.2013.11.005**.

[22] Tenango-Pirin, O., Garcia, J.C., Castro-Gomez, L., Rodriguez, J.A., Sierra, F., De Santiago, O., Rodriguez-Lelis, J.M. (2016). Effect of the modification of the start-up sequence on the thermal stresses for a microgas turbine. *International Journal of Rotating Machinery*, vol. 2016, art. ID 5834172, **DOI:10.1155/2016/5834172**.

[23] NIMONIC® alloy 105 (2007) from: *https://www.specialmetals.com/assets/smc/documents/alloys/nimonic/nimonic-alloy-105.pdf*, accessed on 2019-10-24

[24] Chung, T. (2010). *Computational Fluid Dynamics*. Cambridge university press, Cambridge.

[25] Launder, B.E., Spalding, D.B. (1974). The numerical computation of turbulent flows. *Computer Methods in Applied Mechanics and Engineering*, vol. 3, no. 2, p. 269-289, **DOI:10.1016/0045-7825(74)90029-2**.

[26] Kim, T.S., Lee, D.K., Ro, S.T. (2000). Analysis of thermal stress evolution in the steam drum during start-up of a heat recovery steam generator. *Applied Thermal Engineering*, vol. 20, no. 11, p. 977-992, **DOI:10.1016/S1359-4311(99)00081-2**.

[27] Dong, P., Wang, Q., Guo, Z., Huang, H., Feng, G. (2009). Conjugate calculation of gas turbine vanes cooled with leading edge films. *Chinese Journal of Aeronautics*, vol. 22, no. 2, p. 145-152, **DOI:10.1016/S1000-9361(08)60080-1**.

[28] Wang, Z., Yan, P., Guo, Z., Han, W. (2008). BEM/FDM conjugate heat transfer analysis of a two-dimensional air-cooled turbine blade boundary layer. *Journal of Thermal Science*, vol. 17, p. 199-206, **DOI:10.1007/s11630-008-0199-2**.

[29] Rezazadeh Reyhani, M., Alizadeh, M., Fathi, A., Khaledi, H. (2013). Turbine blade temperature calculation and life estimation - a sensitivity analysis. *Propulsion and Power Research*, vol. 2, no. 2, p. 148-161, **DOI:10.1016/j.jppr.2013.04.004**.

Strojniški vestnik - Journal of Mechanical Engineering 66(2020)10, 591-601

DOI:10.5545/sv-jme.2020.6707
Original Scientific Paper
Received for review: 2020-04-07
Received revised form: 2020-08-04
Accepted for publication: 2020-09-01

Effect of Blade Coating on a Centrifugal Pump Operation under Sediment-Laden Water Flow

Yong Wang[1] – Zilong Zhang[1] – Jie Chen[2] – Houlin Liu[1] – Xiang Zhang[3,*] – Marko Hočevar[4]

[1] Jiangsu University, Research Center of Fluid Machinery Engineering and Technology, China
[2] Beijing Institute of Technology, School of Mechanical and Vehicular Engineering, China
[3] Xihua University, Key Laboratory of Fluid and Power Machinery, China
[4] University of Ljubljana, Faculty of Mechanical Engineering, Slovenia

Applying a high strength coating on a blade's surface could significantly prolong the service life of a centrifugal pump under sediment-laden water flow because of its protection. To explore the effect of blade coating, the characteristics of energy, vibration and pressure fluctuation of a centrifugal pump (the specific speed (n_s) is 81.46) with different polyurethane coating thickness coefficients were experimentally studied under sediment-laden water flow. Keeping the blade outlet angle, blade inlet angle and blade shape unchanged, the head H and efficiency η under both sediment-laden flow and clear water flow decrease significantly as the coating thickness coefficient increases. The axis rotating frequency and blade passing frequency are the main excitation frequencies of the pump vibration velocity amplitude and outlet pressure fluctuation. The vibration velocity amplitude and outlet pressure fluctuation at the frequency of 1 BPF are the largest. At the frequency of 1 axis rotating frequency, they are the second in all cases. The peak values of both vibration velocity amplitude and outlet pressure fluctuation are proportional to the coating thickness coefficient. An analysis was performed for several increasing coating thicknesses, corresponding to coating coefficients from K_0 to K_3. When the coating thickness coefficients are K_0, K_1, and K_2, the peak value of vibration velocity amplitude under sediment-laden flow is larger than that under clear water flow, but the very small difference between them undercoating thickness coefficient K_3. The peak values of pressure fluctuations under different flow rates decrease first and then increase with the increasing coating thickness coefficient, and lowest points are all located at the coating thickness coefficient K_1.

Keywords: blade coating, vibration, pressure fluctuation, sediment-laden flow, centrifugal pump

Highlights

- *The characteristics of energy, vibration and pressure fluctuation of a blade-coated centrifugal pump under sediment-laden flow are studied experimentally.*
- *The blade coating has a small negative effect on the pump energy characteristics, although it may prevent surface wear.*
- *The peak values of vibration velocity amplitude and pressure fluctuation are all located at the same frequency in all experimental cases.*
- *When the flow rate is small, the peak values of vibration velocity amplitude under sediment-laden flow are lower than that under clear water flow.*
- *Under both flows, the peak values of pressure fluctuation decrease first and then increase with the increasing coating thickness coefficient.*

0 INTRODUCTION

As essential equipment for fluid transportation, the centrifugal pump plays an important role in irrigation, metallurgy, water conservation, and mining industry, etc. The working medium of the pump is sediment-laden flow rather than a single medium water flow. The solid phase of sediment-laden flow can abrade the wet parts, causing noise, vibration, leakage and, finally, pump breakdown. Due to the high rotational speed of the impeller, breakage is most likely to happen on the pressure surface of the impeller blades in a solid-liquid two-phase flow centrifugal pump. Furthermore, the strong vibration, pressure fluctuation and abrasion of a damaged centrifugal pump significantly reduces the reliability of the pumping station system and causes environmental noise pollution. Therefore, it is important to improve the performance of the pump when transporting solid-liquid two-phase liquid.

At present, scholars have done much research on the energy characteristics, pressure fluctuation, and vibration for some typical hydraulic machinery under solid-liquid two-phase flow. Work is performed experimentally and by numerical simulation. Wang and Qian [1] investigated the effects of the silt concentration and grain size on the head and efficiency of the pump. They established a relationship for the head reduction factors as a function of the silt parameters for the double-suction centrifugal pump. Jin [2] numerically carried out the response law of impeller channel and vibration in a centrifugal pump and concluded that changing the number of impeller blades can effectively reduce the vibration intensity and avoid resonance. Rodriguez et al. [3] presented an

*Corr. Author's Address: Xihua University, Key Laboratory of Fluid and Power Machinery, Chengdu, China, 927340633@qq.com

analytical prediction method for the peak frequency and amplitude of the rotor-stator interaction (RSI) in large pump turbines in a qualitative way. Han et al. [4] analysed the pressure fluctuations and the axial force on the impeller in a solid-liquid two-phase flow centrifugal pump. In this study, a three-dimensional simulation was performed for the solid-liquid two-phase turbulent flow in a centrifugal pump with a radial diffuser by the mixture multiphase model, the large eddy simulation turbulence model, and sliding mesh technology. Kumar et al. [5] evaluated the centrifugal slurry pump total head, efficiency, and input power operating with a multi-sized particulate slurry of bottom ash and fly ash mixtures at different flow rates. Zhao et al. [6] numerically simulated the solid-liquid two-phase flow of a double suction centrifugal pump with the computational fluid dynamics. The path of the particle in the channel under different particle sizes and particle volume concentrations was revealed. Hazra and Steiner [7] computed the flow field of diluting two-phase flow pump in turbulent conditions for the continuous phase with the Reynolds averaged NavierS tokes equations together in a mixing length turbulence modelling. The large-size particles accumulated at the lower pressure zone near the cashing wall or the rotating shaft. Zhang et al. [8] numerically simulated and analysed turbulent solid-liquid two-phase flows in a low-specific-speed centrifugal pump, in which the influences of rotation and curvature were fully taken into account; the obtained results preliminarily reveal the characteristics of solid-liquid two-phase flow in a centrifugal pump. Tse and Wang [9] designed an efficient prognostic method to assess the performance degradation of a pump though extracting statistical features of vibration signals from on-site operating slurry pumps. This method has better prediction accuracy when compared to other procedures. Therefore, the research on the energy characteristics, vibration, and pressure fluctuation of a solid-liquid two-phase flow centrifugal pump has great significance.

At the same time, to improve the performance of the pump when they work under sediment-laden flow, researchers have found that spraying the anti-wear coating on the surface of wet parts is a good form of protection. Generally, coating material with better wear resistance, including epoxy resin mortar coatings [10] and [11], composite nylon coatings [12], polyurethane coatings [13] and other polymer coatings [14], alleviates the problem of the wear and tear of solid-liquid two-phase flow pumps. Luo et al. [15] sprayed a polyurethane coating on the surface of wet parts of a solid-liquid two-phase flow centrifugal pump and explored the performance of the centrifugal pump with different coating thickness coefficients under a water medium. He also measured internal flow, pressure fluctuations and radial force of the model pump and compared it with numerical simulation, which showed some similarity. Serrano et al. [16] analysed the wear volume of the impeller blade caused by the relative velocity of the mixture (water and sediment-laden) and the wear accumulated in an annual hydrological cycle was estimated mathematically. Tarodiya and Gandhi [17] experimentally and numerically investigated the performance of a centrifugal slurry pump and presented a numerical modelling approach to predict the performance and wear characteristics of the pump. Walker and Robbie [18] performed laboratory wear tests to measure the wear resistance of natural rubber and eutectic and hypereutectic white iron under abrasion conditions in a centrifugal slurry pump. Zhang [19] had shown that elastic polyurethane coating could reduce erosion wear damage caused by the sediment-laden flow on hydraulic machines operating at high speed, which could extend the service life of the pump impellers and turbine blades.

It can be seen from the above studies that the energy, vibration, and pressure fluctuation characteristics of the pump under sediment-laden flow are very different from those under the clear water flow medium. For both pressure pulsation and vibration, the greater the peak value, the greater the impact power on the device, and the higher the peak frequency, the higher the impact times on the device per unit time. After working for a long time, the small difference of vibration and pulsation may cause serious mechanical failures, such as bearing wear and shaft deformation. There are few studies on solid-liquid two-phase flow centrifugal pumps with protective coatings on blades. At present, the research in this area is mainly carried out through numerical simulations. Although numerical simulation is an effective method for predicting outcomes, accurate experiments are essential in research.

Therefore, a polyurethane coating with excellent wear resistance was applied on the blade pressure surface of a centrifugal pump, where the surface is most easily worn. The effect of the blade coating thickness coefficient on the energy, vibration and pressure fluctuation of a centrifugal pump operation under sediment-laden water flow was experimentally studied.

1 RESEARCH OBJECTIVE AND TEST SYSTEM

1.1 Selection of Coating Material

Applying protected coating on the blade can significantly improve the life of the pump. Our research group experimentally studied the abrasion resistance and cavitation erosion resistance of three materials (epoxy resin mortar, composite resin mortar and polyurethane), which are frequently used for the turbine blade as a protected coat, and concluded that polyurethane shows good performance [20]. Polyurethane coating has also been confirmed by Zhou et al. [21] and Zhong et al. [22], showing that it has numerous advantages including abrasion and cavitation resistance using in wet surface protection.

Therefore, polyurethane (curing agent, catalyst, stainless steel flake powder, weight ratio of acetophenone to acetone is 1:0.11:0.05 :0.4:1.25 : 1.25) was selected as the protective material used on the pressure surface of the blades and using 3D printing technology to make a mould to keep the shape and uniform, pouring the blade coating, and finally drying by airing.

1.2 The Model Pump

The single-stage single-suction horizontal centrifugal model pump with straight blades was used in the experiment. The design parameters of the model pump are as follows: design flow rate Q_d = 20 m³/h, head H = 22 m, efficiency η = 48 %, rated shaft power P = 1.5 kW, rotation speed n = 2900 rpm, and specific speed n_s = 84 The main geometric parameters of the model pump are shown in Table 1

Table 1. *Main parameters of the model pump*

Impeller	Inlet diameter [mm]	D_1	65
	External diameter [mm]	D_2	160
	Width of outlet [mm]	b_2	7
	Blade thickness [mm]	δ	6
	Number of blades	z	3
Volute	Inlet diameter [mm]	D_3	182
	Inlet width [mm]	b_3	26
	Outlet diameter [mm]	D_4	50

1.3 Experimental Test System

The schematics of the measuring station are shown in Fig. 1 The measuring station consists of piping, a water tank, outlet valve, a submersible pump, inlet valve, an electromagnetic flowmeter, a model pump with variable-frequency drive, a pressure fluctuation measuring system, a vibration measuring system, and an electric power measuring system.

Irrigation water, especially in China, features the diameter of particles in sediment-laden flow around 0.03 mm and an average bulk concentration of about 3 % [23]. Therefore, sediment-laden water under these features is selected as a working medium. A submersible pump is set in the water storage tank to prevent particles in sediment-laden water from settling, thus keeping the sediment-laden particle concentration in the pump during the test constant. The main parameters of submersible pump are as follows: design flow Q_d = 25 m³/h, head H = 8 m, rated shaft power P = 1.5 kW, rotational speed n = [illegible] r/min, and specific speed n_s = 0.5 The experimental test system is shown in Fig. 1

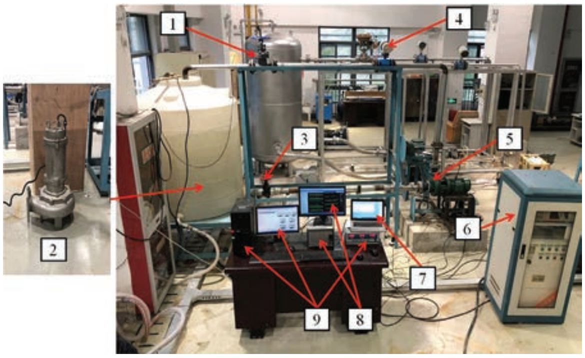

Fig. 1. *Test system; 1) outlet valve; 2) submersible pump; 3) inlet valve; 4) electromagnetic flowmeter; 5) model pump; 6) variable-frequency drive; 7) pressure fluctuation measuring system; 8) vibration measuring system; 9) energy performance measuring system*

The energy generated by vibration is directly related to the vibration velocity. By using the integral function in DASP (data acquisition and signal processing) software, the vibration acceleration is translated to the vibration velocity. The time-domain of the vibration signal is converted into the frequency domain diagram by using the fast Fourier transform (FFT) method. The vibration velocity (root mean square of velocity) is applied to evaluate the overall vibration. The vibration velocity is measured with an INV9[illegible] acceleration sensor (frequency interval from 0.5 kHz to 8 kHz, range of ±[illegible] times the acceleration of gravity, measurement error ±0.[illegible] %).

To measure vibration, sensors are located at the following locations: pump flange inlet, pump body, pump flange outlet and electric motor pedestal, as shown in Table 2 and Fig. 2.

Table 2. *Measurement locations for vibration measurements*

Point M_1	Point M_2	Point M_3	Point M_4
Flange inlet	Pump body	Flange outlet	Electric motor pedestal

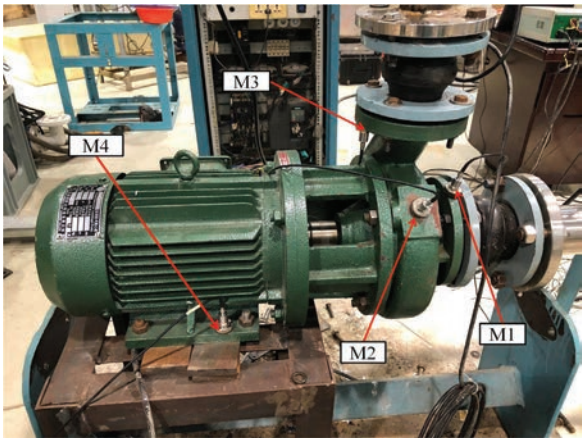

Fig. 2. *Measurement locations for vibration test*

The FFT is used to transform the pressure fluctuation time domain signal to the frequency domain. Dimensionless representation of pressure fluctuations is defined as follows:

$$C_p = \frac{\sqrt{\left(\frac{1}{N}\right)\left(p_i - \bar{p}\right)^2}}{0.5\rho u_2^2}. \tag{1}$$

Here, pressure fluctuation coefficient C_p is the root mean square value of the pressure fluctuation data measured at the measurement locations, divided by dynamic pressure. $\bar{p}$ and p_i are the average static pressure and fluctuating static pressure, respectively, while the unit is Pa. ρ is the medium density, the unit is kg/m³. N is the sample number. u_2 is the impeller outlet circumferential speed, and the unit is m/s.

The pressure fluctuation is measured with a CY301 intelligent digital pressure sensor (maximum frequency of 1 kHz, maximum absolute pressure of 300 kPa, measurement error ±0.10 %). The data acquisition and processing system for pressure fluctuations is shown in Fig. 3

The measurement location of pump outlet pressure fluctuation is set at 4 D downstream pipe diameter D distance from the flange. The pump head is the energy increase of liquid from the inlet to outlet of the pump generated by rotational impeller. The measurement locations of pump inlet and outlet pressure are set at 2 times the upstream and downstream pipe diameter distance from the flange, respectively. Locations of pressure measurements are shown in Fig. 4

Fig. 3. *Data acquisition and processing system for pressure fluctuations*

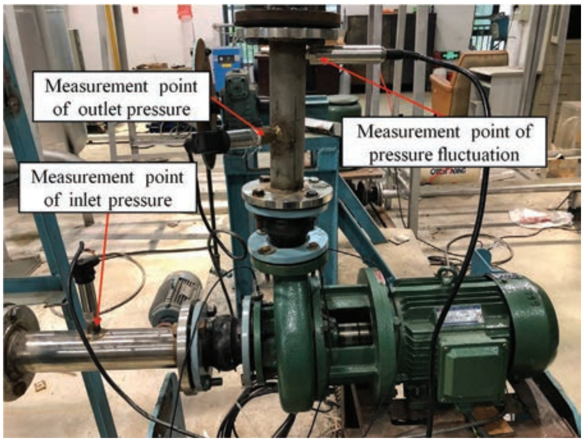

Fig. 4. *Measurement locations for pressure fluctuations*

Also, the flow is pumped from and returned to a 10 m³ tank. The rotational speed is measured by a speed sensor AR926 (rotation from 2.5 rpm to 10^5 rpm, measurement error ±0.05 %). The shaft torque is measured by a torque sensor of model CYT-302 (maximum torque 200 Nm, measurement error ±0.3 %). The static pressure is measured by a pressure sensor MIK-P300 (maximum static pressure of 1 MPa, measurement error ±0.1 %). The flow rate is measured by a magnetic flow meter KEFN (maximum flow rate of 100 m³/h, measurement error ±0.1 %). The collected data are analysed and processed when the test system is stable after a period of operation to ensure the validity of data.

1.4 Dimensionless Coating Thickness

We have used the coating thickness in its dimensionless form, as follows:

$$K_i = \frac{6\delta_i}{\delta}. \tag{2}$$

Here, K_i is the coating thickness coefficient, i is taken as 0, 1, 2, 3; δ_i is the coating thickness, unit is mm; δ is the blade thickness, in our case 6 mm.

The coating thicknesses δ_i are set as 0 mm, 1 mm, 2 mm, 3 mm, and the corresponding coating thickness coefficients are $K_0 = 0$, $K_1 = 1$, $K_2 = 2$, and $K_3 = 3$, respectively. The impellers with different coating thickness coefficients are shown in Fig. 5

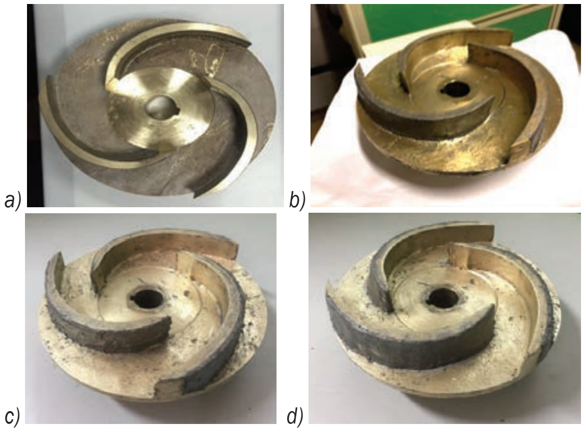

Fig. 5. *Impellers with different coating thickness coefficients; a) K_0; b) K_1, c) K_2; d) K_3*

2 RESULTS AND ANALYSIS

2.1 Energy Characteristics

Fig. 6 shows the energy characteristics of the model pump for four coating thickness coefficients under sediment-laden and clear water flow.

Fig. 6 shows that the head under sediment-laden flow is slightly larger than under clear water flow under the same coating thickness coefficient when the volumetric flow rate is below around 0.9 Q_d. According to [24], at low volumetric flow rates, this can be explained by the solid particles slightly decreasing disturbances near the wet surface, which reduces the turbulent boundary layer thickness and energy loss. However, the head under the sediment-laden flow decreases faster when the volumetric flow exceeds around 0.9 Q_d, because the whole velocity field of two-phase flow is more aberrant relative to the clear water flow. The velocity gradient is much greater under the large flow rate, which increases the loss generated by the velocity difference between water and particles. The contribution of this loss is more than the head increase from the disturbance elimination of particle swarm. Thus, the pump head is slightly lower than that under sediment flow under the larger flow rate.

In contrast, the head under both sediment-laden flow and clear water flow decreases significantly as the coating thickness coefficient increases. The theoretical pumping head H_t and efficiency η are derived from Euler equations, Eqs. (3) to (6) [24] and [25]. Here, u_1, u_2, v_{u1} and v_{u2} are the circumferential components of the inlet and outlet circumferential speed and absolute velocity, respectively; β_2 is blade angle at the exit; φ_2 is extrusion coefficient at impeller outlet; s_{u2} is blade outlet thickness; γ is the angle between the impeller outlet axis line and the streamline; h_0 is slip coefficient; is the pump efficiency; η_h is the pump hydraulic efficiency; η_v is the volumetric efficiency; η_m is the mechanical efficiency; P_0 is the power of liquid energy increase; P_e is the shaft power;

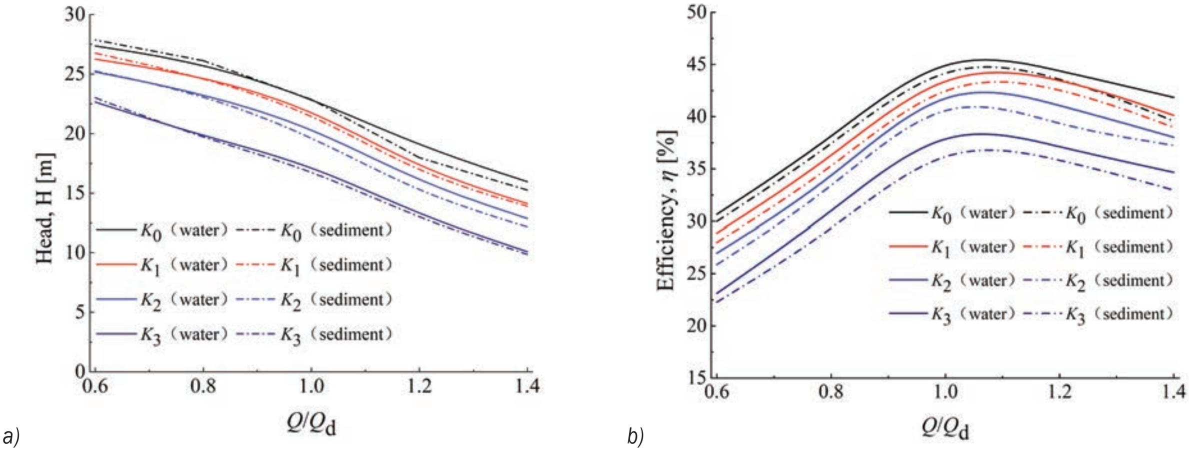

Fig. 6. *Energy characteristics for different coating thickness coefficients and working mediums; a) head; b) efficiency*

$$H_t = \frac{u_2 v_{u2} - u_1 v_{u1}}{g} = \\ = \frac{u_2}{g}\left(u_2 h_0 - \frac{Q_d}{\pi D_2 b_2 \varphi_2 \tan\beta_2}\right) - \frac{u_1 v_{u1}}{g}, \quad (3)$$

$$\varphi_2 = 1 - \frac{z s_{u2}}{\pi D_2} = 1 - \frac{z\delta}{\pi D_2 \sin\gamma \sin\beta_2^{'}}, \quad (4)$$

$$h_0 = 1 - \frac{\pi \sin\beta_2}{z}, \quad (5)$$

$$\eta = \eta_h \eta_v \eta_m = \frac{P_0}{P_e}. \quad (6)$$

Based on the formulas mentioned above, as the coating thickness increases, the blade thickness δ becomes larger. Since the coating is sprayed uniformly, the blade profile is unchanged, that is to say, D_2, γ and β_2 are not changed. Based on Eq. (3), it concludes that blade coating makes δ larger while φ_2 becomes smaller. Eq. (5) shows that the slip coefficient h_0 does not change. Therefore, the blade coating makes φ_2 smaller when other parameters remain unchanged. Based on Eq. (3), the theoretical head of the model pump is reduced; therefore, with the increase of the impeller coating thickness coefficient, the model pump head is gradually reduced.

From Fig. 6, the efficiency gradually decreases with the increase of the coating thickness coefficient for all flow rates. Based on Eq. (6), the pump efficiency η is related directly to the hydraulic efficiency η_h, the volumetric efficiency η_v, and the mechanical efficiency η_m. The hydraulic efficiency η_h will be the only changed parameter of the three above when the coating thickness coefficient varies. The liquid shock at blade inlet and swirl at the blade outlet will be more significant and make more energy loss under a larger coating thickness coefficient. Therefore, the pump efficiency η drops as the coating thickness coefficient increases.

At the same time, the pump efficiency under sediment-laden flow is slightly smaller than that under clear water flow. On the one hand, because of different density, viscosity and physical state, the velocities of solid and liquid at the same point are different, especially in highly turbulent flow, which increases the loss generated by the friction of solid-liquid flow. On the other hand, solid particles rush and hit the wet surface frequently, which generates energy loss. Based on Eq. (6), because of these two points

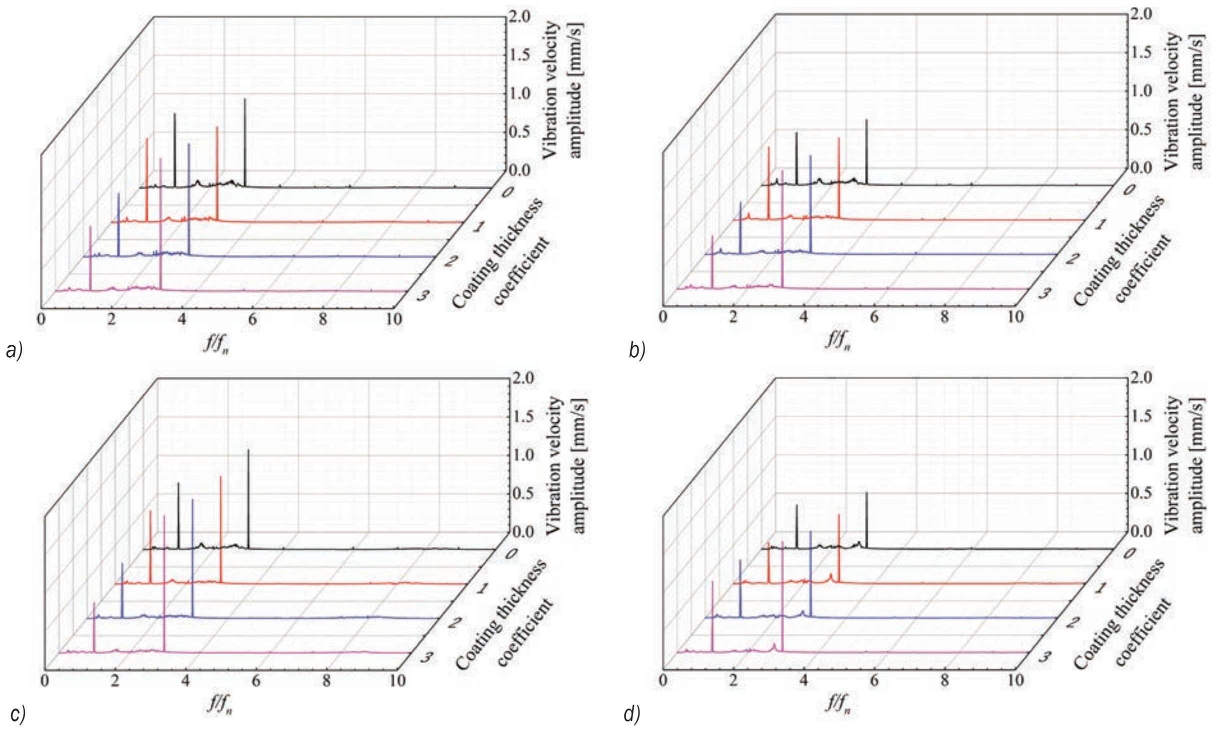

Fig. 7. *Frequency domain diagrams of vibration velocity at different measurement locations under clear water flow and design flow rate Q_d; at measurement locations: a) M_1; b) M_2; c) M_3; and d) M_4*

mentioned above, the hydraulic efficiency η_h under sediment flow is lower than that under clear water flow. As a result, the total efficiency η under sediment flow is lower than that under clear water flow.

2.2 Vibration Analysis

Fig. 7 shows the frequency domain diagrams of vibration velocity at different measurement locations under clear water flow.

Based on the above figure, the axis rotating frequency (ARF) (f_n) and blade passing frequency (BPF) (equal to 3 times f_n) are the main excitation frequencies of the pump vibration velocity at each measurement location. The vibration velocity amplitude at the frequency of 1 ARF is the largest at every measurement location and coating thickness coefficient. It is also proportional to the coating thickness coefficient.

The vibration velocity amplitude at the frequency of 1 BPF is just below that under the frequency of 1 ARF at every measurement location and coating thickness coefficient. The vibration velocity amplitude at the frequency of 1 ARF becomes the largest for the coating thickness coefficient K_1 at every measuring location except for location M_4.

Fig. 8 shows frequency domain diagrams of vibration velocity at different measurement locations under sediment-laden flow and design flow rate Q_d.

It can be seen that the characteristics of the vibration velocity at each measurement location under sediment-laden flow are the same as that under clear water flow.

A three-dimensional diagram of the relationship between the peak value of the vibration velocity amplitude and the coating thickness coefficient under design flow rate Q_d is shown in Fig. 9

The peak value of vibration velocity amplitude increases with the increase of the coating thickness coefficient under both sediment-laden flow and clear water flow. This is because of rotor-stator interaction between blade and volute tongue, and the thicker blade coating increases the liquid velocity at the blade outlet, which intensifies this kind of interaction. The thicker coating also means more rotating mass and more imbalance.

When the coating thickness coefficient is K_0, K_1 and K_2, the vibration velocity amplitude under sediment-laden flow is larger than under clear water

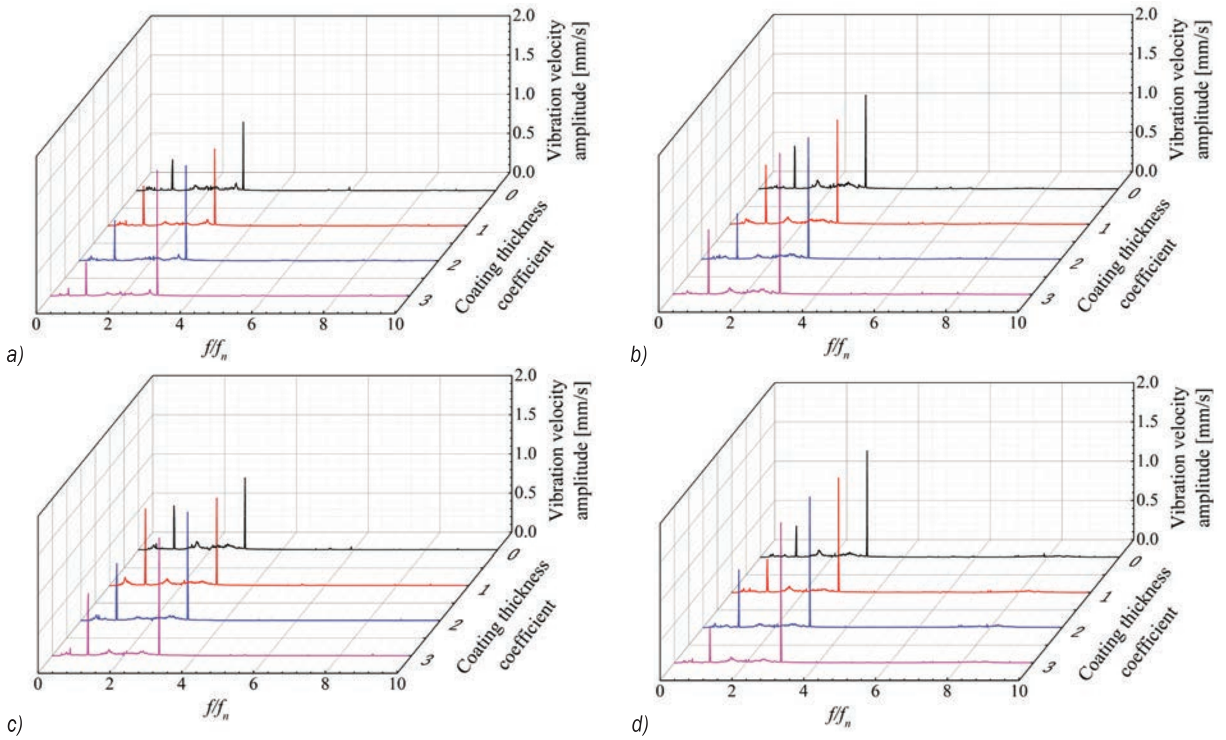

Fig. 8. *Frequency domain diagrams of vibration velocity under sediment-laden flow at measurement locations: a) M_1; b) M_2; c) M_3; and d) M_4*

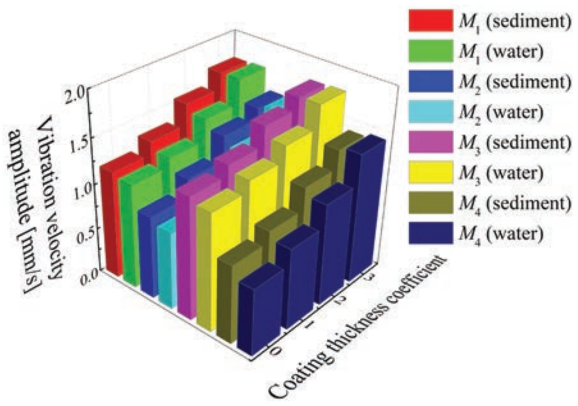

Fig. 9. *Three-dimensional column of the amplitude for the velocity of the vibration*

flow, but we see nearly no difference between them under the coating thickness coefficient K_3. The main reason is that the sediment particles of sediment-laden flow aggravate the instability or turbulence of the flow at volute tongue and a larger density of sediment-laden flow has a stronger interaction with volute. However, this kind of influence is covered by the negative effect of much large coating thickness coefficient on it. Therefore the vibration velocity amplitude does not show the difference between sediment-laden flow and water flow only on larger coating thickness coefficients.

2.3 Pressure Fluctuations

Fig. 10 shows the frequency domain diagrams of pressure fluctuations under different clear water flow rates and different coating thickness coefficients.

As shown in the above figure, the outlet pressure fluctuation features similar behaviour under different coating thickness coefficients and water flow rates. The ARF and BPF are the main excitation frequencies of the pump pressure fluctuation amplitude, and the pressure fluctuation at the frequency of 1 BPF is significantly larger than that at the frequency of 1 ARF. At the same time, the difference of the pressure fluctuation at the frequency of 1 ARF is not much different among experimental cases, which indicates that the effect and response of blade rotation on pressure fluctuation are more significant than axis rotation. Furthermore, under the same coating thickness coefficient, the peak pressure fluctuation under design flow rate Q_d is lower than that under off-design flow rates.

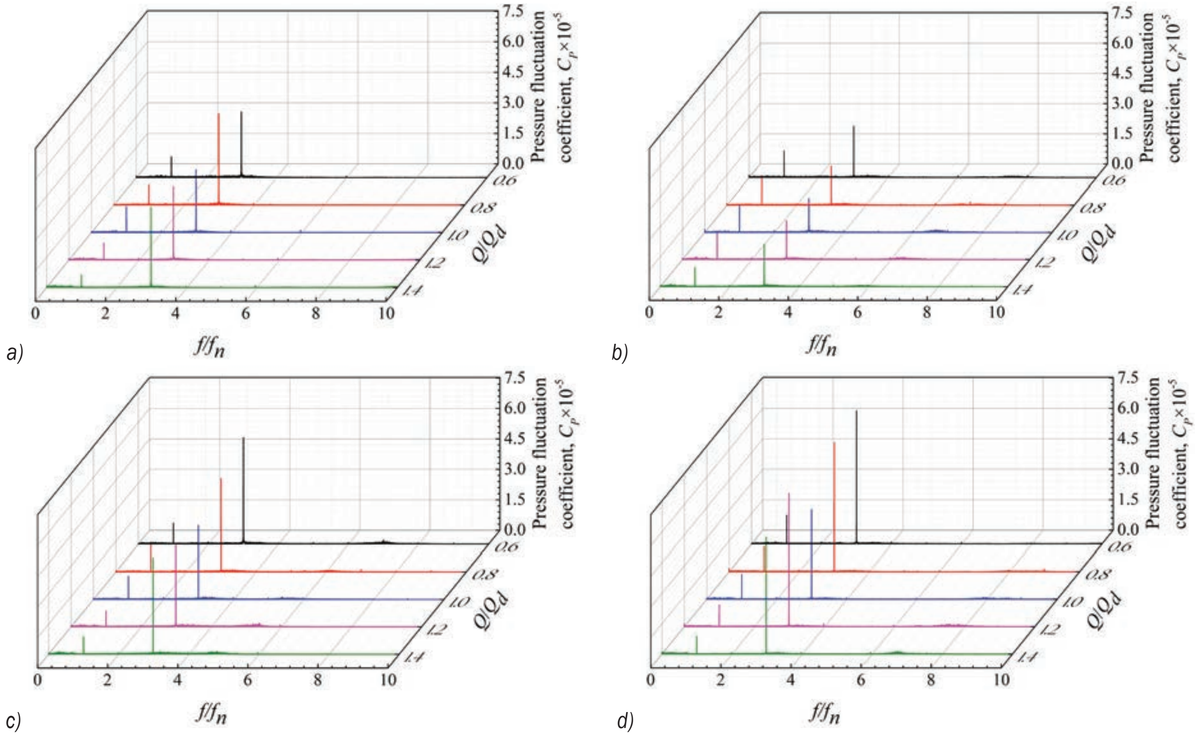

Fig. 10. *Frequency domain diagrams of pressure fluctuation under different clear water flow rates at coating thickness coefficients: a) K_1; b) K_2; c) K_3; and d) K_4*

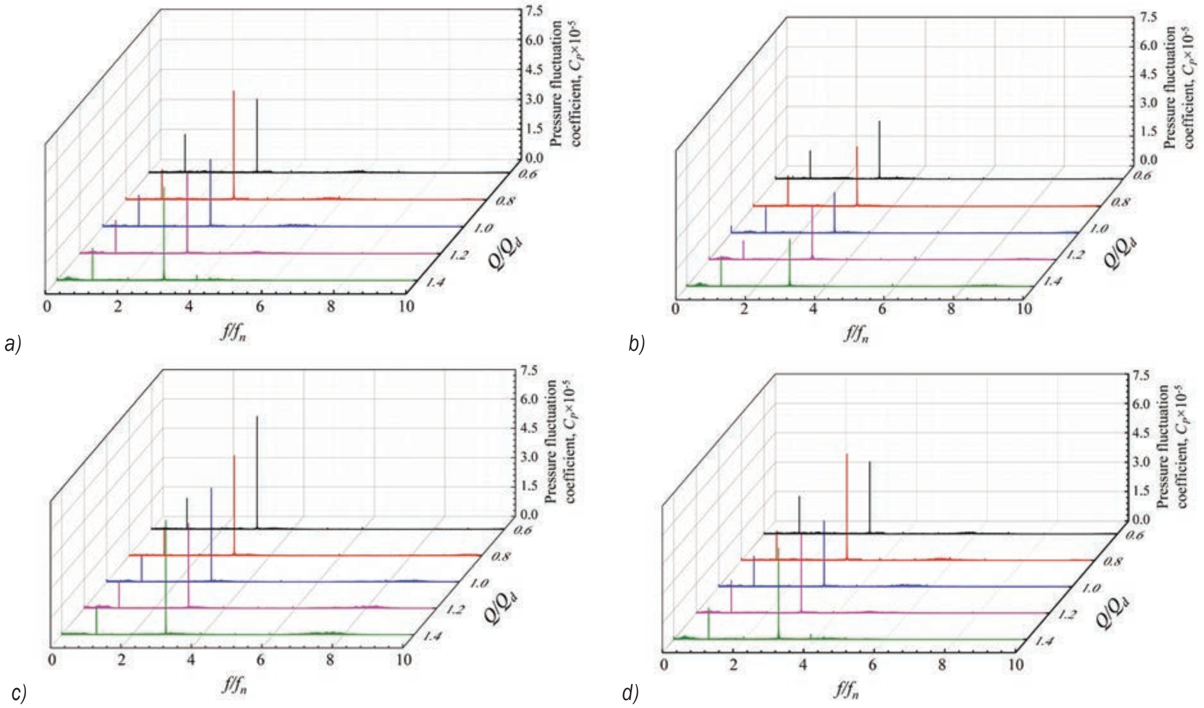

Fig. 11. Frequency domain diagrams of pressure fluctuation under different sediment-laden flow rates at coating thickness coefficients: a) K_1; b) K_2; c) K_3; and d) K_4

Fig. 11 shows the frequency domain diagrams of pressure fluctuation under different sediment-laden flow rates and different coating thickness coefficients. It can be seen that the characteristics of the pressure fluctuation under sediment-laden flow are basically the same as that under clear water flow.

Fig. 12 shows the line chart of peak pressure fluctuation.

As shown in the above figure, the variation trend of pressure fluctuation with increasing coating coefficient under both sediment-laden flow and clear water flow show similar behaviour.

Furthermore, under the same coating thickness coefficient, the peak value of pressure fluctuation under design flow rate Q_d is lower than that under off-design flow rates. The peak values of pressure fluctuation under different flow rates increase first and then decrease with the increasing coating thickness coefficient, and the lowest points are all located at the coating thickness coefficient K_1. The peak values

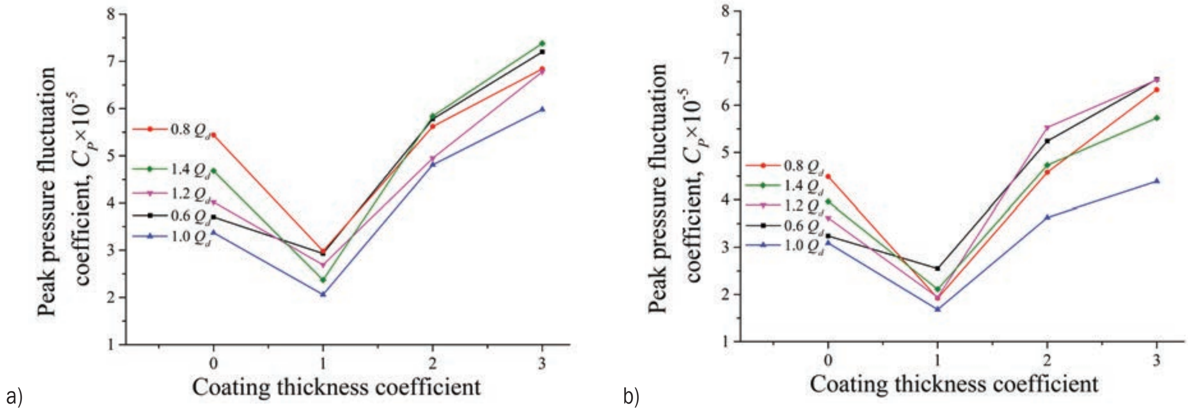

Fig. 12. *Line chart of peak pressure fluctuation; a) under clear water flow; b) under sediment-laden flow*

of pressure fluctuation under sediment-laden flow are higher than that under clear water flow when the working conditions are the same.

3 CONCLUSIONS

In this paper, energy, vibration and pressure fluctuation of a centrifugal pump with different polyurethane coating thickness coefficients were experimentally studied under sediment-laden flow. The conclusions are as follows:

1. The head H under both sediment-laden flow and clear water flow decreases significantly as the coating thickness coefficient increases. The head H under sediment-laden flow is slightly larger than that under clear water flow under the same coating thickness coefficient when the volumetric flow rate is up to around 0.9 Q_d. However, when the volumetric flow rate exceeds 0.9 Q_d, the opposite is true. The efficiency η gradually decreases with the increase of coating thickness coefficient for all flow rates, and the efficiency η under sediment-laden flow is slightly smaller than that under clear water flow.
2. The ARF and BPF are the main excitation frequencies of the pump vibration velocity amplitude and outlet pressure fluctuation in all cases. The peak value of the vibration velocity amplitude and outlet pressure fluctuation at the frequency of 1 BPF is the largest in all cases and that at the frequency of 1 ARF is just the second.
3. The peak value of vibration velocity amplitude is also proportional to the coating thickness coefficient. When the coating thickness coefficients are K_0, K_1 and K_2, the peak value of vibration velocity amplitude under sediment-laden flow is larger than that under clear water flow, but there is a very small difference between them for coating thickness coefficient K_3.
4. The difference of the pressure fluctuation at the frequency of 1 ARF varies little among different cases; however, that of 1 BRF is pretty obvious. For the same coating thickness coefficient, the peak pressure fluctuation under design flow rate Q_d is lower than that under off-design flow rates. The peak values of pressure fluctuation under different flow rates decrease first and then increase with the increasing coating thickness coefficient, and the lowest values are all found for the coating thickness coefficient K_1. The peak values of pressure fluctuation under sediment-laden flow are higher than that under clear water flow.

4 ACKNOWLEDGEMENTS

The authors would like to acknowledge the support given by the National Natural Science Foundation of China (926 and 956), and a project funded by the Priority Academic Program Development of Jiangsu Higher Education Institutions, Ministry of Education, Xihua University (szjj2016 088). The authors would like to thank the research program Energy Engineering P2-0401 funded by the Slovenian research agency ARRS.

5 NOMENCLATURES

Q_d nominal flow rate, [m³/h]
Q flow rate, [m³/h]
H pump head, [m]
H_t theoretical head, [m]
n rotational speed, [rpm]
N sample number
P rated shaft power, [kW]
n_s specific speeds
η efficiency, [%]
u_1 circumferential velocity of impeller at blade inlet, [m/s]
u_2 circumferential velocity of impeller at blade outlet, [m/s]
v_{u1} circumferential velocity of flow at blade inlet, [m/s]
v_{u2} circumferential velocity of flow at blade outlet, [m/s]
φ_2 extrusion coefficient at impeller outlet
s_{u2} thickness of blade at impeller outlet, [m]
γ angle between section line on axial plane and streamline at impeller outlet, [°]
h_0 slip coefficient
D_1 impeller inlet diameter, [mm]
D_2 impeller outlet diameter, [mm]
D_3 inlet diameter of volute, [mm]
D_4 outlet diameters of volute, [mm]
b_3 inlet width of volute, [mm]
z number of blades
$\overline{p}$ average static pressure, [Pa]
p_i fluctuating static pressure, [Pa]
δ thickness of blade, [mm]
δ_i thickness of blade coating , [mm]
ρ density, [kg/m³]
b_2 outlet impeller width, [mm]
f_n axis rotating frequency, [Hz]
K_i coating thickness coefficient,
C_p pressure fluctuation coefficient

6 REFERENCES

[1] Wang, Z.-Y., Qian, Z.-D. (2017). Effects of concentration and size of silt particles on the performance of a double-suction centrifugal pump. *Energy*, vol. 123, p. 36-46, **DOI:10.1016/j.energy.2017.01.142**.

[2] Jin, W. (2014). *Vibration Characteristics Analysis of Centrifugal Solid-Liquid Two-Phase Fluids Impeller*. MSc thesis, Liaoning Technical University, Liaoning.

[3] Rodriguez, C.G., Egusquiza, E., Santos, I.F. (2007). Frequencies in the vibration induced by the rotor stator interaction in a centrifugal pump turbine. *Journal of Fluids Engineering*, vol. 129, no. 11, p. 1428-1435, **DOI:10.1115/1.2786489**.

[4] Han, W., Yi, J., Ren, N.-L. Yue, T., Quan, H. (2015). Effects of particles on pressure fluctuation characteristics in centrifugal pump. *Journal of Drainage and Irrigation Machinery Engineering*, vol. 33, no. 6, p. 467-474, **DOI:10.3969/j.issn.1674-8530.14.1002**. (in Chinese)

[5] Kumar, S., Gandhi, B.K., Mohapatra, S.K. (2014), Performance characteristics of centrifugal slurry pump with multi-sized particulate bottom and fly ash mixtures. *Particulate Science and Technology*, vol. 32, no. 5, p. 466-476, **DOI:10.1080/02726351.2014.894163**.

[6] Zhao, B.-J, Yuan, S.-Q., Liu, H.-L., Huang, Z.-F., Tan, M.-G. (2008). Simulation of solid-liquid two-phase turbulent flow in double-channel pump based on mixture model. *Transactions of the Chinese Society of Agricultural Engineering*, vol. 24, no. 1, p. 7-12.

[7] Hazra, S.B., Steiner, K. (2007). Computation of dilute two-phase flow in a pump. *Journal of Computational and Applied Mathematics*, vol. 203, no. 2, p. 444-460, **DOI:10.1016/j.cam.2006.04.011**.

[8] Zhang, Y., Li, Y., Cui, B., Zhu, Z.-H., Dou, H.-S. (2013). Numerical simulation, analysis of solid-liquid two-phase flow in centrifugal pump. *Chinese Journal of Mechanical Engineering*, vol. 26, p. 53-60, **DOI:10.3901/CJME.2013.01.053**.

[9] Tse, P.W., Wang, D. (2015). Enhancing the abilities in assessing slurry pumps' performance degradation, estimating their remaining useful lives by using captured vibration signals. *Journal of Vibration and Control*, vol. 23, no. 12, p. 1925-1937, **DOI:10.1177/1077546315604522**.

[10] Golru, S.S., Attar, M.M., Ramezanzadeh, B. (2014). Studying the influence of nano-Al2O3 particles on the corrosion performance and hydrolytic degradation resistance of an epoxy/polyamide coating on AA-1050. *Progress in Organic Coatings*, vol. 77, no. 9, p. 1391-1399, **DOI:10.1016/j.porgcoat.2014.04.017**.

[11] Chairman, C.A., Kumaresh-Babu, S.P. (2013). Mechanical and abrasive wear behavior of glass and basalt fabric-reinforced epoxy composites. *Journal of Applied Polymer Science*, vol. 130, p. 120-130, **DOI:10.1002/app.39154**.

[12] Jin, J., Rafiq, R., Gill, Y.Q., Song, M. (2013). Preparation and characterization of high performance of graphene/nylon nanocomposites. *European Polymer Journal*, vol. 49, no. 9, p. 2617-2626, **DOI:10.1016/j.eurpolymj.2013.06.004**.

[13] Kim, B.K., Lee, J.C. (1996). Waterborne polyurethanes and their properties. *Journal of Polymer Science Part A: Polymer Chemistry*, vol. 34, no. 6, p. 1095-1104, **DOI:10.1002/(SICI)1099-0518(19960430)34:6<1095::AID-POLA19>3.0.CO;2-2**.

[14] Fu, J.J., Chen, T., Wang, M.D., Yang, N.W, Li, S.N, Wang, Y., Liu, X.D. (2013). Acid and alkaline dual stimuli-responsive mechanized hollow mesoporous silica nanoparticles as smart nanocontainers for intelligent anticorrosion coatings. *ACS Nano*, vol. 7, no. 12, p. 11397-11408, **DOI:10.1021/nn4053233**.

[15] Luo, K.-K., Wang, Y., Liu, H.-L., Dular, M., Chen, J. Zhang, Z.-L. (2019). Effect of coating thickness on a solid-liquid two-phase flow centrifugal pump under water medium. *Strojniški vestnik - Journal of Mechanical Engineering*, vol. 65, no. 4, p. 251-261, **DOI:10.5545/sv-jme.2018.5865**.

[16] Serrano, R.O.P., Santos L.P., Viana, E.M.F., Pinto, M.A., Martinez, C,B. (2018). Case study: Effects of sediment concentration on the wear of fluvial water pump impellers on Brazil's Acre river. *Wear*, vol. 408-409, p. 131-137, **DOI:10.1016/j.wear.2018.04.018**.

[17] Tarodiya, R., Gandhi, B.K. (2017). Hydraulic performance and erosive wear of centrifugal slurry pumps - a review. *Powder Technology*, vol. 305, p. 27-38, **DOI:10.1016/j.powtec.2016.09.048**.

[18] Walker, C.I., Robbie, P. (2013). Comparison of some laboratory wear tests and field wear in slurry pumps. *Wear*, vol. 302, no. 1-2, p. 1026-1034, **DOI:10.1016/j.wear.2012.11.053**.

[19] Zhang, R.-Z. (2014). Abrasion resistance analysis of spray polyurethane elastic coating on turbine blades. *Surface Technology*, vol. 43, no. 1, p. 11-15, **DOI:10.16490/j.cnki.issn.1001-3660.2014.01.014**.

[20] Chen, J. (2018). Effect of Coating on Operating Characteristics of Solid-Liquid Two-Phase Flow Centrifugal Pumps. MSc thesis, Jiangsu University, Jiangsu.

[21] Zhou, R., Lu, D.H., Jiang, Y.H., Li, Q.N. (2005). Mechanical properties and erosion wear resistance of polyurethane matrix composites. *Wear*, vol. 259, no. 1-6, p. 676-683, **DOI:10.1016/j.wear.2005.02.118**.

[22] Zhong, P., Peng, E.-G., Li, J., Xiao, X. (2007). Study of erosion behaviour of polyurethane-urea coating. *Tribology*, vol. 27, no. 5, p. 447-450, **DOI:10.3321/j.issn:1004-0595.2007.05.010**. (in Chinese)

[23] Sun, J.-H, Chai, Y., Wang, G.-L. (2010). Review on effects of sediment on the water quality of the Yellow River. *Journal of Sediment Research*, vol. 1, p. 72-80, **DOI:CNKI:SUN:NSYJ.0.2010-01-012**. (in Chinese)

[24] Liu, H. L., Tan, M.-G, Yuan, S.-Q. (2006). Research on calculation of theoretical head of centrifugal pumps. *Transactions of the Chinese Society for Agricultural Machinery*, vol. 37, no. 12, p. 87-90, **DOI:CNKI:SUN:NYJX.0.2006-12-021**. (in Chinese)

[25] He, X.-J., Lao, X.-S. (2009). Review of formulas for efficiency calculation of centrifugal pump. Pump technology, vol. 6, p. 24-27, **DOI:CNKI:SUN:SBJS.0.2009-06-007**. (in Chinese)

Strojniški vestnik - Journal of Mechanical Engineering 66(2020)10, 602-612

DOI:10.5545/sv-jme.2020.6755
Original Scientific Paper
Received for review: 2020-04-30
Received revised form: 2020-07-30
Accepted for publication: 2020-09-03

Prediction of Strain Limits via the Marciniak-Kuczyński Model and a Novel Semi-Empirical Forming Limit Diagram Model for Dual-Phase DP600 Advanced High Strength Steel

Ilyas Kacar[1,*] – Fahrettin Ozturk[2,3] – Serkan Toros[1] – Suleyman Kilic[4]
[1] Nigde Ömer Halisdemir University, Turkey
[2] Turkish Aerospace Industries, Inc., Turkey
[3] Ankara Yıldırım Beyazıt University, Turkey
[4] Kirsehir Ahi Evran University, Turkey

The prediction capability of a forming limiting diagram (FLD) depends on how the yield strength and anisotropy coefficients evolve during the plastic deformation of sheet metals. The FLD predictions are carried out via the Marciniak-Kuczynski (M-K) criterion with anisotropic yield functions for DP600 steel of various thicknesses. Then, a novel semi-empirical FLD criterion is proposed, and prediction capabilities of the criterion are tested with different yield criteria. The results show that the yield functions are very sensitive to anisotropic evolution. Thus, while the FLD curves from the M-K model and the proposed model are not the same for each thickness, the proposed model has better prediction than the M-K model.
Keywords: DP600, anisotropy, yield criterion, forming limit diagram, M-K failure criterion

Highlights

- *The most popular failure criterion, the Marciniak-Kuczynski, is compared to a novel semi-empirical failure criterion presented for sheet metals.*
- *The most appropriate and conservative yield function among anisotropic functions is the YLD2000-2d to be able to use with the failure criterion for DP600 sheet steel.*
- *The YLD2000-2d model parameters are presented for DP600 steel.*
- *Prediction capabilities for strain limits are presented on forming limit curves.*

0 INTRODUCTION

Some strategies on weight reduction have been developed for vehicles in transportation, one of which is to be able to use a thinner body without sacrificing strength requirements by using stronger sheet metal, known as advanced high strength steel (AHSS), which can provide weight saving due to its higher strength leading to thinner and lighter bodies. Therefore, its use in automobile body parts has been increased tremendously [1] to [3]. In AHSS, dual-phase (DP) steels are manufactured by holding low carbon steel at the austenite temperature for a while and then quenching. They include both ferrite and martensite, which come from the cooling of unstable austenite [4]. AHSSs have been increasingly used in automotive structural components, such as floor panels [5] and the trunk lid [6] due to their corrosion resistance, toughness, and high resistance to impact. However, it should be taken into consideration that carbon and nitrogen alloying elements decrease their formability. Numerous research studies have been carried out to enhance their mechanical behaviour, especially formability [7] to [11]. The determination of formability limitations is one of the requirements to achieve safer forming for sheet metals [12].

Using forming limit curves is one of the methods to determine necking initiation during deformation. These curves are based on stress (forming limit stress diagram (FLSD)) or strain (forming limit diagram (FLD)). This study focuses on the FLD and determines the formability limit and safe zone of the sheet material under various deforming conditions. It is also an efficient tool for diagnosing manufacturing defects. Sheet metals have their own specific FLD curves. Fig. 1 shows a typical FLD.

The FLD was introduced by Keeler and Backhofen [13], and Goodwin [14] developed their application to sheet metal forming problems. Although today an FLD consists of two curves known as right-left side curves, Keeler and Backhofen [13] first developed the right side of the FLD (positive minor strain side). Goodwin [14] extended the curve to the left side (negative minor strain side). Forming limit curves are determined by using a failure criterion based on necking. An accurate determination of neck initiation and propagation is not an easy task in sheet metals. Various deformation processes from uniaxial to biaxial loadings may

*Corr. Author's Address: Nigde Ömer Halisdemir University, Department of Mechatronics Engineering, Nigde 51240, Turkey, ikacar@gmail.com

cause different strain combinations. Also, material anisotropy has a significant effect on the strain pattern besides loading conditions [15] to [17]. Swift [18] and Hill [19] developed a failure criterion based on instability analysis to determine necking [18] and [19]. While Swift's criterion takes care of the maximum force's direction to determine diffuse necking, Hill's criterion, which is especially suitable for anisotropy in sheet metals, is based on discontinuity to determine localized necking. While the first has the ability to construct just the right-hand side of the FLD, which is useful when strains at all directions are positive, the other one constructs just its left-hand side. Thus, it is quite possible to take different results depending on the criterion. In recent years, one of the criteria is presented in the finite element codes to determine the FLD [20].

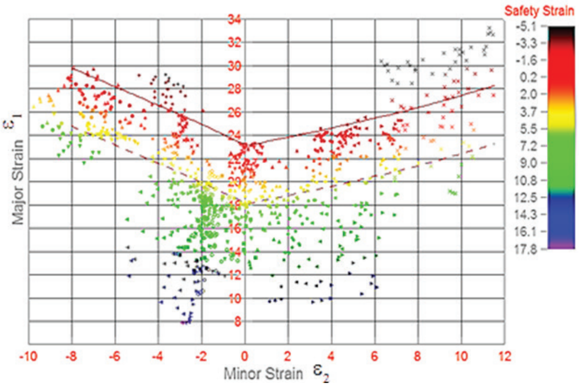

Fig. 1. *An example FLD from ASAME software*

Marciniak and Kuczynski [21] presented another instability criterion, known as the M-K model, based on force equilibrium. It can take into account geometric imperfection or inhomogeneity. Banabic et al. [22] compared their model to a maximum force criterion [23], diffusion based criterion [18], and the localized necking approach [19] to predict the FLD for a stamping process with a linear strain path by combining the M-K criterion and their orthotropic yield function, known as BBC2003 [24]. Later, it was developed as BBC2008 [25]. For a deep drawing simulation, the onset of necking was predicted, and yield surfaces were obtained via the M-K criterion [26]. Many comparative studies were collected on the FLD prediction [27]. As a result, it is seen that the M-K model is a preferred failure criterion due to its closer results to experimental data.

The present study shows FLD predictions from combined models of the M-K with some anisotropic yield criteria. The curves were evaluated through experimental data collected from DP600 steel. The most appropriate criterion to represent the anisotropy properly was determined. The model and its curves show its applicability and accuracy on various deformation types for DP600.

1 MATERIAL AND METHOD

DP steels are characterized by their microstructure where hard martensite grains are dispersed. Martensite grains provide high strength in the soft and ductile structure of the ferritic matrix. The strength is adjusted by the amount of martensite and carbon content. In this study, DP600 sheet was examined by means of uniaxial tensile tests with a 100 kN tensile test machine. Elongation was determined by its extensometer with two cameras. Specimens of 0.8 mm thickness were prepared from rolling in the diagonal (DD) and transverse (TD) directions, according to the ASTM E8 / E8 standard [28]. The strain rate was 0.008 s^{-1}. Initial yield point (σ_0), anisotropy coefficients (r-values), strength coefficient (K), and hardening exponent (n) were obtained to use as plasticity model parameters explained in the subsequent sections in detail [29]. The results were given in Table 1. Tensile curves were obtained, as seen in Fig. 2. Even small discrepancies were seen, all curves had similar shapes. Although the yield strength was approximately the same for all, the ultimate tensile strength and total elongations were different.

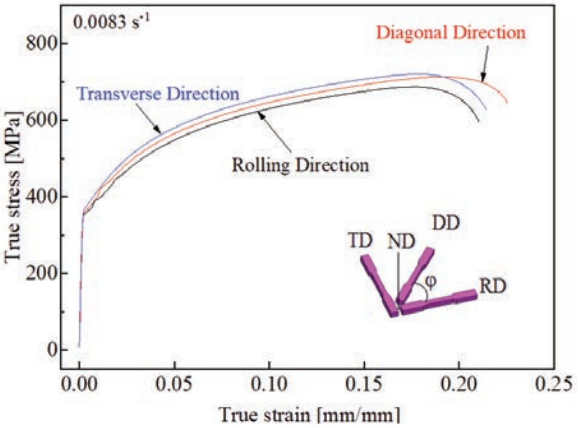

Fig. 2. *Tensile properties at different orientations for DP600 steel*

An experimental FLD curve was drawn using the out-of-plane formability test with 0.8 mm sheet thickness. The values for 1.6 mm and 2 mm were used from the literature [30]. The tensile test was done only for the thickness of 0.8 mm because mechanical properties were independent on the thickness. The experiments were repeated three times on a double-action special press machine with a 100 mm hemispherical punch. Before deformation, 2.5 mm × 2.5 mm square grids were printed on the sample surface. After deformation, strains on the deformed grids were detected by an image processing software ASAME©. The results were shown in Fig. 3. An offsetting procedure to reduce the size of the safe zone on the experimental FLD curve was applied as dashed lines. It increases the reliability as depicted in the Fig. 3

Table 1. *Tensile test results for DP600 sheet steel*

Direction	Yield strength [MPa]	r-value	Hardening exponent, n	Strength coefficient, K [MPa]
RD (0°)	355	0.89	0.194	979.46 (R^2=0.996)
DD (45°)	362	0.85	0.191	994.25 (R^2=0.996)
TD (90°)	371	1.12	0.188	1014.44 (R^2=0.997)

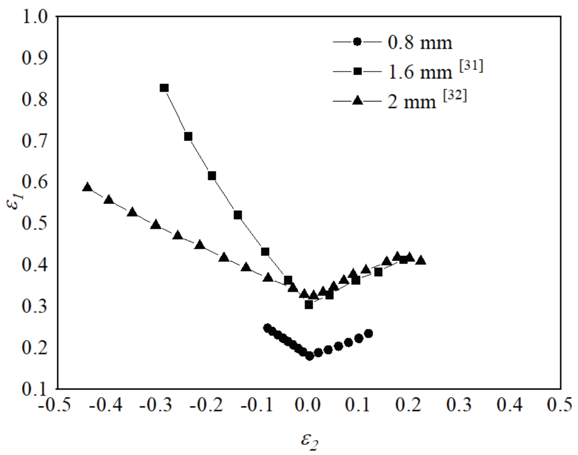

Fig. 3. *FLDs determined for various thicknesses (1.6 mm: [31], 2 mm: [32])*

While the area under the curves of the FLDs depicts the safe zone where the dashed line limits the safer zone, its size gives the material's forming ability. The more area under the FLD curve leads to a bigger safe zone for deformation. Strain limits depend on thickness and strain signs. While the bigger thickness leads to the more formability when the strain ε_2 has a positive sign, the formability decreases in the negative region contrary to expectations, especially for thicknesses 1.6 mm or 2 mm. Experiments with the 1.6 mm sample were carried out under in-plane deformation conditions while the other two were tested under out-of-plane conditions. The strain limit depends on the test method performed in-plane or out-of-plane deformation. Thus, a safety margin is used to eliminate the difference in practice.

2 YIELD CRITERIA

A plasticity model consists of a yield criterion to define an elastic to the plastic boundary, a hardening rule to model the evolution of this boundary during plastic deformation, and a flow rule to define plastic strain increment vector. Also, a failure criterion can be used in the case of failure estimates. The yield criterion's function produces one equivalent stress from stress components. In this study, the plasticity models were derived by using the Hill48, the Barlat89 and the YLD2000-2d functions.

2.1 Hill48

A yield formula of the quadratic Hill48 was given in Eq. (1) [33]:

$$2f\left(\sigma_{ij}\right) = F\left(\sigma_y - \sigma_z\right)^2 + G\left(\sigma_z - \sigma_x\right)^2 + H\left(\sigma_x - \sigma_y\right)^2 + 2L\tau_{yz}^2 + 2M\tau_{zx}^2 + 2N\tau_{xy}^2 = 1, \quad (1)$$

where x, y, z axes are mutually orthogonal. Its coefficients represent the anisotropic behaviour. The coefficients N, M, L, H, G, and F can be calculated by using anisotropy coefficients r_0, r_{45}, r_{90}, as in Eq. (2).

$$F = \frac{r_0}{r_{90}\left(1 + r_{90}\right)}, \qquad G = \frac{1}{\left(1 + r_0\right)},$$
$$H = \frac{r_0}{\left(1 + r_0\right)}, \qquad N = \frac{\left(r_0 + r_{90}\right) + \left(1 + r_{45}\right)}{2r_{90}\left(1 + r_0\right)}. \quad (2)$$

2.2 Barlat89

Another widely used anisotropic yield function in sheet metal deformation simulations was proposed by Barlat and Lian [34] (denoted as the Barlat89):

$$\varnothing = a\left|K_1 + K_2\right|^M + b\left|K_1 - K_2\right|^M + c\left|2K_2\right|^M = 2\bar{\sigma}^M, \quad (3)$$

where $\bar{\sigma}$ is the equivalent stress. M = 6 or 8 in the case of body-centred cubic or face-centred cubic microstructure. K_1 and K_2 are two invariants for stress tensor seen in Eqs. (4) to (6). Its coefficients; p, a, c, h characterize the anisotropic behaviour.

$$K_1 = \frac{\sigma_x + h\sigma_y}{2}, \qquad K_2 = \sqrt{\left(\frac{\sigma_x + h\sigma_y}{2}\right)^2 + p^2\tau_{xy}^2}, \quad (4)$$

$$a = 2 - c = 2 - 2\sqrt{\frac{r_0}{1 + r_0}\frac{r_{90}}{1 + r_{90}}}, \quad (5)$$

$$h = \sqrt{\frac{r_0}{1+r_0}\frac{1+r_{90}}{r_{90}}}, \qquad p = \frac{\bar{\sigma}}{\tau_{s1}}^{M}\sqrt{\left(\frac{2}{2a+2^{M}c}\right)}, \quad (16)$$

where *h*, *c*, and *a* can be computed based on *r*-values. However, *p* cannot be calculated directly but using some ways explained in **[34]**. τ_{s1} is yield point from shear stress test and $\tau_{s1}=\sigma_{xy}$ while $\sigma_{xx}=\sigma_{yy}=0$.

2.3 YLD2000-2d

Barlat et al. **[35]** presented another function known as the YLD2000-2d, which is more powerful to represent the anisotropy. It is described as follows:

$$f^{\frac{1}{M}} = \left\{\frac{\varnothing}{2}\right\}^{\frac{1}{M}} = \bar{\sigma}, \quad (17)$$

where $\bar{\sigma}$ is the equivalent stress and

$$\varnothing = \left|\tilde{S}_1^{'} - \tilde{S}_2^{'}\right|^{M} + \left|\tilde{S}_1^{''} + 2\tilde{S}_2^{''}\right|^{M} + \left|2\tilde{S}_1^{''} + \tilde{S}_2^{''}\right|^{M}, \quad (18)$$

where *M* is an exponent the same that of Barlat89 **[24]**. $\tilde{S}_k^{'}$ and $\tilde{S}_k^{''}$ (k = 1, 2) are principal stresses in the transformed domain when $\tilde{s}^{'}$ and $\tilde{s}^{''}$ are stress deviators. Transformations are linear based on $\tilde{s} = CS$.

$$\tilde{s}^{'} = C^{'}S = L^{'}\sigma, \quad (19)$$

$$\tilde{s}^{''} = C^{''}S = L^{''}\sigma, \quad (20)$$

where C' and C'' are matrices providing transformations. The $'$ and $''$ superscripts mean two different transformations. σ shows the stress state. T is a matrix including constants. The explicit forms of L' and L'' matrices are given in Eqs. (21) and (22).

$$\begin{bmatrix} L_{11}^{'} \\ L_{12}^{'} \\ L_{21}^{'} \\ L_{22}^{'} \\ L_{66}^{'} \end{bmatrix} = \begin{bmatrix} 2/3 & 0 & 0 \\ -1/3 & 0 & 0 \\ 0 & -1/3 & 0 \\ 0 & 2/3 & 0 \\ 0 & 0 & 1 \end{bmatrix} \begin{bmatrix} \alpha_1 \\ \alpha_2 \\ \alpha_7 \end{bmatrix}, \quad (21)$$

$$\begin{bmatrix} L_{11}^{''} \\ L_{12}^{''} \\ L_{21}^{''} \\ L_{22}^{''} \\ L_{66}^{''} \end{bmatrix} = \begin{bmatrix} -2 & 2 & 8 & -2 & 0 \\ 1 & -4 & -4 & 4 & 0 \\ 4 & -4 & -4 & 1 & 0 \\ -2 & 8 & 2 & -2 & 0 \\ 0 & 0 & 0 & 0 & 1 \end{bmatrix} \begin{bmatrix} \alpha_3 \\ \alpha_4 \\ \alpha_5 \\ \alpha_6 \\ \alpha_8 \end{bmatrix}, \quad (22)$$

where α_1 to α_8 are the YLD2000-2d function's parameters providing anisotropic effects. No direct formula to calculate them exists, so an inverse identification technic based on error minimization by referring to experimental yield strengths (σ_0, σ_{45}, σ_{90}, σ_b) and anisotropy coefficients (r_0, r_{45}, r_{90}, r_b) are applied to determine them. This method was explained in detail in **[36]**. To determine the YLD2000-2d yield function model's parameters, theoretical calculation of anisotropies and yield stresses, at different orientation angles were used. In the theoretical calculation of the biaxial stress and similarly in biaxial anisotropy calculation, it was assumed that $\sigma_b = \sigma_{11} = \sigma_{22}$. Equi-biaxial yield strength σ_b = [illegible] MPa was determined via the bulge test and biaxial anisotropy as r_b = 0.[illegible] is then determined with the help of hole expansion test **[37]**.

2.4 Application of the M-K Failure Criterion

This criterion assumes that the sheet metal includes a pre-existing thickness imperfection on the surface lying along the rolling direction. An imperfection factor is defined as $f_0 = \left(t_0^a / t_0^b\right)$ where t defines thickness. The imperfection free zone and imperfection's zone are denoted by '*a*' and '*b*' superscripts, respectively. Subscript 0 means anything at the beginning. If any biaxial stress increment is applied to a sheet metal, it leads to a strain increment in *a* and *b* sections. Necking initiates if the strain increment in section *b* is ten times higher than that of section *a* **[38]** to **[41]**. Force exerted in *a* and *b* must be in balance during loading, as explained in Eq. (23).

$$F_{nt}^{a} = F_{nt}^{b}, \qquad F_{nn}^{a} = F_{nn}^{b}, \quad (23)$$

where F is the force and n, t shows the normal and tangential axes. Similarly, both equations can be rewritten in terms of stresses as in Eq. (24).

$$\sigma_{nt}^{a} \cdot t_0^{a} e^{\varepsilon_3^{a}} = \sigma_{nt}^{b} \cdot t_0^{b} e^{\varepsilon_3^{b}}, \qquad \sigma_{nn}^{a} \cdot t_0^{a} e^{\varepsilon_3^{a}} = \sigma_{nn}^{b} \cdot t_0^{b} e^{\varepsilon_3^{b}}, \quad (24)$$

where t_0 is initial sheet thickness. σ_n and σ_{nt} are normal and tangential stresses. The strain component exerted through thickness in the normal axis is ε_3. The imperfection factor f can be generalized as in Eq. (25).

$$f = f_0 \cdot e^{\left(\varepsilon_3^{b} - \varepsilon_3^{a}\right)}, \quad (25)$$

where f_0 is initial imperfection factor. ε_3 can be determined by using incompressibility condition **[42]**. The stress components $\sigma_{nn}^{b}, \sigma_{tt}^{b}, \sigma_{nt}^{b}$, and effective strain increment $d\bar{\varepsilon}^{b}$ can be solved by means of simultaneous solution of four equations in Eq. (26).

$$
\begin{aligned}
F_1 &= \frac{d\varepsilon_{nn}^b \sigma_{nn}^b + d\varepsilon_{tt}^b \sigma_{tt}^b + d\varepsilon_{nt}^b \sigma_{nt}^b}{d\bar{\varepsilon}_b \bar{\sigma}_Y} - 1 = 0, \\
F_2 &= \frac{d\varepsilon_{tt}^b}{d\varepsilon_{tt}^a} - 1 = 0, \\
F_3 &= f\,\frac{\sigma_{nn}^b}{\sigma_{nn}^a} - 1 = 0, \\
F_4 &= f\,\frac{\sigma_{nt}^b}{\sigma_{nt}^a} - 1 = 0.
\end{aligned} \tag{16}
$$

Although these equations depend on the groove angle, the M-K model can be used without the groove angle by following the flowchart in [43]. The flowchart has been followed in this study. The f_0 parameter of the M-K model was taken as 0.99. The other parameters of the model depend on the strain and f_0.

2.5 The Proposed Failure Criterion

The FLD consists of two curves and one intersecting point depending on three deformation modes such as uniaxial, biaxial, and plane strain deformations. While uniaxial strains give points on the curve in the left-hand side, biaxial strains give points on the other curve in the right-hand side with respect to zero strain point in the horizontal axis. Both curves are intersected at a point corresponding to zero strain in the horizontal axis leading to one strain component, which causes to plane strain deformation. In the study, a novel semi-empirical FLD model was proposed, which was created via regression analysis of the experimentally obtained FLD diagrams of the several materials that were obtained by the other researches of the authors. During the modelling of the FLDs, the general mechanical properties that affect the FLDs of the materials were defined. As is well-known from the experiences and literature, the thickness and anisotropic features of the materials are the main characters that can change the FLDs. During the fitting analysis of the simple mathematical formulations, the constants were then constrained with the given experimental properties. The model consists of three formulas corresponding two curves and one intersecting point. The formulas are based on normal anisotropy r, biaxial anisotropy r_b, sheet thickness t, and strains as seen in Eq. (17).

$$
\varepsilon_1 = \begin{cases} -r\varepsilon_2 + FLD_0, & \varepsilon_2 < 0 \\ -r_b \varepsilon_2^{r_b/2} + FLD_0, & \varepsilon_2 > 0. \\ \text{where} \quad FLD_0 = \varepsilon_{eng\%} t^{3n} \end{cases} \tag{17}
$$

FLD_0 is the major strain at the point corresponding zero strain in the horizontal axis ($\varepsilon_2 = 0$). It depends on the engineering strain percentage $\varepsilon_{eg\%}$, sheet thickness t and hardening exponent n. Although there are many experiment types to determine the biaxial anisotropy, such as disk compression test [44], biaxial stretching test [45], or hole expansion test [46], it can also be calculated by using a flow rule, as in Eqs. (18) to (20), which gives the strain increment relation.

$$
d\varepsilon_{11} = d\lambda \frac{\partial f}{\partial \sigma_{11}} = d\bar{\varepsilon} \frac{\partial \bar{\sigma}}{\partial \sigma_{11}}, \tag{18}
$$

$$
d\varepsilon_{22} = d\lambda \frac{\partial f}{\partial \sigma_{22}} = d\bar{\varepsilon} \frac{\partial \bar{\sigma}}{\partial \sigma_{22}}, \tag{19}
$$

$$
r_b = \frac{\dfrac{\partial \bar{\sigma}}{\partial \sigma_{22}}}{\dfrac{\partial \bar{\sigma}}{\partial \sigma_{11}}}, \tag{20}
$$

where λ is a multiplier, $d\varepsilon$ gives true plastic strain increment. f is a scalar function defining “plastic potential’’. When the plastic potential function is $\bar{\sigma}$, this formula becomes the associated flow rule. σ_{11} and σ_{22} are plane stress states at the longitudinal and transverse axes with respect to the rolling axis.

2.6 Hardening Rule

An isotropic hardening rule presented by Hollomon as in Eq. (21) is used [47]. Thus the evolution on the stress σ_h due to hardening during plastic deformation is obtained.

$$
\sigma_h = K\varepsilon^n, \tag{21}
$$

where K is the strength coefficient, n stands for the strain-hardening exponent, and h means the isotropic hardening function. These are determined from curve fitting of tensile data.

3 RESULT AND DISCUSSIONS

While the parameters of the Hill48 and the Barlat89 can be determined from r-values, the YLD2000-2d’s coefficients were determined by optimization based on the nonlinear least-squares method. Kılıç et al. [48] explained an application of this optimization method in detail. The coefficients were calculated as in Table 2 for various thicknesses.

In any plastic deformation process, it is expected that the plasticity model should give the yield point

Table 2. *Coefficients of the yield functions*

	Thickness								
Hill48	Thickness	F		G		H		N	
	0.8 mm	0.4204		0.5291		0.4709		1.2819	
	1.6 mm	0.46		0.5754		0.4246		1.5304	
	2 mm	0.4035		0.5977		0.4023		1.5369	
Barlat89	Thickness	a		c		h		p	
	0.8 mm	1.0024		0.9976		0.9441		0.95	
	1.6 mm	1.0971		0.9029		0.9406		1.015	
	2 mm	1.1037		0.8963		0.8979		1.015	
YLD2000-2d	Thickness	α_1	α_2	α_3	α_4	α_5	α_6	α_7	α_8
	0.8 mm	1.0221	0.9387	1.0668	0.9766	0.9992	0.9806	0.9719	0.9778
	1.6 mm	1.011	0.9162	1.0651	0.9793	1.0048	0.9653	0.9729	0.9356
	2 mm	0.98	0.9431	1.078	0.9767	1.0075	0.951	0.9766	0.9281

and anisotropy predictions as accurately as possible. Therefore, the model performances were evaluated by their predictions on the yield strength and anisotropy coefficients depending on plane angle φ. Formulas derived based on plane stress transformations as in Eqs. (22) and (23) **[49]** were used to estimate the yield points and anisotropies.

$$\sigma_\varphi = \frac{\sigma_h}{F_\varphi}, \tag{22}$$

$$r_\varphi = \frac{F_\varphi}{\dfrac{\partial\bar{\sigma}}{\partial\sigma_{11}} + \dfrac{\partial\bar{\sigma}}{\partial\sigma_{22}}} - 1, \tag{23}$$

where F_φ includes trigonometric terms and comes from plane stress transformations. Its terms depend on yield criterion. σ_h stands for the isotropic hardening rule. $\bar{\sigma}$ is the equivalent stress, which comes from yield criterion. σ_φ is the yield strength and r_φ is the anisotropy coefficient at any angle φ in relation with the rolling direction. Experimental data obtained from the 0.8 mm DP600 steel sheet were used for comparisons. Figs. 4 and 5 show the prediction curves and experimental points. Stresses were normalized. The best fit to experimental points was given by YLD2000-2d. Its success is based on the criterion including eight parameters to be able to represent the anisotropy.

The yield function's responses were also investigated in the case of thickness variation in Figs. 6 to 8. The YLD2000-2d draws the same shape for all cases. The other two criteria exhibit some small differences when the thickness changes. All criteria predicted the same value for uniaxial tension/compression points at the rolling direction. The curves from the Hill48 and the Barlat89 criteria exhibited the most deviation when the thickness is 2 mm.

The yield surfaces for all yield criteria were compared when the thickness is 0.8 mm in Fig. 9. The stresses were predicted the same by all criteria for uniaxial tension/compression cases at rolling and transverse directions. They differed at biaxial and shear deformation regions. The most conservative one was the YLD2000-2d due to its smallest boundary.

FLD curves from the M-K and the proposed failure models were given in Figs. 10 and 11, respectively. Each model consists of the yield criteria and the failure criteria. Three M-K failure models, including the Hill48, the Barlat89, and the YLD2000 criteria, were compared to the experimental data for 0.8 mm, 1.6 mm, and 2 mm. The responses of the yield functions with the M-K failure criterion were investigated for thickness variation in Fig. 8. It is seen that while thickness <2 mm, the curves from the M-K models combined with the Hill48 or the YLD2000-2d were closer to the experimental data. For 2 mm, while the best representation of the right side was

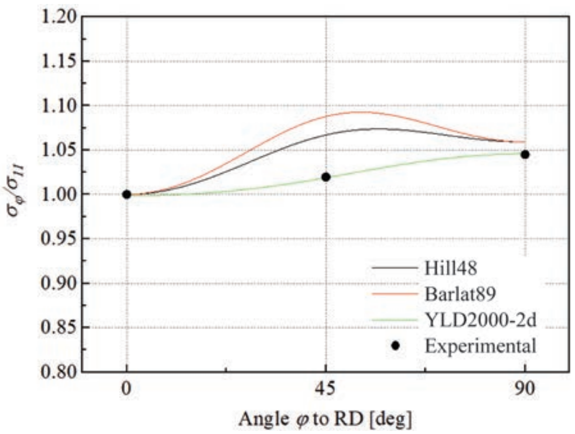

Fig. 4. *Yield stress predictions*

done by the models combined with the Hill48 and the YLD20002d, none of them provided a good fit for the left side. The YLD20002d gave conservative predictions on the right side curves for all cases.

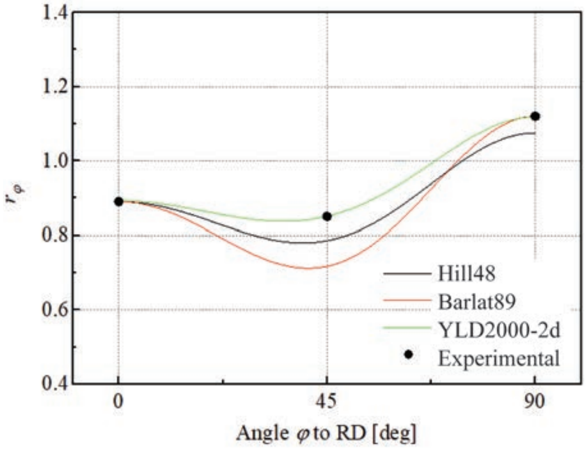

Fig. 5. *Anisotropy coefficients prediction*

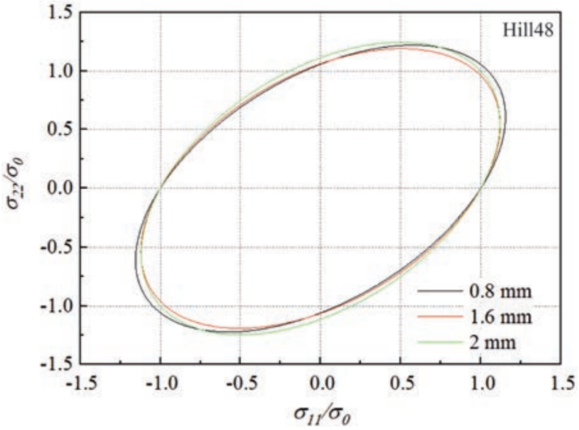

Fig. 6. *The yield contours predicted with the Hill-48 for different thicknesses*

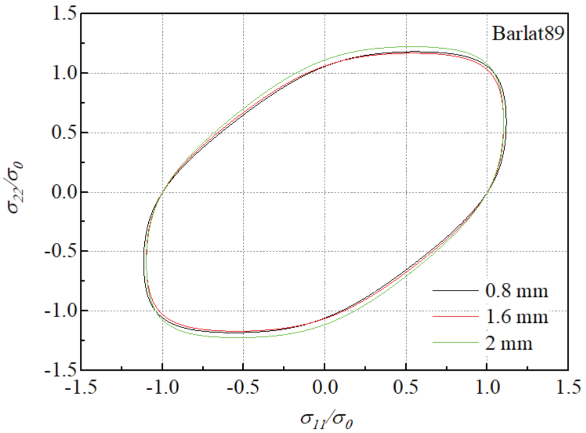

Fig. 7. *The yield contours predicted with the Barlat 89 for different thicknesses*

In the Fig. 11 the responses of the yield functions from the proposed model were given on the FLD curves. It is seen that the curves are in better agreement for all cases when compared to those from the M-K criterion. The proposed model was easier for calculations. The YLD20002d was more conservative at the right side for all cases.

In Fig. 12, when the YLD2000-2d criterion was used, the FLD curves from the M-K model and the proposed model were presented with the experimental curve. The proposed model was generally more convenient for the experiments.

4 CONCLUSIONS

The forming limits were investigated for DP600 steel. Anisotropic yield functions were used with the M-K model and a novel semi-empirical model. Prediction capabilities for strain limits were determined from

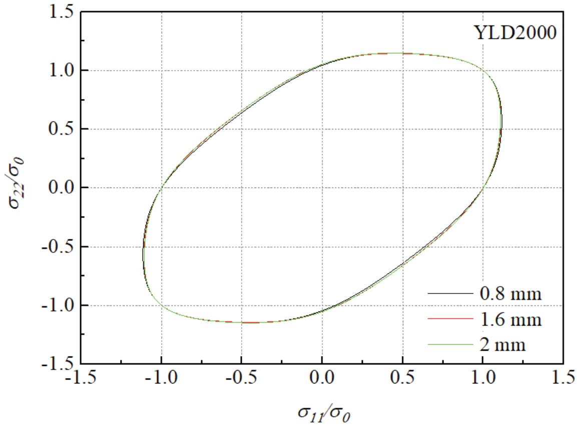

Fig. 8. *The yield contours predicted with the YLD2000-2d for different thicknesses*

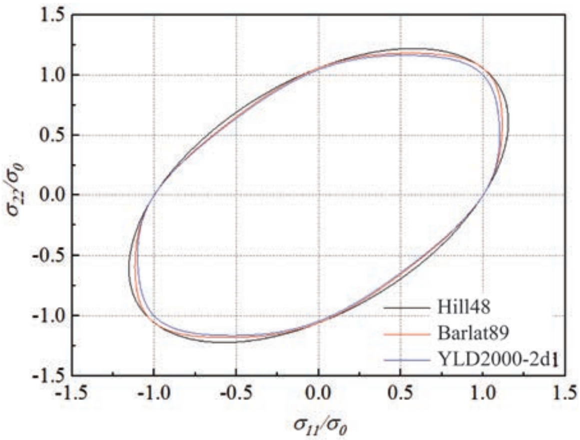

Fig. 9. *Comparison of yield functions*

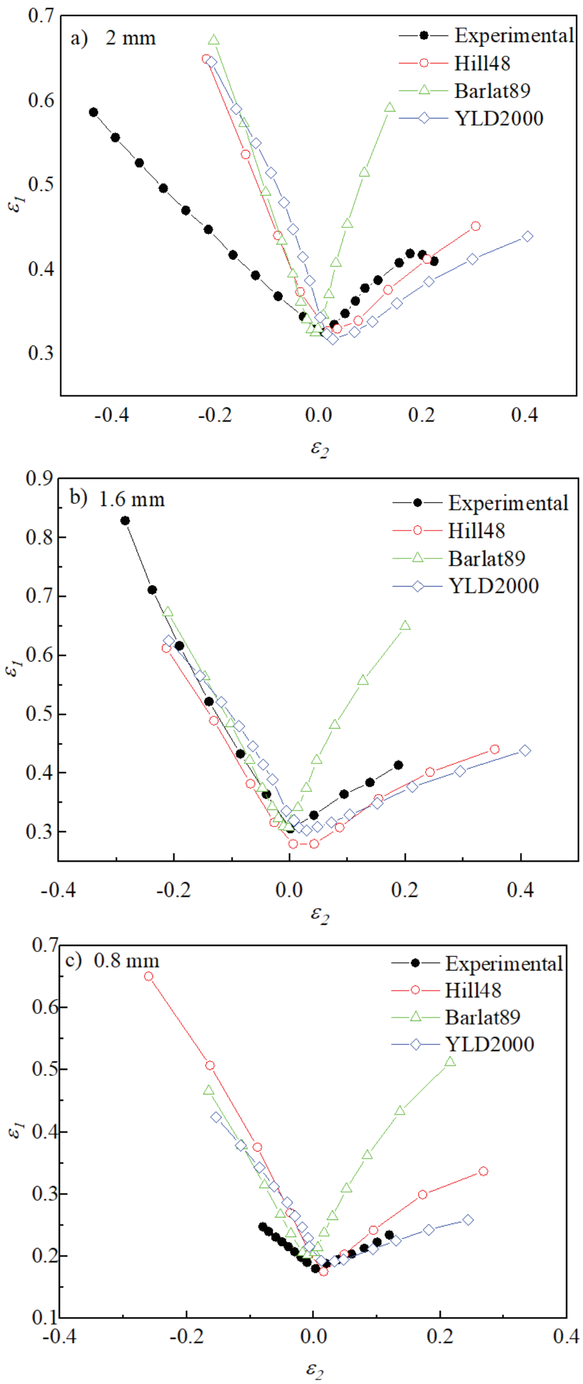

Fig. 10. *FLD curves from the M-K model and the yield criteria for thickness; a) 2 mm, b) 1.6 mm, and c) 0.8 mm*

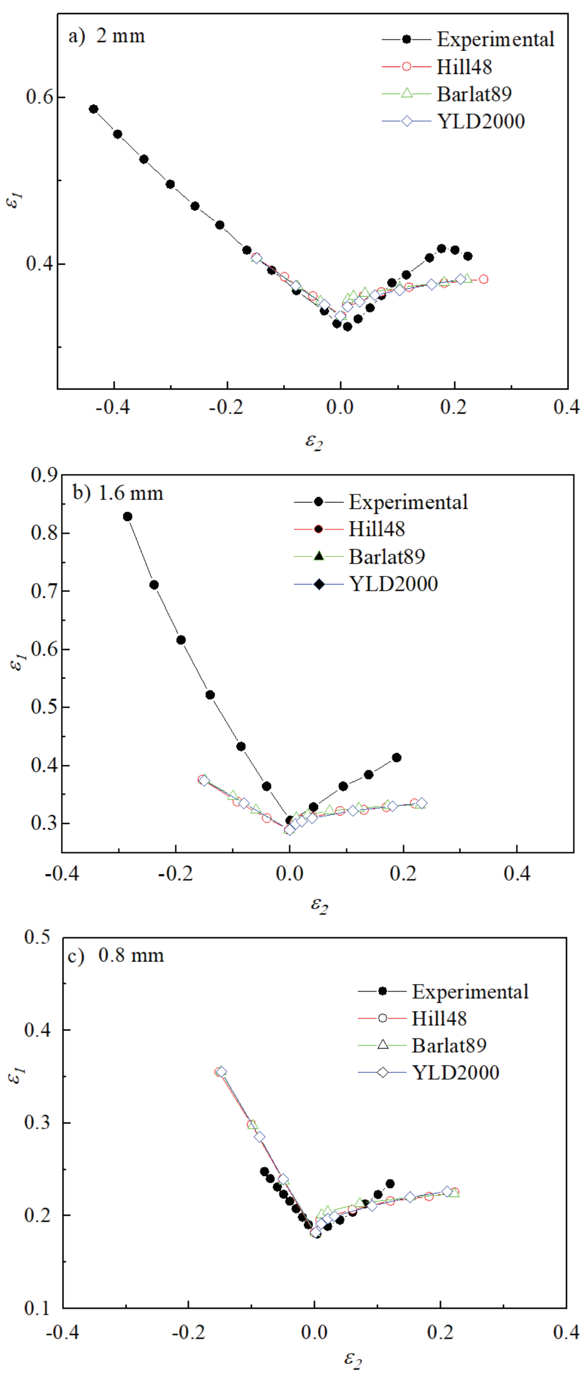

Fig. 11. *FLD curves from the proposed model and the yield criteria for thickness; a) 2 mm, b) 1.6 mm, and c) 0.8 mm*

both models. Finally, the following conclusions were drawn:

- The estimated yield locus, the anisotropy coefficients, and the normalized yield strengths for DP600 fit well with the experimental data for the YLD2000-2d criterion. It can simulate almost entire anisotropy coefficient and stress distribution depending on a plane angle between 0 and 90°. It works regardless of sheet thickness. Also, it is the most conservative one because it draws the smallest safe zone leading to the most reliable decision. The fact that it has more parameters gives more nonlinearity to be able to represent the cases with complex loading, such as biaxial deformation for which material anisotropy plays a significant role on the formability and defect occurrences. Therefore, this criterion is suitable for sheet metal deformation simulations.

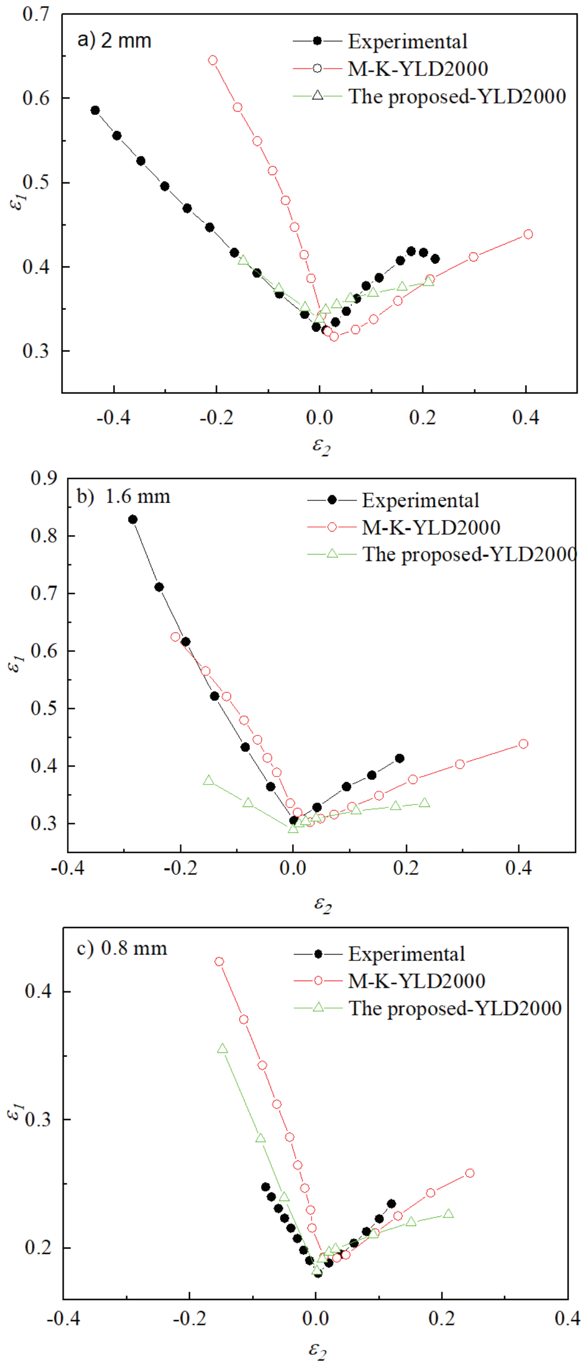

Fig. 12. *Comparison of the M K and the proposed criteria for thickness; a) 2 mm, b) 1.6 mm, and c) 0.8 mm*

- The YLD2000-2d represents the most suitable curve in the positive deformation zone of FLDs, which means that it can be preferred for failure predictions of DP600 sheet metals. Its consistency continues for all thickness for the sheet.
- When the sheet thickness is 2 mm, the Hill48 and the Barlat89 criteria show bigger deviation from the experimental curve. Thus, both criteria were consistent up to 2 mm sheet thickness.
- The proposed model combined with the YLD2000-2d gives the most precise failure predictions for DP600 sheet steels.
- Within the scope of this study, a failure criterion was presented for sheet metals. Further work for this research should be evaluated for the sheets thicker than 2 mm of DP600 and other AHSSs.

5 REFERENCES

[1] Kleiner, M., Chatti, S., Klaus, A. (2006). Metal forming techniques for lightweight construction. *Journal of Materials Processing Technology*, vol. 177, no. 1-3, p. 2-7, **DOI:10.1016/j.jmatprotec.2006.04.085**.

[2] Kleiner, M., Geiger, M., Klaus, A. (2003). Manufacturing of lightweight components by metal forming. *Cirp Annals-Manufacturing Technology*, vol. 52, no. 2, p. 521-542, **DOI:10.1016/S0007-8506(07)60202-9**.

[3] Neugebauer, R., Altan, T., Geiger, M., Kleiner, M., Sterzing, A. (2006). Sheet metal forming at elevated temperatures. *Cirp Annals-Manufacturing Technology*, vol. 55, no. 2, p. 793-816, **DOI:10.1016/j.cirp.2006.10.008**.

[4] Huh, H., Kim, S.B., Song, J.H., Lim, J.H. (2008). Dynamic tensile characteristics of trip-type and dp-type steel sheets for an auto-body. *International Journal of Mechanical Sciences*, vol. 50, no. 5, p. 918-931, **DOI:10.1016/j.ijmecsci.2007.09.004**.

[5] Golovashchenko, S.F., Gillard, A.J., Mamutov, A.V. (2013). Formability of dual phase steels in electrohydraulic forming. *Journal of Materials Processing Technology*, vol. 213, no. 7, p. 1191-1212, **DOI:10.1016/j.jmatprotec.2013.01.026**.

[6] Kamal Bashah, N.A., Muhamad, N., Md Deros, B., Zakaria, A., Ashari, S., Mobin, A., Mohd Abdul Lazat, M.S. (2013). Multi-regression modeling for springback effect on automotive body in white stamped parts. *Materials & Design*, vol. 46, no. 0, p. 175-190, **DOI:10.1016/j.matdes.2012.10.006**.

[7] Dong, D., Liu, Y., Yang, Y., Li, J., Ma, M., Jiang, T. (2014). Microstructure and dynamic tensile behavior of dp600 dual phase steel joint by laser welding. *Materials Science and Engineering A*, vol. 594, p. 17-25, **DOI:10.1016/j.msea.2013.11.047**.

[8] Farabi, N., Chen, D.L., Li, J., Zhou, Y., Dong, S.J. (2010). Microstructure and mechanical properties of laser welded dp600 steel joints. *Materials Science and Engineering*, vol. 527, no. 4-5, p. 1215-1222, **DOI:10.1016/j.msea.2009.09.051**.

[9] Nasser, A., Yadav, A., Pathak, P., Altan, T. (2010). Determination of the flow stress of five ahss sheet materials (dp 600, dp 780, dp 780-cr, dp 780-hy and trip 780) using the uniaxial tensile

and the biaxial viscous pressure bulge (VPB) tests. *Journal of Materials Processing Technology*, vol. 210, no. 3, p. 429-436, **DOI:10.1016/j.jmatprotec.2009.10.003**.

[10] Pepelnjak, T., Kayhan, E., Kaftanoglu, B. (2019). Analysis of non-isothermal warm deep drawing of dual-phase dp600 steel. *International Journal of Material Forming*, vol. 12, no. 2, p. 223-240, **DOI:10.1007/s12289-018-1400-0**.

[11] Ramazani, A., Abbasi, M., Prahl, U., Bleck, W. (2012). Failure analysis of dp600 steel during the cross-die test. *Computational Materials Science*, vol. 64, no. 0, p. 101-105, **DOI:10.1016/j.commatsci.2012.01.031**.

[12] Keeler, S.P. (1994). Application and forming of higher strength steel. *Journal of Materials Processing Technology*, vol. 46, no. 3-4, p. 443-454, **DOI:10.1016/0924-0136(94)90127-9**.

[13] Keeler, S., P., Backhofen, W., A. (1964). Plastic instability and fracture in sheet stretched over rigid punches. *ASM Trans. Quart*, vol. 56, p. 25-48.

[14] Goodwin, G.M. (1968). Application of strain analysis to sheet metal forming in the press shop. SAE paper, vol. 680093, **DOI:10.4271/680093**.

[15] Aleksandrović, S., Stefanović, M., Adamović, D., Lazić, V. (2009). Variation of normal anisotropy ratio “r” during plastic forming. *Strojniški vestnik - Journal of Mechanical Engineering*, vol. 55, no. 6, p. 392-399.

[16] Satošek, R., Valeš, M., Pepelnjak, T. (2019). Study of influential parameters of the sphere indentation used for the control function of material properties in forming operations. *Strojniški vestnik - Journal of Mechanical Engineering*, vol. 65, no. 10, p. 585-598, **DOI:10.5545/sv-jme.2019.6312**.

[17] Starman, B., Vrh, M., Halilovič, M., Štok, B. (2014). Advanced modelling of sheet metal forming considering anisotropy and young’s modulus evolution. *Strojniški vestnik - Journal of Mechanical Engineering*, vol. 60, no. 2, p. 84-92 **DOI:10.5545/sv-jme.2013.1349**.

[18] Swift, H.W. (1952). Plastic instability under plane stress. *Journal of the Mechanics and Physics of Solids*, vol. 1, no. 1, p. 1-18, **DOI:10.1016/0022-5096(52)90002-1**.

[19] Hill, R. (1952). On discontinuous plastic states, with special reference to localized necking in thin sheets. *Journal of the Mechanics and Physics of Solids*, vol. 1, p. 19-30, **DOI:10.1016/0022-5096(52)90003-3**.

[20] Petek, A., Pepelnjak, T., Kuzman, K. (2005). An improved method for determining a forming limit diagram in the digital environment. *Strojniški vestnik - Journal of Mechanical Engineering*, vol. 51, no. 6, p. 16330-345.

[21] Marciniak, Z., Kuczyński, K. (1967). Limit strains in the processes of stretch-forming sheet metal. *International Journal of Mechanical Sciences*, vol. 9, no. 9, p. 609-620, **DOI:10.1016/0020-7403(67)90066-5**.

[22] Banabic, D., Aretz, H., Paraianu, L., Jurco, P. (2005). Application of various fld modelling approaches. *Modelling and Simulation in Materials Science and Engineering*, vol. 13, no. 5, p. 759-769, **DOI:10.1088/0965-0393/13/5/009**.

[23] Hora, P., Tong, L., Reissner, J. (1996). A prediction method for ductile sheet metal failure in fe-simulation. *Numisheet ’96*, p. 252-256.

[24] Banabic, D., Aretz, H., Comsa, D.S., Paraianu, L. (2005). An improved analytical description of orthotropy in metallic sheets. *International Journal of Plasticity*, vol. 21, no. 3, p. 493-512, **DOI:10.1016/j.ijplas.2004.04.003**.

[25] Vrh, M., Halilovič, M., Starman, B., Štok, B., Comsa, D.-S., Banabic, D. (2014). Capability of the bbc2008 yield criterion in predicting the earing profile in cup deep drawing simulations. *European Journal of Mechanics - A/Solids*, vol. 45, p. 59-74, **DOI:10.1016/j.euromechsol.2013.11.013**.

[26] Arrieux, R., Brunet, M., Vacher, P., Nhat, T.N. (1996). A method to predict the onset of necking in numerical simulation of deep drawing operations. *CIRP Annals*, vol. 45, no. 1, p. 255-258, **DOI:10.1016/S0007-8506(07)63058-3**.

[27] Slota, J., Spisak, E. (2005). Comparison of the forming-limit diagram (FLD) models for drawing quality (DQ) steel sheets. *Metalurgija*, vol. 44, no. 4, p. 249-253.

[28] ASTM E8 / E8M (2004). Standard test methods for tension testing of metallic materials. *American Society for Testing and Materials*, vol. E8, West Conshohocken.

[29] Hollomon, J.H. (1945). Tensile deformation. *Transactions of the Metallurgical Society of AIME*, vol. 162, p. 268-290.

[30] Ozturk, F., Lee, D. (2005). Experimental and numerical analysis of out-of-plane formability test. *Journal of Materials Processing Technology*, vol. 170, no. 1–2, p. 247-253, **DOI:10.1016/j.jmatprotec.2005.05.010**.

[31] Buranathiti, T. (2007). Simulation and benchmark of an automotive underbody cross member panel. *ASIMMOD2007*, p. 107-113.

[32] Tigrinho, L.M.V., Filho, R.A.C., Neto, R.d.C.B., Lajarin, S.F., Marcondes, P.V.P. (2011). Forming analyses of dp600 steel using different blank-holder pressures. *21st Brazilian Congress of Mechanical Engineering*, p. 112-122.

[33] Hill, R. (1948). A theory of the yielding and plastic flow of anisotropic metals. *Proceedings of the Royal Society A* vol. 193, p. 281-297, **DOI:10.1098/rspa.1948.0045**.

[34] Barlat, F., Lian, K. (1989). Plastic behavior and stretchability of sheet metals. Part i: A yield function for orthotropic sheets under plane stress conditions. *International Journal of Plasticity*, vol. 5, no. 1, p. 51-66, **DOI:10.1016/0749-6419(89)90019-3**.

[35] Barlat, F., Brem, J.C., Yoon, J.W., Chung, K., Dick, R.E., Lege, D.J., Pourgoghrat, F., Choi, S.H., Chu, E. (2003). Plane stress yield function for aluminum alloy sheets - part 1: Theory. *International Journal of Plasticity*, vol. 19, no. 9, p. 1297-1319, **DOI:10.1016/s0749-6419(02)00019-0**.

[36] Maček, A., Starman, B., Mole, N., Halilovič, M. (2020). Calibration of advanced yield criteria using uniaxial and heterogeneous tensile test data. *Metals*, vol. 10, p. 542, **DOI:10.3390/met10040542**.

[37] Hosford, W.F. (1972). A generalized isotropic yield criterion. *Journal of Applied Mechanics*, vol. 39, no. 2, p. 607-609, **DOI:10.1115/1.3422732**.

[38] Butuc, M.C., Banabic, D., da Rocha, A.B., Gracio, J.J., Duarte, J.F., Jurco, P., Comsa, D.S. (2002). The performance of YLD96 and bbc2000 yield functions in forming limit prediction. *Journal of Materials Processing Technology*, vol. 125, p. 281-286, **DOI:10.1016/s0924-0136(02)00399-0**.

[39] Butuc, M.C., da Rocha, A.B., Gracio, J.J., Duarte, J.F. (2002). A more general model for forming limit diagrams prediction.

Journal of Materials Processing Technology, vol. 125-126, p. 213-218, DOI:10.1016/S0924-0136(02)00315-1

[40] Cao, J., Yao, H., Karafillis, A., Boyce, M.C. (2000). Prediction of localized thinning in sheet metal using a general anisotropic yield criterion. *International Journal of Plasticity*, vol. 16, no. 9, p. 1105-1129, DOI:10.1016/s0749-6419(99)00091-1.

[41] Yao, H., Cao, J. (2002). Prediction of forming limit curves using an anisotropic yield function with prestrain induced backstress. *International Journal of Plasticity*, vol. 18, no. 8, p. 1013-1038, DOI:10.1016/S0749-6419(01)00022-5.

[42] Grobbelaar, M. (2020). Lifting plate incompressibility condition for stability of a magnetoelastic mindlin–timoshenko model. *Applied Mathematics Letters*, vol. 102, p. 106084, DOI:10.1016/j.aml.2019.106084.

[43] Kılıç, S., Öztürk, F. (2016). Comparison of commercial twip900 and dp600 high strength steels in the automotive industry. *Gazi University Journal of Engineering and Architecture*, vol. 31, no. 3, p. 567-578, DOI:10.17341/gummfd.81389.

[44] Zillmann, B., Wagner, M.F.X., Schmaltz, S., Schmidl, E., Lampke, T., Willner, K., Halle, T. (2015). In-plane biaxial compression and tension testing of thin sheet materials. *International Journal of Solids and Structures*, vol. 66, p. 111-120, DOI:10.1016/j.ijsolstr.2015.03.031.

[45] Takuda, H., Mori, K., Takakura, N., Yamaguchi, K. (2000). Finite element analysis of limit strains in biaxial stretching of sheet metals allowing for ductile fracture. *International Journal of Mechanical Sciences*, vol. 42, no. 4, p. 785-798, DOI:10.1016/S0020-7403(99)00018-1.

[46] Xu, L., Barlat, F., Lee, M.-G. (2012). Hole expansion of twinning-induced plasticity steel. *Scripta Materialia*, vol. 66, no. 12, p. 1012-1017, DOI:10.1016/j.scriptamat.2012.01.062.

[47] Hollomon, J.R. (1945). Tensile deformation. *Transaction of AIME*, vol. 162, no. 1, p. 268–277.

[48] Kılıç, S., Toros, S., Kacar, İ., Öztürk, F. (2018). Lüy, Ö.T.M., Çam, E., Barışçı, N., Demirbaş, M.D., Güçyetmez, M. (eds.). *Scientific and Professional Studies-Engineering and Technology in the World of the Future*, Ekin press, Bursa, p. 271-290.

[49] Banabic, D., Carleer, B., Comsa, D.-S., Kam, E., Krasovskyy, A., Mattiasson, K., Sester, M., Sigvant, M., Zhang, X. (2010). *Sheet Metal Forming Processes: Constitutive Modelling and Numerical Simulation*. Springer-Verlag Berlin Heidelberg.

Strojniški vestnik - Journal of Mechanical Engineering 66(2020)10, 613-626

DOI:10.5545/sv-jme.2020.6704
Original Scientific Paper
Received for review: 2020-04-03
Received revised form: 2020-07-30
Accepted for publication: 2020-09-01

Research on a Noise Reduction Method Based on DTCWT and the Cyclic Singular Energy Difference Spectrum

Xihui Chen[1,2,*] – Gang Cheng[2,4] – Ning Liu[3] – Xinhui Shi[1] – Wei Lou[1]
[1] Hohai University, College of Mechanical and Electrical Engineering, China
[2] China University of Mining and Technology, School of Mechatronic Engineering, China
[3] China Coal Technology and Engineering Grope Shanghai Co., Ltd., China
[4] Shandong Zhongheng Optoelectronic Technology Co., Ltd., China

The gear is the most important part of the transmission system of mechanical equipment, and the monitoring and diagnosis of it can improve the reliability of mechanical equipment. However, mechanical equipment generally works in harsh working conditions. The gear vibration signal is subjected to strong noise interference in working conditions, which brings great challenges for the effective diagnosis of gear faults. This paper proposed a noise reduction method based on the dual-tree complex wavelet transform (DTCWT) and cyclic singular energy difference spectrum. First, the gear vibration signal containing strong noise interference is decomposed into a series of signal components with different frequency characteristics by using the time-frequency analysis ability of DTCWT. Then, cyclic singular energy difference spectrum is proposed based on the idea of a cascaded cycle and the successive elimination of noise interference to process each signal component with different frequency characteristics, and the termination conditions of cyclic singular energy difference spectrum can be set according to the noise interference distribution characteristics in different frequency bands. The final noise reduction of the original gear vibration signal can be realized based on signal reconstruction after the noise reduction processing of each signal components with different frequency bands. Finally, experiments are carried out to verify the effectiveness of the proposed method, which is effective and suitable for the noise reduction of the vibration signal.

Keywords: noise reduction, DTCWT, singular value decomposition, cyclic singular energy difference spectrum, vibration signal

Highlights

- *A noise reduction method based on dual-tree complex wavelet transform and cyclic singular energy difference spectrum is proposed.*
- *The cyclic singular energy difference spectrum is proposed based on the idea of a cascaded cycle and the successive elimination of noise interference.*
- *The adaptive selection methods of some parameters are applied to the proposed cyclic singular energy difference spectrum.*
- *The simulated signals and experimental signals are used to verify the proposed method, which proves that the proposed method can effectively eliminate noise interference.*

0 INTRODUCTION

The gear is the most important part of mechanical equipment and is mainly responsible for the transmission of motion and power. On-line monitoring and fault diagnosis of gear is crucial in ensuring the safe operation of mechanical equipment [1] and [2]. At present, the vibration signal analysis is the mainstream of gear fault diagnosis. However, the actual operation condition of mechanical equipment is generally harsh, the result of which is that the collected vibration signal contains a large amount of noise interference [3] and [4]. The vibration signals obtained under harsh working conditions generally contain strong noise interference, which conceals the weak fault feature produced by the gear fault and greatly affects the accuracy of the vibration signal. The difficulty of obtaining useful information from the collected vibration signals is increased under such operation conditions [5]. Therefore, the pre-processing of noise reduction is essential for the vibration signal in real working conditions.

The commonly used traditional noise reduction method includes low-pass, high-pass, and band-pass filters, but for the noise interference generated in real working conditions, no matter which filter is used, the integrity of the useful signal components will be affected [5]. With the development of signal-processing technology, more noise reduction methods have been proposed. Wavelet transform and singular value decomposition (SVD) are more commonly used in modern signal processing. Wavelet transform can decompose the original vibration signal into several signal components with different frequency bands and different resolutions [6]; the noise reduction is then processed for each signal components with different frequency bands. Generally, noise reduction methods based on wavelet transform include wavelet modulus maximum denoising, wavelet threshold denoising, wavelet correlation denoising and similar. However,

*Corr. Author's Address: College of Mechanical and Electrical Engineering, Hohai University, Changzhou, China, chenxh@hhu.edu.cn

wavelet threshold denoising needs to determine the threshold value, and an accurate threshold setting has a great influence on noise reduction effect. Wavelet correlation denoising uses the correlation of wavelet coefficients at corresponding points on different scales to distinguish the useful signal coefficients and noise coefficients to achieve the purpose of noise reduction. However, wavelet correlation denoising has the disadvantage of a complex algorithm, and its noise reduction effect is generally limited by the judging of correlation of wavelet coefficients. The noise reduction based on SVD can eliminate noise interference according to the different contribution of useful signal and noise interference to singular values, and that has been applied in the noise reduction of vibration signal [7].

However, the noise reduction methods based on SVD are faced with the problems of phase space matrix construction and denoising order selection. The noise interference generated in real working condition is more complex, which has the characteristics of irregularity, wide frequency distribution, and similar. In order to eliminate the strong noise interference in real work conditions, combining the advantages of the noise reduction ideas based on wavelet and SVD provides a new idea for the pre-processing of noise reduction of the gear vibration signal. The strong noise interference can be decomposed into a series of signal components with different frequency bands, and the corresponding denoising criteria based on SVD can be built to eliminate the noise interference in each frequency band according to its distribution characteristics.

Nevertheless, the general wavelet transform has some shortcomings, such as frequency leakage, frequency aliasing, translation sensitivity and less direction selection, and there are also some problems such as phase space matrix construction and denoising order selection in SVD [8]. With the development of the general wavelet transform, DTCWT has been proposed. Compared with the general wavelet transform, DTCWT has the characteristics of translation invariance, small frequency aliasing and multi-direction selection [9] and [10]. Meanwhile, the selections of embedding dimension, delay parameters and denoising order involved in the noise reduction based on SVD also need to be further studied [11].

In this paper, a noise reduction method based on DTCWT and cyclic singular energy difference spectrum is proposed. The gear vibration signal with strong noise interference is decomposed into a series of signal components by DTCWT, and the strong noise interference in each frequency band can be eliminated by cyclic singular energy difference spectrum. The noise reduction of the gear vibration signal can be realized by reconstructing the signal components of each frequency band after noise reduction. Finally, the validity of the proposed method is verified by experimental signal analysis.

However, it should be noted that most equipment is not equipped with the suitable vibration sensors for state monitoring and matching acquisition systems in existing large equipment, such as shearers, heading machines, shield machines, and so on. Therefore, it is impossible to realize the long-time continuous acquisition of vibration signal in the working process of equipment. Only the external vibration sensors and acquisition system can be used for short-term experiments. However, the gear fault in the real working condition usually occurs suddenly and has a certain probability, so it is very difficult to obtain the vibration signal of gear fault in the short-term acquisition process. Therefore, this paper uses the mechanical fault simulation bench to simulate the vibration signal of the gear fault. Meanwhile, the strong noise interference in real working condition is collected. Then, the strong noise interference after energy conversion is added into the vibration signal of the gear fault, which provides a way to obtain the gear fault vibration signal under strong noise interference in real working conditions.

1 MODEL BUILDING

1.1 Dual-Tree Complex Wavelet Transform

The basis function of DTCWT consists of two distinct real wavelets, and they constitute the Hilbert transform pair. The basis function of DTCWT is shown as [12] and [13]:

$$\varphi(t) = \varphi_h(t) + i\varphi_g(t), \tag{1}$$

where $\boldsymbol{\varphi}_h(t)$ and $\boldsymbol{\varphi}_g(t)$ are two real wavelets, and i is complex unit. $\boldsymbol{\varphi}_h(t)$ is the wavelet of real tree, and $\boldsymbol{\varphi}_g(t)$ is the wavelet of complex tree, and $\boldsymbol{\varphi}_h(t)$ and $\boldsymbol{\varphi}_g(t)$ are mutually Hilbert transform pairs.

The wavelet transform results in a real tree for signal $\mathbf{y}(t)$ are as follows:

$$\begin{cases} \mathbf{DI}_j^{\mathrm{Re}}(n) = 2^{j/2}\int_{-\infty}^{+\infty} \mathbf{y}(t)\varphi_g(2^j t - n)\,\mathrm{d}t & j = 1,2,\dots,J \\ \mathbf{CI}_J^{\mathrm{Re}}(n) = 2^{J/2}\int_{-\infty}^{+\infty} \mathbf{y}(t)\varphi_g(2^J t - n)\,\mathrm{d}t \end{cases}, \tag{2}$$

where $\mathbf{DI}_j^{\mathrm{Re}}(n)$ is the high-frequency coefficients in a real tree, $\mathbf{CI}_J^{\mathrm{Re}}(n)$ is the low-frequency coefficients in a real tree, and n is the number of data points. j is the decomposition scale coefficient, and J is the largest scale.

The wavelet transform results in a complex tree for signal $\mathbf{y}(t)$ are as follows:

$$\begin{cases} \mathbf{DI}_j^{\mathrm{Im}}(n) = 2^{j/2}\int_{-\infty}^{+\infty}\mathbf{y}(t)\varphi_h(2^j t-n)\,\mathrm{d}t \quad j=1,2,...,J \\ \mathbf{CI}_J^{\mathrm{Im}}(n) = 2^{J/2}\int_{-\infty}^{+\infty}\mathbf{y}(t)\varphi_h(2^J t-n)\,\mathrm{d}t \end{cases}, \quad (3)$$

where $\mathbf{DI}_j^{\mathrm{Im}}(n)$ is the high-frequency coefficients in a complex tree, $\mathbf{CI}_J^{\mathrm{Im}}(n)$ is the low-frequency coefficients in a complex tree.

The high-frequency coefficients and low-frequency coefficients obtained with DTCWT can be further expressed as follows:

$$\begin{cases} \mathbf{D}_j = \mathbf{DI}_j^{\mathrm{Re}}(n) + i\mathbf{DI}_j^{\mathrm{Im}}(n) \quad j=1,2,...,J \\ \mathbf{C}_J = \mathbf{CI}_J^{\mathrm{Re}}(n) + i\mathbf{CI}_J^{\mathrm{Re}}(n) \end{cases}, \quad (4)$$

where $\mathbf{D}_j$ is the high-frequency coefficients of DTCWT, and $\mathbf{C}_J$ is the low-frequency coefficients of DTCWT.

In the specific calculation process, the decomposition and reconstruction of DTCWT are implemented with a Mallet fast algorithm [14]. According to the Mallet fast decomposition algorithm, the transformation relationship of the decomposition coefficients between scale j and scale j+1 is as follows:

$$\begin{cases} \mathbf{CI}_{j+1}^{\mathrm{Re}}(k) = \sum_m \mathbf{h}_0(m-2k)\mathbf{CJ}_j^{\mathrm{Re}}(m) \\ \mathbf{DI}_{j+1}^{\mathrm{Re}}(k) = \sum_m \mathbf{h}_1(m-2k)\mathbf{DI}_j^{\mathrm{Re}}(m) \\ \mathbf{CI}_{j+1}^{\mathrm{Im}}(k) = \sum_m \mathbf{g}_0(p-2k)\mathbf{CJ}_j^{\mathrm{Im}}(p) \\ \mathbf{DI}_{j+1}^{\mathrm{Im}}(k) = \sum_m \mathbf{g}_1(p-2k)\mathbf{DI}_j^{\mathrm{Im}}(p) \\ \mathbf{CI}_j^{\mathrm{Re}}(k) = \sum_m \bar{\mathbf{h}}_0(k-2m)\mathbf{CI}_{j+1}^{\mathrm{Re}}(m) + \sum_m \bar{\mathbf{h}}_1(k-2m)\mathbf{DI}_{j+1}^{\mathrm{Re}}(m) \\ \mathbf{CI}_j^{\mathrm{Im}}(k) = \sum_m \bar{\mathbf{g}}_0(k-2p)\mathbf{CI}_{j+1}^{\mathrm{Im}}(p) + \sum_m \bar{\mathbf{g}}_1(k-2p)\mathbf{DI}_{j+1}^{\mathrm{Im}}(p) \end{cases}, \quad (5)$$

where $\mathbf{h}_0$ and $\mathbf{h}_1$ are the low-pass filter and high-pass filter of real tree wavelet, and $\mathbf{g}_0$ and $\mathbf{g}_1$ are the low-pass filter and high-pass filter of complex tree wavelet. m is the length of the filter of real tree wavelet, and p is the length of the filter of complex tree wavelet. k is the number of data points. $\bar{\mathbf{h}}_0$, $\bar{\mathbf{h}}_1$, $\bar{\mathbf{g}}_0$ and $\bar{\mathbf{g}}_1$ are the corresponding reconstruction filters, respectively. The decomposition and reconstruction process of DTCWT can be represented as Fig. 1 [15].

The original vibration signal containing strong noise interference is decomposed into a series of signal components with different frequency characteristics. Next, a cyclic singular energy difference spectrum is used to realize the pre-processing of noise interference in each frequency band.

1.2 Cyclic Singular Energy Difference Spectrum

1.2.1 Noise Reduction Principle Based on SVD

The noise reduction idea based on SVD is according to the singular value difference contributed by useful signal and noise interference [16]. Assuming that the vibration signal includes noise interference is $\mathbf{x} = (x_1, x_2, ..., x_N)$, where N is the number of data points. The phase space matrix of the vibration signal $\mathbf{x}$ can be constructed as follows:

$$\mathbf{A} = \begin{bmatrix} x_1 & x_2 & \cdots & x_m \\ x_{1+\tau} & x_{2+\tau} & \cdots & x_{m+\tau} \\ \vdots & \vdots & & \vdots \\ x_{1+(d-1)\tau} & x_{2+(d-1)\tau} & \cdots & x_{m+(d-1)\tau} \end{bmatrix}_{m\times d}, \quad (6)$$

where $m=N-(d-1)\tau$, and τ is the delay parameter, d is the number of matrix rows, that is embedding dimension.

The construction of phase space matrix is the foundation of the noise reduction based on SVD, and the one-dimensional time-domain vibration signal can be transformed into a phase space matrix with multiple-dimensions. In the phase space matrix, the data in the $(n+1)^{\mathrm{th}}$ row always lags behind the τ data points compared with the data in the n^{th} row, and τ is the delay parameter. For example, in Eq. (6), the data in the first row of phase space matrix $\mathbf{A}$ is $(x_1, x_1, ..., x_m)$, and the data in the second row of phase space matrix $\mathbf{A}$ is $(x_{1+\tau}, x_{2+\tau}, ..., x_{m+\tau})$. If the vibration signal is composed of the ideal signal without noise interference, the data between the adjacent two rows of phase space matrix will be highly correlated. That is an ill-conditioned matrix, and the singular values with large values for this matrix are thought to be contributed by a useful signal. If the signal is composed of noise interference, the data between the adjacent two rows have a small correlation, which is a well-conditioned full-rank matrix, and the singular value structure with uniform numerical distribution can be produced. Therefore, it can be considered that the larger singular value is contributed by both useful signal and noise interference, and the smaller singular value is contributed entirely by noise interference. The noise interference can be effectively eliminated by selecting and preserving singular values. For phase matrix $\mathbf{A}^{m\times d}$, according to the theory of SVD, there must be a pair of orthogonal matrices $\mathbf{U} \in \mathbf{R}^{m\times d}$ and

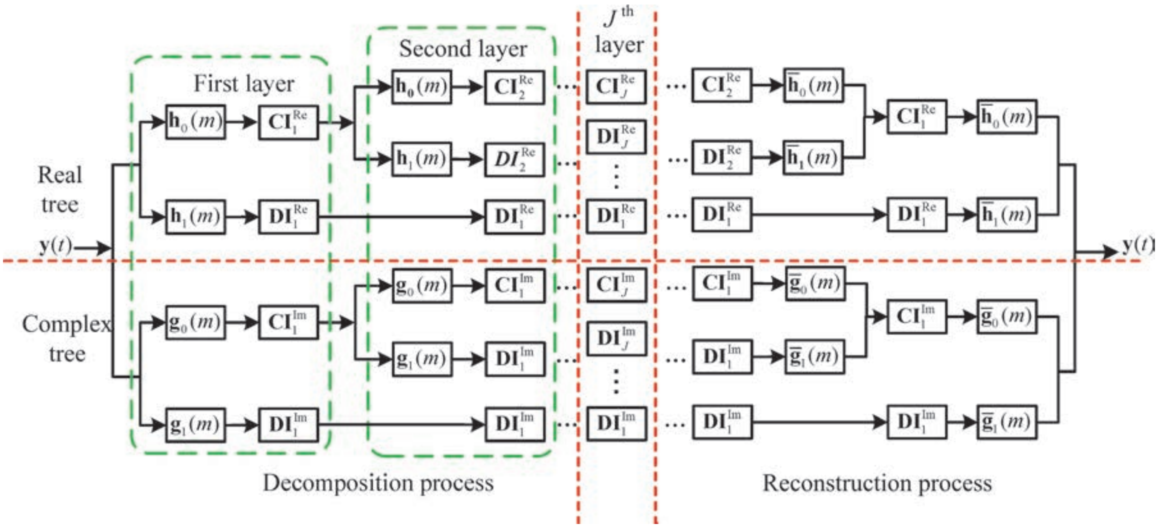

Fig. 1. *The decomposition and reconstruction processes of DTCWT*

$\mathbf{V} \in \mathbf{R}^{d\times d}$, which satisfy $\mathbf{U}^T\mathbf{U}=\mathbf{I}_d$ and $\mathbf{V}^T\mathbf{V}=\mathbf{V}\mathbf{V}^T=\mathbf{I}_d$ [17]. The phase matrix can be expressed as follows:

$$\mathbf{A}=\mathbf{U}\mathbf{S}\mathbf{V}^T, \tag{7}$$

where $\mathrm{S}=\{\lambda_1,\lambda_2,...,\lambda_h\}$, $\lambda_1\geq\lambda_2\geq...\geq\lambda_h\geq 0$ is a diagonal matrix with $(1+(d-1)\tau)\times m$ dimension, and they are the singular values of phase space matrix **A**. **U** is the left singular matrix of **A**, and **V** is the right singular matrix of **A**.

Next, the singular values contributed by the useful signal are retained, and that contributed by noise interference are set to zero. The singular value diagonal matrix is converted to $\tilde{\mathbf{S}}=(\lambda_1,\lambda_2,...,\lambda_k,0,...,0)$ $k\leq h=(1+(d-1)\tau)\times m$. The inverse process of SVD is performed according to Eq. (8) on the basis of the left singular matrix $\mathbf{U}\in\mathbf{R}^{m\times d}$ and right singular matrix $\mathbf{V}\in\mathbf{R}^{d\times d}$, and the phase space eliminated noise interference can be obtained. Further, the inverse process of constructing the phase space matrix is conducted, and the noise reduction can be realized.

$$\tilde{\mathbf{A}}=\mathbf{U}\tilde{\mathbf{S}}\mathbf{V}^T. \tag{8}$$

Through the analysis of the noise reduction theory of SVD, selecting the denoising order, that is, determining the number of the retained singular values is the key factor that affects the effect of noise reduction.

1.2.2 Cyclic Singular Energy Difference Spectrum

The key to eliminating noise interference is the selection of denoising order. However, at present, most noise reduction methods based on SVD are used to eliminate the noise interference one-time by selecting denoising order. However, the large singular value may be contributed by useful signal and noise interference, and the smaller mutation point of the maximum singular value may also contain the useful signal. So, the idea of one-time completion of noise reduction may lead to the noise interference being unable to be eliminated completely or useful signals being mistakenly eliminated. Therefore, the noise reduction method called cyclic singular energy difference spectrum is proposed based on the idea of a cascaded cycle and successive elimination of noise interference. In each cycle of the noise reduction process, only the definite noise interference is eliminated each time, and though the cycle process, the strong noise interference can be eliminated successively step by step. In the noise reduction process of using cyclic singular energy difference spectrum, each cyclic noise reduction process needs to select the delay parameter, embedding dimension and denoising order. The selection of relevant parameters of the proposed method is as follows:

(1) Selection of delay parameter

In this paper, the mutual information function method is used to determine the delay parameter, and the formula of mutual information function is as follows [18]:

$$\mathbf{I}(\tau)=\sum_{i=1}^{N-\tau}\mathbf{p}(x_i,x_{i+\tau})\ln\frac{\mathbf{p}(x_i,x_{i+\tau})}{\mathbf{p}(x_i)\,p(x_{i+\tau})}, \tag{9}$$

where $\mathbf{p}(x_i)$ is the probability of numerical occurrence of the i^{th} data point in a vibration signal, and $\mathbf{p}(x_{i+\tau})$

is the probability of numerical occurrence of the $(i+\tau)^{\text{th}}$ data point. $\mathbf{p}(x_i, x_{i+\tau})$ is the joint probability of $\mathbf{p}(x_i)$ and $\mathbf{p}(x_{i+\tau})$, and it represents the probability of the numerical occurrence of $x_{i+\tau}$ after the numerical occurrence of x_i. The selection of the delay parameter is defined according to the corresponding value of the first minimum to Eq. (9) [19].

(2) Selection of embedding dimension

In this paper, the embedding dimension of the phase space is selected by the follows [20]:

$$\mathbf{E}(d) = \frac{1}{N - d\tau} \sum_{i=1}^{N-d\tau} \frac{\left\| \mathbf{X}_i(d+1) - \mathbf{X}_{n(i,d)}(d+1) \right\|}{\left\| \mathbf{X}_i(d) - \mathbf{X}_{n(i,d)}(d) \right\|}, \quad (10)$$

where $\mathbf{X}_i(d)$ is the i^{th} reconstruction vector of the constructed phase space when the embedding dimension is d and delay parameter τ is determined, and $\mathbf{X}_{n(i,d)}(d)$ is the nearest neighbour of $\mathbf{X}_i(d)$. The nearest neighbour $\mathbf{X}_{n(i,d)}(d)$ is the reconstruction vector with the minimum Euclidean distance between the other reconstruction vectors of the constructed phase space and $\mathbf{X}_i(d)$. When the delay parameter τ is determined, the value of $\mathbf{E}(d)$ is only related to the embedding dimension d. To define $\mathbf{E}_1(d)=\mathbf{E}(d)/\mathbf{E}(d+1)$, it is generally believed that the value of d is the appropriate embedding dimension when $\mathbf{E}_1(d)$ changes slowly as the increasing of d [16].

(3) Selection of denoising order

In this paper, a new selection method of denoising order is proposed: singular energy difference spectrum. The singular energy difference spectrum is to calculate the energy difference between each singular value and its adjacent singular values. According to the characteristic that the singular values of noise interference and useful signal are quite different, the signal component mutation (useful signal and noise interference) occurs at the abrupt change of singular value, which is the inevitable result of the difference in correlation between useful signal and noise interference. Meanwhile, calculating the energy of singular values can amplify the difference between adjacent singular values, and the mutation between adjacent singular values can be increased. It is easier to detect the mutation point of singular values, and the determined mutation point can better represent the mutation of signal components at here. Furthermore, all extreme points of the singular energy difference spectrum and their corresponding sequence numbers can be obtained, and the average value of all extreme points can be calculated. The maximum singular value sequence number of the extreme point with greater than the average value can be taken as the denoising order, and the singular values smaller than the denoising order can be determined to be completely contributed by noise interference. The detailed calculation process is as follows:

SVD is performed on the phase space matrix [21], and the obtained singular value sequence is $\mathbf{S}=\{\lambda_1, \lambda_2, ..., \lambda_h\}$, and $\lambda_1 \geq \lambda_2 \geq ... \geq \lambda_h \geq 0$, and the energy of singular value can be expressed as follows:

$$\mathbf{E}_i = \lambda_i^2, \quad (11)$$

where $\mathbf{E}_i$ is the energy of the i^{th} singular value.

The difference spectrum of singular energy can be expressed as follows:

$$\mathbf{b}_i = \lambda_i^2 - \lambda_{i+1}^2, \; i = 1, 2, ..., h. \quad (12)$$

The average of the difference spectrum of the singular energy is calculated.

$$\bar{\mathbf{p}} = (\lambda_i^2 - \lambda_{i+1}^2) \Big/ \sum_{i=1}^{h} \lambda_i^2 . \quad (13)$$

The extreme value point b_i of singular energy difference spectrum represents the mutation of the signal components at the i^{th} singular value. The singular value sequence numbers of all extreme points that are is greater than the average value are found. The maximum singular value sequence number of the extreme point with greater than the average value $\bar{\mathbf{p}}$ is taken as the denoising order of one-time cycle. It can be found that the denoising order is a mutation point of singular value, which represents the signal component mutation. It is not the biggest mutation point, and it is obtained according to the average value. The singular values smaller than the denoising order can be determined to be essentially contributed by noise interference.

(4) Algorithm process

The proposed cyclic singular energy difference spectrum is introduced on the basis of selection methods of delay parameter, embedding dimension and denoising order.

Step 1: According to the characteristics of vibration signal under strong noise interference, the delay parameter and embedding dimension are selected by Eqs. (9) and (10), and the phase space matrix can be constructed;

Step 2: The singular energy difference spectrum can be obtained according to Eqs. (11) and (12), and the average value of those can be further obtained;

Step 3: The singular value sequence numbers whose abrupt extreme values are greater than their average value in singular energy difference spectrum are obtained, and the maximum sequence number is defined as the denoising order, and the singular values whose sequence number are greater than denoising order are replaced by zero;

Step 4 The inverse process of SVD is carried out, and the noise reduction signal can be reconstructed, and one-time noise reduction is completed, and there is still a part of noise interference that has not been eliminated.

Step 5 The signal after one-time noise reduction is regarded as a new signal, and it is treated as a new processed object to replace the original vibration signal. Then, the process of Steps 1 to 4 is cycled until the termination condition of noise reduction of cyclic singular energy difference spectrum is satisfied.

Step 6 In the proposed cyclic singular energy difference spectrum, the termination condition is that the maximum sequence number of the singular values whose abrupt extreme values detected in Step 3 are greater than the average value of those is less than a certain value. When the termination condition is satisfied, the noise reduction process will be terminated after this time noise reduction. The flowchart of the proposed cyclic singular energy difference spectrum is shown in Fig. 2.

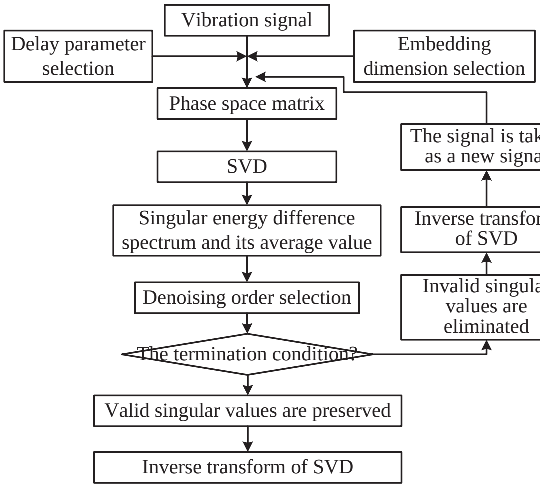

Fig. 2. *The flowchart of the proposed cyclic singular energy difference spectrum*

2 EXPERIMENTAL ANALYSIS

The overall analysis flowchart of the proposed method is shown in Fig. 3 and MATLAB software is used for the following analysis and processing of signals.

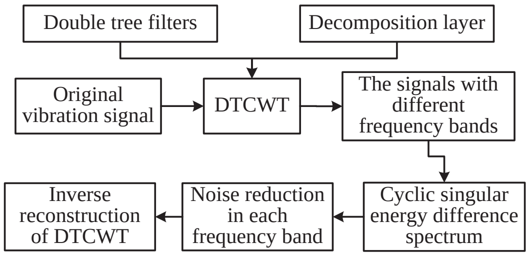

Fig. 3. *The flowchart of the proposed noise reduction method*

2.1 The Analysis of the Simulated Signal

Based on the characteristics of the vibration signal generated by gears, the simulated signal is shown as Eq. (4), and its time-domain signal and frequency spectrum are shown in Fig. 4

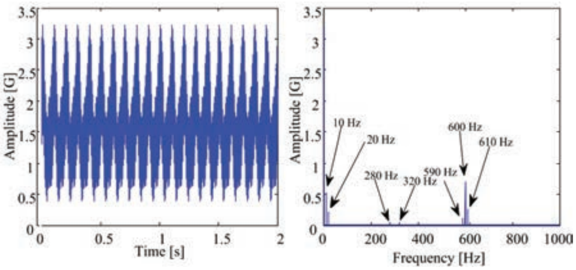

Fig. 4. *The simulated signal a) time-domain signal, and b) its frequency spectrum*

It can be seen from Fig. 4 that the simulated time-domain signal is more regular and have more obvious periodic components. The main frequency components are outstanding. The Gaussian white noise is used to simulate strong noise interference, and which are added into the simulated signal. The simulated signal added noise interference and its frequency spectrum are shown in Fig. 5

$$\begin{cases} \mathbf{y}_0(t) = (1+0.8+0.4\cos(20\pi t))\cdot\sin(0.1\sin(20\pi t)) \\ \mathbf{y}_1(t) = (1+0.6+0.5\cos(20\pi t)+0.1\cos(40\pi t)) \\ \qquad \cdot\cos(600\pi t+0.1\sin(20\pi t)) \\ \mathbf{y}_2(t) = 0.5(1+0.5+0.3\cos(20\pi t)) \\ \qquad \cdot\sin(1200\pi t+0.5\sin(20\pi t)+0.2\sin(40\pi t)) \\ \mathbf{y} = \mathbf{y}_0+\mathbf{y}_1+\mathbf{y}_2 \\ t = 0:0.0005:2 \end{cases}. \quad (4)$$

It can be seen from Fig. 5 that the simulated signal is completely submerged by the added noise interference. Except for the very prominent frequency points of 10 Hz and 600 Hz, the other frequency components are disturbed by the noise interference. The proposed noise reduction method is used to deal with the simulated signal added noise interference. Firstly, DTCWT is used, and the number of the decomposition layers is important for the subsequent noise reduction effect. If the number of decomposition layers is large (more than 8), the frequency band of some decomposed signal components will be too narrow, and it is easy to cause signal loss and signal distortion. If the number of decomposition layers is small (less than 4), it will cause the similar wavelet coefficients of useful signal and noise interference can not be separated, which cause the noise reduction effect of the subsequent process to be reduced. Therefore, through multiple experiments of the decomposition effect of DTCWT, the number of decomposition layer is determined to 6. The decomposition result of DTCWT is shown in Fig. 6.

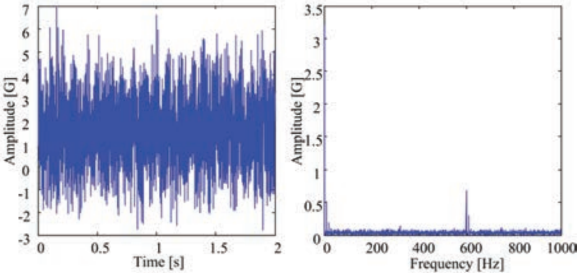

Fig. 5. *The simulated signal added noise interference and its frequency spectrum*

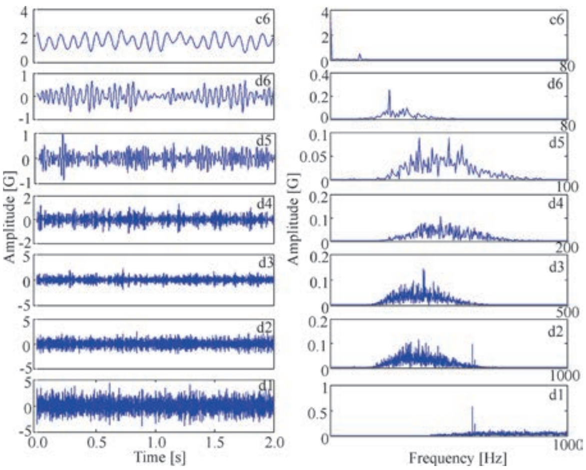

Fig. 6. *The decomposition result of DTCWT*

The simulated signal added noise interference is decomposed into seven signal components by DTCWT, and the corresponding noise interference is also decomposed into each signal component. For each signal component with different frequency bands, the cyclic singular energy difference spectrum is carried out. Meanwhile, the termination condition is that the denoising order determined by the last cyclic noise reduction is less than a certain value. In this way, the corresponding termination conditions can be set according to the noise distribution of each frequency band. Due to the space limitation, the noise reduction process in frequency band d1 is illustrated as an example, and the termination condition of this signal component is set as the denoising order being determined by the last cyclic process of noise reduction being less than 0. The noise reduction result of the signal component of frequency band d1 is shown in Fig. 7

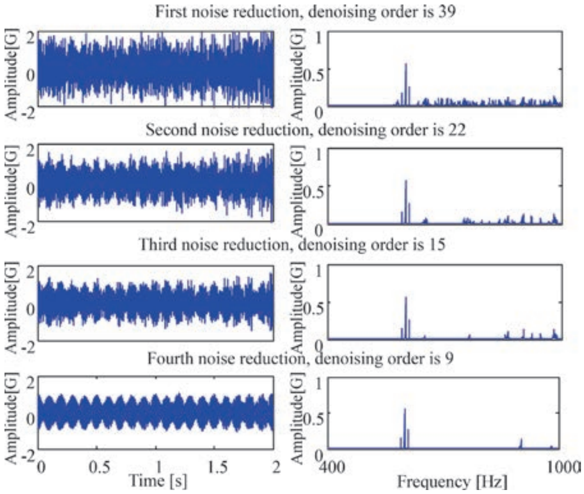

Fig. 7. *Cyclic noise reduction result of the signal component of frequency band d1*

As can be found in Fig. 7 for the signal component of frequency band d1, a total of four-cycle processes of noise reduction are used. With each cycle process of noise reduction, the noise interference is filtered out step by step, and the effective signal after noise reduction can be obtained. It can be found from the reduction result that the main frequency components in the frequency spectrum are 0 Hz, 60 Hz, 90 Hz, and 2 Hz, which are merely the frequency components of the simulated signal (Fig. 4). It is illustrated that the proposed method can eliminate noise interference better.

Furthermore, 9 0 Hz and 2 Hz are regarded as the useful signal and not filtered out in the final noise reduction. However, comparatively speaking, the proposed method can eliminate the most of noise interference, it has a good noise reduction effect. For other signal components obtained by DTCWT, noise reduction is carried out according to the cyclic singular energy difference spectrum, and the final noise reduction results of the simulated signal can be obtained, and they are shown in Fig. 8

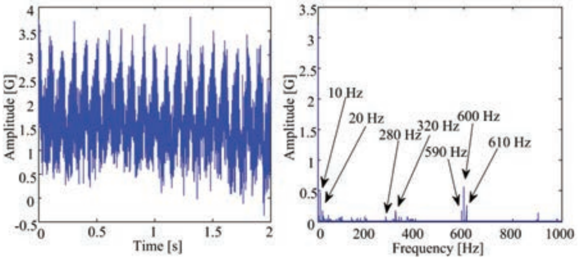

Fig. 8. *Final noise reduction result of the simulated signal*

It can be seen from Fig. 8 that the proposed method can effectively eliminate the strong noise interference comparing with Fig. 5. In the final noise reduction result, the main feature frequency components of the simulated signal are 10 Hz, 20 Hz, 280 Hz, 320 Hz, 590 Hz, 600 Hz, and 610 Hz, and they are completely retained, indicating that the above method can better eliminate noise interference and retain the useful signal. Comparing Figs. 4 and 8, it can be found that some frequency components are not filtered out; however, the amplitude of those frequency components are relatively low, and their interference with the useful signal is limited. Next, the validity of the proposed method is verified by the processing of the gear vibration signal under strong noise interference in real working condition.

2.2 Analysis of the Experiment Signal

The acquisition experiment of the strong noise interference in real working conditions is carried out in the gear system of rocker arm of electric haulage shearer. The vibration signals generated by the gear system are collected when it is running under no-load and normal cutting and the strong noise interference in real working condition can be extracted, and the acquisition experiment is shown in Fig. 9, and the strong noise interference in real working conditions is shown in Fig. 10.

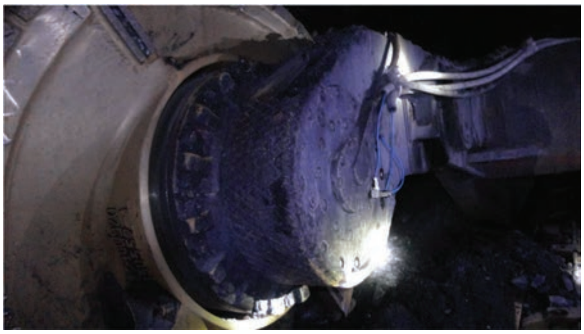

Fig. 9. *The acquisition experiment of strong noise interference*

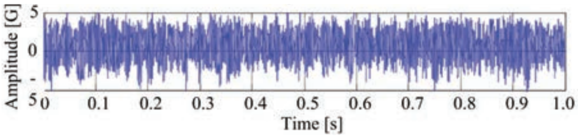

Fig. 10. *The strong noise interference in the real working conditions*

The SNR can be estimated after extracting strong noise interference in real working conditions, and its calculation process is shown in Eq. (15).

$$EPR = 10\lg(SE/NE) = 10\lg\left(\sum_{i=1}^{I} s_i^2 \Big/ \sum_{i=1}^{I} n_i^2\right), \qquad (15)$$

where *EPR* is the SNR in real working condition, *SE* the energy of useful signal, *NE* the energy of strong noise interference, and *I* the number of data points.

The gear fault vibration signal in strong noise interference is obtained by adding strong noise interference after energy conversion into the vibration signal collected from the mechanical fault simulation bench. In this paper, the mechanical fault simulation bench is composed of motor, planetary gearbox, spur gearbox, load system and vibration sensors, and vibration sensors are arranged on the housing of a planetary gearbox. In the experimental process, the broken tooth fault of sun gear in the planetary gearbox is simulated, and the broken tooth fault is processed by wire-cutting technology. The length of the broken tooth is 7 mm, and the broken gear is installed in the planetary gearbox. The motor speed is set to 40 Hz, and the load is set to 35 Nm by control software. The acquisition system works in synchronous sampling mode, and the sampling frequency is set to 2000 Hz. The collected experiment with the mechanical fault simulation bench is shown in Fig. 11, and the collected gear fault vibration signal is shown in Fig. 12.

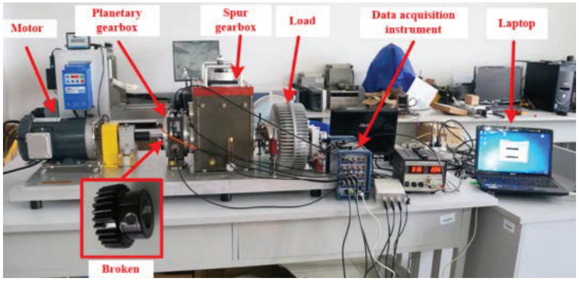

Fig. 11. *The collected experiment and gear state*

According to the SNR in real working conditions, the energy conversion coefficient can be confirmed. The noise interference in real working conditions converted by energy conversion coefficient is added into the gear fault vibration signal collected from the mechanical fault simulation bench. The gear fault vibration signal under strong noise interference is shown in Fig. 13, from which it can be seen that the gear fault vibration signal is all submerged after adding the strong noise interference in real working conditions, and its frequency spectrum is shown in Fig. 14.

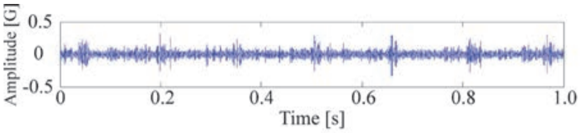

Fig. 12. *Vibration signal of broken gear fault collected from mechanical fault simulation bench*

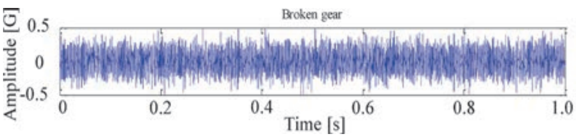

Fig. 13. *The gear fault vibration signal under strong noise interference in real working condition*

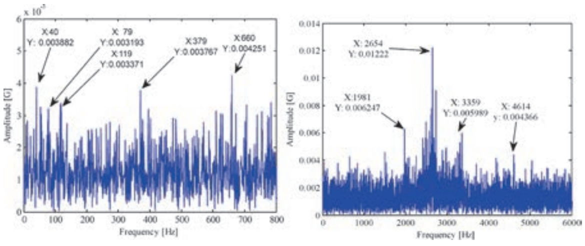

a) b)

Fig. 14. *The frequency spectrum of gear fault vibration signal in strong noise interference; a) detail frequency spectrum, and b) full frequency spectrum*

It can be seen from Fig. 14 that the prominent frequency points in the detail frequency spectrum are 40 Hz, 79 Hz, and 119 Hz, which are the output frequency of the motor and its double frequency and triple frequency, respectively. However, there are also high amplitude frequency components around these frequencies, which cause interference to these feature frequencies. Furthermore, 660 Hz corresponds approximately to the meshing frequency of the gear system, which is the installation part of the fault gear, and 1981 Hz, 2654 Hz, 3359 Hz and 4614 Hz correspond to the triple frequency, fourfold frequency, fivefold frequency, and sevenfold frequency, respectively. Although some frequency points are prominent in the frequency spectrum but the gear fault vibration signal suffers from strong noise interference in the low-, middle-, and high-frequency bands. Next, the gear fault vibration signal is decomposed by DTCWT, and the decomposition layer is set to 6. In the decomposition process of DTCWT, the applied filters are as follows: The high-pass filter $\mathbf{h}_1$ of real tree is [−0.0045, 0.0043, 0.0072, −0.0282, −0.0167, −0.0186, 0.86, −0.45, 0.2729, 0.1170, −0.087, −0.046, −0.0083, −0.0035], the low-pass filter $\mathbf{h}_0$ of real tree is [0.0035, −0.0083, 0.046, −0.087, −0.117, 0.2729, 0.45, 0.86, 0.0186, −0.0167, 0.0282, 0.0072, −0.0043, −0.0045]. The high-pass filter $\mathbf{g}_1$ of complex tree is [−0.0035, −0.0083, −0.046, −0.087, 0.1170, 0.2729, −0.45, 0.68, −0.0186, −0.0167, −0.0282, 0.0072, 0.0043, −0.0045], and the low-pass filter $\mathbf{g}_0$ of complex tree is [−0.0045, −0.0043, 0.0072, 0.0282, −0.107, 0.0186, 0.86, 0.45, 0.2729, −0.1170, −0.087, 0.046, −0.0083, 0.0035]. The decomposition result of DTCWT is shown in Fig. 15.

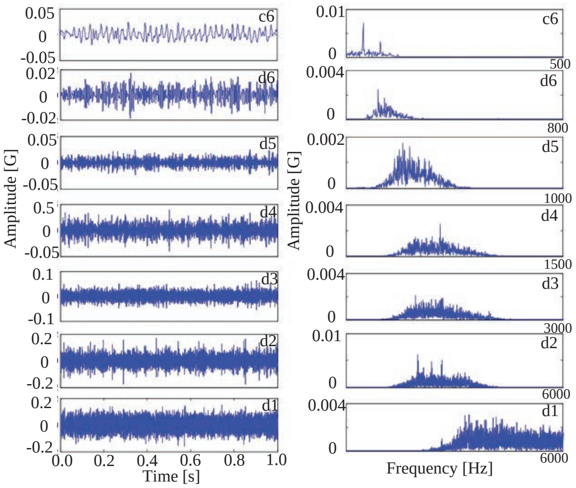

Fig. 15. *The decomposition result of DTCWT*

With DTCWT, seven signal components with different frequency bands and different resolution attributes are obtained. Meanwhile, the strong noise interference is also decomposed into different band signals according to their attributes. For the obtained signal components with different frequency bands, the noise reduction based on cyclic singular energy difference spectrum is carried out. Because the termination condition of the proposed noise reduction method is that the denoising order determined by the last cyclic is less than a certain value, different cycle termination conditions can be set for different band signals. In this paper, by comparing several experiments, the termination condition of noise reduction of frequency band c6 to d1 is that the denoising order determined by the last cycle is less than [30, 50, 50, 80, 100, 100, 120] , respectively. Due space limitations, the noise reduction process of frequency band d2 layer is illustrated as an example. The noise reduction process is shown in Fig. 16.

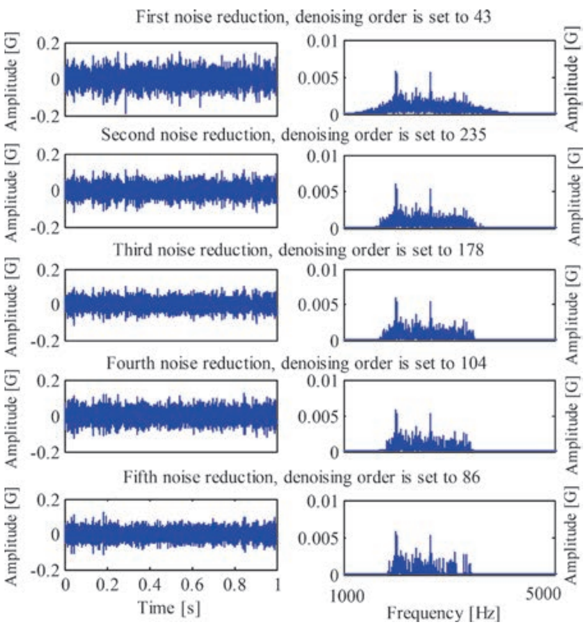

Fig. 16. *Noise reduction process of frequency band d2*

It can be seen from Fig. 16 that the noise reduction process of frequency band d2 is completed after 5 cycles of noise reduction. Compared to the signal of frequency band d2 layer between Figs. 15 and 16, the signal of frequency band d2 layer in Fig. 15 contains more noise interference, and the noise interference submerges most of the original signal frequency components. Based on the idea of the cascaded cycle and successive elimination of noise interference, the proposed cyclic singular energy difference spectrum is used, and the signal components determined to be noise interference are filtered out step by step in the process of each cycle noise reduction. It can also be seen from Fig.16 that the noise interference can be eliminated step by step with the increasing of the cycle number of noise reduction; then, the strong noise interference in frequency band d2 layer can be eliminated, and the useful signal can be retained.

To analyse the effect of different delay parameters on the noise reduction result, and the mutual information function method is proved to be effective in selecting the delay parameter, some qualitative and quantitative analyses are carried out. Similarly, the vibration signal of frequency band d2 is taken as the analysis object, and the delay parameters are set as 2, 4, 6, 8, 10 and 12, respectively, where the delay parameter is equal to 6, which is selected by the mutual information function method in this paper. In addition, for different delay parameters, the same methods are used to select the embedding dimension and denoising order. For the vibration signal of frequency band d2, the noise reduction results using different delay parameters are shown in Fig. 17.

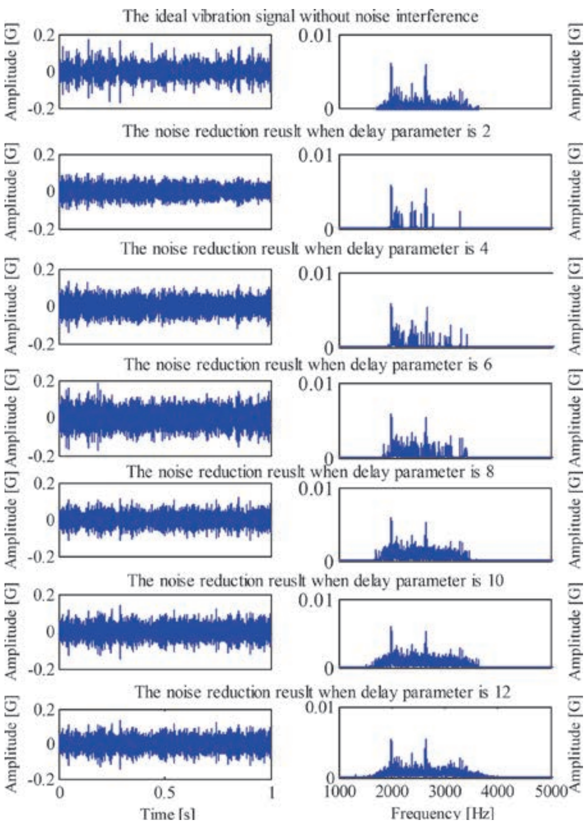

Fig. 17. *The noise reduction results using different delay parameters*

In the analysis process, except for different delay parameters, the other processing methods are all consistent. As can be seen from Fig. 17, with the increase of the value of the delay parameter, more signal components are retained. Compared with the ideal vibration signal without noise interference, when the delay parameter is selected 2 or 4, although their noise reduction results retain the main signal components, some useful signals are eliminated as noise interference. When the delay parameter is selected as 10 or 12, it can be found that there is too much noise interference at both ends of the signal frequency band, and the noise interference can not be effectively eliminated. By comparison, when the delay parameter is selected 6 or 8, they have a better noise reduction effect. In addition, the noise interference

Table 1. *Some feature indexes of the noise reduction results of different delay parameters and the ideal vibrations signal without noise interference*

Delay parameter	2	4	6	8	10	12	Vibration signal without noise interference
Energy	3.30	4.96	9.04	11.01	13.83	14.27	9.22
Average value ($\times 10^{-6}$)	1.18	9.87	4.20	9.7	4.2	3.45	6.87
Root mean square	1.82	2.23	3.01	3.32	3.72	3.93	3.04
Kurtosis	5.11	3.23	3.45	3.55	3.76	3.84	5.23
Waveform factor	143.3	144.1	145.3	146.1	146.6	147.1	146.28
Kurtosis factor ($\times 10^{-3}$)	1.4	2.7	7.2	10	14.9	16.4	8.3

results of different delay parameters are quantitatively analysed. Some feature indexes of the noise reduction results of different delay parameters and the ideal vibrations signal without noise interference are calculated, and they are shown in Table 1.

It can be seen from Table 1 that the quantization indexes of noise reduction results are the closest to the vibration signal without noise interference when the delay parameter is 6 or 8. Because of the better symmetry of the vibration signal, the magnitude of average values is smaller. When the delay parameter is 2, only the most prominent signal components are retained, and their kurtosis indexes are the largest. When the delay parameter is selected as other values, some abrupt signal components are eliminated by mistake, so the kurtosis index is relatively small, which is also the key issue to be studied in the future. When the delay parameter is set to 12, it can be found that the energy of the noise reduction signal is higher approximately by 54 % from the vibration signal without noise interference, because when the delay parameter is 12 or another large value, the data in the $(n+1)^{th}$ row always lags behind more data points compared with the data in the n^{th} row. This phenomenon causes the dimension of the phase space to decrease, and the size and number of extreme points of the singular energy difference spectrum is also reduced. However, the termination condition in the proposed method is that the maximum sequence number of the singular values whose abrupt extreme values are greater than the average value of those is less than a certain value, so the cycle noise reduction process stops prematurely when the delay parameter is large, and some noise interference is not eliminated. Then, when the delay parameter is 12, the noise reduction signal still contains some noise interference, so the energy of the noise reduction signal is significantly higher than that of the vibration signal without noise interference. In this paper, the delay parameter selected by the mutual information function method is 6, which also proves that it is feasible to apply mutual information function method for delay parameter selection.

For other frequency band signals obtained by DTCWT, the noise reduction is carried out according to the above process, and the signals after noise reduction of each frequency band are inversely reconstructed to obtain the final noise reduction result. The final noise reduction results of the gear fault vibration signal and its frequency spectrum are shown in Fig. 18. Fig. 19 is the comparison of the detailed spectrums of the vibration signal without noise interference and the vibration signal with noise interference after noise reduction. Meanwhile, the effectiveness of the proposed method is proved by combining the comparison analysis of the above Fig. 14, which is the frequency spectrums of the vibration signal in strong noise interference.

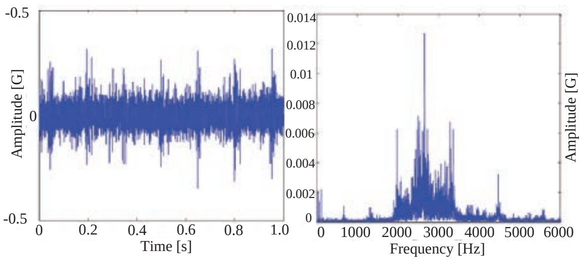

a) b)

Fig. 18. *Final noise reduction result of gear fault vibration signal and its frequency spectrum; a) gear fault vibration signal after noise reduction, and b) frequency spectrum after noise reduction*

To compare and analyse the above results comprehensively, it can be found that gear fault vibration signal is disturbed by strong noise interference seriously, main features of gear fault vibration signal are completely submerged by strong noise interference, and the low-, middle-, and high-frequency bands are full of noise interference (Fig. 14). After the processing of the proposed method, the gear fault vibration signal after noise reduction shows the regularity similar to the gear fault vibration signal without noise interference, and the noise interference in low-, middle-, and high-frequency bands are greatly reduced (comparison between Figs. 14 and 18). That is because DTCWT is used for signal decomposition, and each signal component obtained by DTCWT is denoised separately. Meanwhile, to compare the detailed spectrums between the vibration signal without noise interference and the vibration signal with noise interference after noise reduction (Fig. 19), it can be found that they have the same main frequency components, and the main composition of signal components is also similar. Most noise interference can be eliminated, main signal features can be represented, and the useful signal components can be obtained. However, it also can be found that the proposed noise reduction method does not completely eliminate the strong noise interference in real working condition, and there is still a small amount of noise interference. However, relatively speaking, any noise reduction method can not eliminate all noise interference. Compared with the strong noise interference in real working conditions, the proposed noise reduction method has a relatively effective noise reduction effect.

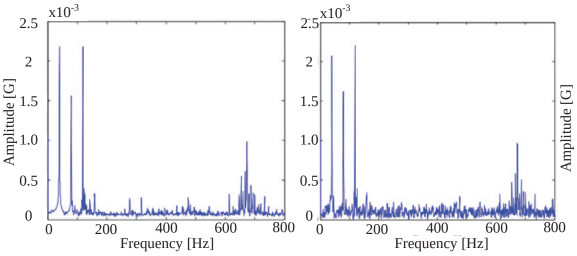

a) b)

Fig. 19. *The comparison of detailed spectrums; a) the detailed spectrum without noise interference, b) the detailed spectrum with noise interference after noise reduction*

In order to further illustrate the effectiveness of the proposed method, the proposed method is compared with the existing technologies, and the Butterworth low-pass filter and one-time noise reduction method based on SVD are used to process the same vibration signal under strong noise interference, respectively. When the Butterworth low-pass filter is applied, the cut-off frequencies are set as [80 Hz, 200 Hz, 300 Hz, 700 Hz, 1000 Hz, 3000 Hz, 5000 Hz] for the signal components of frequency band c6–d1 obtained by DTCWT after many experiments, and the final noise reduction result processed by Butterworth low-pass filter is shown in Fig. 20. When the one-time noise reduction method based on SVD is applied, the denoising order orders are set as [3, 5, 5, 8, 10, 10, 20] for the signal components of frequency band c6–d1 obtained by DTCWT, which is consistent with the proposed method in this paper. The final noise reduction result processed by one-time noise reduction method based on SVD is shown in Fig. 21.

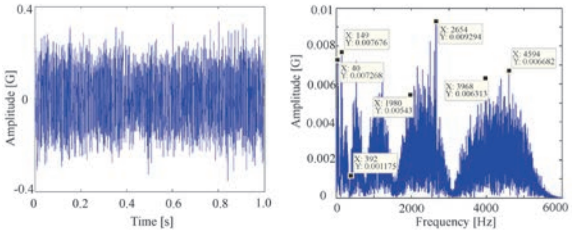

a) b)

Fig. 20. *Final noise reduction result processed by Butterworth low-pass filter; a) time-domain signal after noise reduction, and b) frequency spectrum after noise reduction*

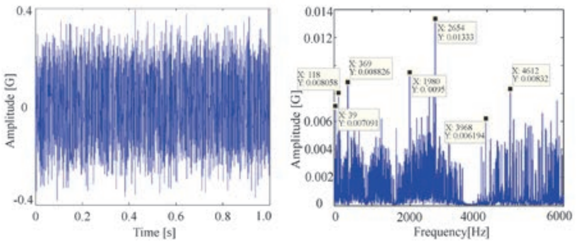

a) b)

Fig. 21. *Final noise reduction result processed by one-time noise reduction method based on SVD; a) time-domain signal after noise reduction, and b) frequency spectrum after noise reduction*

It can be seen from Fig. 20 that the time-domain signal processed by the Butterworth low-pass filter has no characteristic to follow. From the frequency spectrum, there is still more noise interference in the low-, middle-, and high-frequency bands. Among the frequency salient points marked in Fig. 20, some of them are the feature information contained in the original signal, but most of them are not included in the original signal. The noise reduction effect processed by Butterworth low-pass filter is worse than that of the proposed method. The main reason is that the low-pass filter eliminates all signal components lower than the cut-off frequency, and retains all signal components higher than the cut-off frequency. The strong noise interference in real working conditions exists in all frequency bands, so it is inevitable that the noise interference in some frequency bands cannot be eliminated.

Furthermore, it is very difficult to set the cut-off frequency reasonably when dealing with the actual noise interference. It can be seen from Fig. 21 that the time-domain signal processed by one-time noise reduction method based on SVD does not reflect the regular shock waveform similar to that in Fig. 18. In the frequency spectrum of Fig. 21, the main features of the vibration signal (marked in Fig. 21) are retained, but their clarity is far less than that in Fig. 18, there are still more noise interferences in the low-, middle-, and high-frequency bands of the whole frequency spectrum, which will interfere with these main feature information points.

Moreover, it also can be found that the signal components in the frequency band from 3000 Hz to 4000 Hz are eliminated as noise interference, and the main features from 3000 Hz to 4000 Hz are also mistaken as noise interference, which is a bad result. It can be seen that the noise reduction result processed by one-time noise reduction method based on SVD is far worse than that processed by the proposed method. The above comparison and analysis can also show that the proposed method has better noise reduction effect.

In this paper, the proposed method can be used to eliminate the strong noise interference of the vibration signal of equipment. It is a pre-processing for gear fault diagnosis process, which ensured that the further feature extraction and fault recognition can be conducted effectively and smoothly. Also, the proposed noise reduction method can also be applied to the detection of gear quality for production process. The authors of the present paper assert that the proposed method can be successfully applied to gear production process through two ways: The first way is that the proposed noise reduction method is applied to the condition monitoring of gear cutting machine. The vibration signal of the gear cutting machine can be obtained, and the proposed method can eliminate the noise interference contained in the vibration signal. The feature information that can reflect the operating state of the gear-cutting machine can be retained, and the operating state of the gear-cutting machine can be evaluated. The cutting quality of gear production process can be further guaranteed.

Another way is that the proposed noise reduction method is applied to the gear quality test after the gear is machined. A special test bench for testing the quality of gears can be built, and the machined gears can be run on the test bench. The vibration signal of the test bench can be obtained, and the proposed noise reduction method can be used to process the vibration signal, the useful signals which can be reflected in the gear quality being obtained by using the proposed method to eliminate the external interference. Further combined with other signal-processing technologies, the gear machining defects, such as excessive radial runout, tooth surface defects, tooth profile asymmetry and tooth profile periodic error, can be detected. Through the above two ways, the noise reduction method proposed in this paper can be applied to the gear production process to ensure the quality of the gear.

3 CONCLUSIONS

A pre-treatment noise reduction method based on DTCWT and cyclic singular energy difference spectrum is proposed in this paper. DTCWT can be used to decompose the gear fault vibration signal under strong noise interference, and the noise interference with different frequency attributes can be decomposed into different signal components. Based on the noise reduction principle of SVD, cyclic singular energy difference spectrum is proposed. According to the characteristics of each signal components obtained by DTCWT, the noise interference can be purposefully eliminated successively.

Furthermore, the termination condition of cyclic singular energy difference spectrum can be set according to the noise interference distribution characteristics in different frequency bands, and it has a better noise reduction effect than the one-time noise reduction idea. The final noise reduction of gear fault vibration signal under noise interference can be realized on the basis of reducing noise for all signal components obtained by DTCWT. The experiment results show that the proposed method can effectively eliminate the strong noise interference in real working condition, and the useful vibration signal components can be retained.

4 ACKNOWLEDGEMENTS

This research was funded by National Natural Science Foundation of China ([illegible]), Changzhou Sci & Tech Program (CJ20[illegible]5), the Fundamental Research Funds for the Central Universities (B200202226), and the Special project of science and technology innovation of Tiandi Science & Technology (2018 TD-MS03), and is gratefully acknowledged.

5 REFERENCES

[1] Pang, X.Y., Cheng, B.A., Yang, Z.J. (2019). A fault feature extraction method for a gearbox with a composite gear train based on EEMD and translation-invariant multiwavelet neighbouring coefficients. *Strojniski vestnik – Journal of*

Mechanical Engineering, vol. 65, no. 1, p. 3-11, **DOI:10.5545/sv-jme.2018.5441**.

[2] Mohammad, R.A.A.A., Ashkan, M., Meghdad, K. (2016). Wavelet transform and least square support vector machine for mechanical fault detection of an alternator using vibration signal. *Journal of Low Frequency Noise Vibration and Active Control*, vol. 35, no. 1, p. 52-63, **DOI:10.1177/0263092316628258**.

[3] Klausen, A., Khang, H.V., Robbersmyr, K.G. (2020). Multi-band identification for enhancing bearing fault detection in variable speed conditions. *Mechanical Systems and Signal Processing*, vol. 139, art. ID:106422, **DOI:10.1016/j.ymssp.2019.106422**.

[4] Brigham, K., Zappal, D., Crabtree, C.J., Donaghy, S.C. (2020). Simplified automatic fault detection in wind turbine induction generators. *Wind Energy*, vol. 23, no. 4, p. 1135-1144, **DOI:10.1002/we.2478**.

[5] Tsiaparas, N.N., Golemati, S., Andreadis, I., Stoitsis, J., Valavanis. I., Nikita, K.S. (2013). Assessment of carotid atherosclerosis from B-mode ultrasound images using directional multi-scale texture features. *Measurement Science and Technology*, vol. 23, 114004, **DOI:10.1088/0957-0233/23/11/114004**.

[6] Mamun, Md., Al-Kadi, M., Marufuzzamann, M. (2013). Effectiveness of wavelet denoising on electroencephalogram signals. *Journal of Applied Research and Technology*, vol. 11, no. 1, p. 156-160, **DOI:10.1016/S1665-6423(13)71524-4**.

[7] Zhao, M., Jia, X. (2017). A novel strategy for signal denoising using reweighted SVD and its applications to weak fault feature enhancement of rotating machinery. *Mechanical Systems and Signal Processing*, vol. 94, p. 129-147, **DOI:10.1016/j.ymssp.2017.02.036**.

[8] Jiang, H.M., Chen, J., Dong, G.M. (2015). Study on hankel matrix-based SVD and its application in rolling element bearing fault diagnosis. *Mechanical Systems and Signal Processing*, vol. 52, p. 338-359, **DOI:10.1016/j.ymssp.2014.07.019**.

[9] Tomassi, D., Milone, D., Nelson, J.D.B. (2015). Wavelet shrinkage using adaptive structured sparsity constraints. *Signal Processing*, vol. 106, p. 73-87, **DOI:10.1016/j.sigpro.2014.07.001**.

[10] Dudik, J.M., Coyle, J.L., El-Jaroudi, A., Sun, M., Sejdić, E. (2016). A matched dual-tree wavelet denoising for tri-axial swallowing vibrations. *Biomedical Signal Processing and Control*, vol. 27, p. 112-121, **DOI:10.1016/j.bspc.2016.01.012**.

[11] Yu, X., Liang, W., Zhang, L., Jin, H., Qiu, J. (2016). Dual-tree complex wavelet transform and SVD based acoustic noise reduction and its application in leak detection for natural gas pipeline. *Mechanical Systems and Signal Processing*, vol. 72-73, p. 266-285, **DOI:10.1016/j.ymssp.2015.10.034**.

[12] Yin, M., Liu, W., Zhao, X. (2013). Image denoising using trivariate prior model in nonsubsampled dual-tree complex contourlet transform domain and non-local means filter in spatial domain. *Optik*, vol. 124, no. 24, p. 6896-6904, **DOI:10.1016/j.ijleo.2013.05.132**.

[13] Chen, X.H., Cheng, G., Li, Y. (2018). Fault diagnosis of planetary gear based on entropy feature fusion of DTCWT and OKFDA. *Journal of Vibration and Control*, vol. 24, no. 21, p. 5044-5061, **DOI:10.1177/1077546317742506**.

[14] Xu, Y., Meng, Z., Lu, M. (2014). Gear fault diagnosis based on dual-tree complex wavelet transform and singular value difference spectrum. *Journal of Vibration and Shock*, vol. 33, no. 1, p. 11-16.

[15] Kingsbury, N.G. (1998). The dual-tree complex wavelet transform: a new technology for shift invariance and directional filters. *IEEE Digital Signal Processing Workshop*, vol. 98, no. 1, p. 2-5.

[16] Traore, O.L., Pantera, L., Favretto-Cristini, N., Cristinni, P., Viguier-Pla, S., Vieu, P. (2017) Structure analysis and denoising using singular spectrum analysis: Application to acoustic emission signals from nuclear safety experiments. *Measurement*, vol. 104, p. 78-88, **DOI:10.1016/j.measurement. 2017.02.019**.

[17] De, M.B. (1993). The singular value decomposition and long and short spaces of noisy matrices. *IEEE Transactions on Signal Processing*, vol. 41, no. 9, p. 2826-2838, **DOI:10.1109/78.236505**.

[18] Zeng, M., Yang, Y., Zheng, J., Cheng, J. (2015). μ-SVD based denoising method and its application to gear fault diagnosis. *Chinese Journal of Mechanical Engineering*, vol. 51, no. 3, p. 95-103, **DOI:10.3901/JME.2015.03.095**. (in Chinese)

[19] Wang, B., Ren, Z., Wen, B. (2012). Fault diagnosis method of rotating machines based on nonlinear multi-parameters. *Chinese Journal of Mechanical Engineering*, vol. 48, no. 5, p. 63-69, **DOI:10.3901/JME.2012.05.063**.

[20] Cao, L.Y. (1997). Practical method for determining the minimum embedding dimension of a scalar time series. *Physica D: Nonlinear Phenomena*, vol. 110, no. 1-2, p. 43-50, **DOI:10.1016/s0167-2789(97)00118-8**.

[21] Cong, F.Y., Chen, J., Dong, G.M., Zhao, F. (2013). Short-time matrix series based singular value decomposition for rolling bearing fault diagnosis. *Mechanical Systems and Signal Processing*, vol. 34, no. 1-2, p. 218-230, **DOI:10.1016/j.ymssp.2012.06.005**.

Vsebina

Strojniški vestnik - Journal of Mechanical Engineering
letnik 66, (2020), številka 10
Ljubljana, oktober 2020
ISSN 0039-2480

Izhaja mesečno

Razširjeni povzetki (extended abstracts)

Strojniški vestnik - Journal of Mechanical Engineering 66(2020)10, SI 71

Prejeto v recenzijo: 2020-07-09
Prejeto popravljeno: 2020-08-21
Odobreno za objavo: 2020-09-24

Eksperimentalno spremljanje utrujenostnih lastnosti vibrirajočih mehanskih sistemov

Filippo Cianetti
Univerza v Perugii, Italija

Opazovanje in vrednotenje utrujenostnih poškodb in v splošnem utrujenostnih lastnosti mehanskih sistemov (v vozilih, letalih, plovilih, vetrnih turbinah ipd.) med življenjsko dobo ni preprosta naloga. Za to obstajajo različne teoretične in numerične metode v časovni ali frekvenčni domeni na osnovi privzetih obremenitvenih pogojev (tj. sil in pospeškov). Do izhodnih napetostnih stanj pridejo z numeričnimi modeli mehanskega sistema (npr. sistem več teles – MBS, končni elementi – MKE, sistem več teles z gibkimi elementi – Flex/MBS) ali z neposrednimi meritvami napetostnih/deformacijskih stanj na osnovi hipotez o trajni dinamični trdnosti (tj. Wöhlerjeve krivulje ali Basquinove krivulje S-N).

V literaturi je opisanih več inštrumentov oz. merilnih verig za vrednotenje v časovni domeni (snemalnik rainflow) ali v frekvenčni domeni, pri nobeni od metod pa ni zagotovljeno celovito opazovanje dinamičnega vedenja sistema (tj. pospeškov, notranjih obremenitev, deformacij) in napovedovanje dejanskih poškodb za ocenjevanje preostale življenjske dobe sistema.

V članku je predstavljena preprosta metoda v časovni domeni za spremljanje trenutnih utrujenostnih lastnosti z opredelitvijo trenutnih in kumulativnih potencialnih poškodb oz. amplitude ekvivalentnega poškodbenega signala na osnovi metode štetja Rainflow (RFC), zakona linearne akumulacije poškodb (Palmgren-Minerjevo pravilo) in signalov, ki izhajajo iz dinamike sistema. Metoda precenjuje realne poškodbe, da je upravitelj sistema opozorjen še pred nastankom razpok, poleg tega pa jo je mogoče preprosto pretvoriti v elektronsko vezje, ki se pritrdi na mehanski sistem in poveže z enim od običajnih senzorjev za nadzor funkcionalnosti sistema. V članku je predstavljena realizacija metode v računalniškem okolju za dinamično večdomensko simulacijo mehanskih sistemov ter projektiranje in verifikacijo regulacijskih sistemov. Na ta način je bilo mogoče preveriti uporabnost analitičnega orodja s fizikalnimi meritvami na sami turbini in z numeričnimi analizami na osnovi bolj ali manj kompleksnih dinamičnih modelov generatorja.

Osnovna hipoteza tega dela je, da obstajajo različni parametri, ki se že merijo na strojih zaradi različnih razlogov (npr. hitrost, pospeški, momenti) in katerih vrednosti je mogoče takoj uporabiti za nadzor stanja, ne glede na ocene v zvezi s trajnostjo, utrujenostjo ali poškodbami sistema.

Na osnovi domneve o linearnem vedenju stroja in mehanskega sistema je vedno mogoče določiti odvisnosti med merjenimi parametri in splošnim napetostnim stanjem v poljubni komponenti in tako vrednotiti utrujanje na osnovi teh generičnih signalov s klasičnimi orodji za analizo časovne zgodovine napetostnih stanj. Če se vrednotenje utrujenostnih lastnosti izvaja na generičnem signalu, ki ne omogoča neposredne uporabe vseh hipotez in orodij, ki so bila razvita za vrednotenje poškodb iz napetostnih stanj, je upravičena opredelitev potencialnih utrujenostnih poškodb in s tem predlagane metode.

Znanstvena in tehnična skupnost na področju avtomatskega vodenja bo tako lahko vključila utrujanje med tiste procese v poljubnem mehanskem sistemu (vozila, letala, vlaki, ladje, vetrne turbine), ki jih je mogoče upravljati s povratno zanko ter upoštevati njegove minimalne ali maksimalne vrednosti in potencial za poškodbe.

Ključne besede: utrujanje, poškodbe, vibracije, metoda štetja rainflow, naključne obremenitve, regulacijski sistemi

*Naslov avtorja za dopisovanje: Univerza v Perugii Italija, filippo.cianetti@unipg.it

Strojniški vestnik - Journal of Mechanical Engineering 66(2020)10, SI 72

Prejeto v recenzijo: 2020-05-12
Prejeto popravljeno: 2020-08-19
Odobreno za objavo: 2020-09-03

Numerična analiza napetosti za različne širine varkov pri navarjanju

Adam Kulawik – Joanna Wrƃe l
Tehniška univerza v Čenstohovi, Fakulteta za strojništvo in računalništvo, Poljska

V članku so predstavljene razlike v napetostnih stanjih po nanosu varkov s kotom 90° po standardu EN ISO 5817. Primerjava rezultatov numeričnega modela omogoča izbiro primerne širine varkov pri reparaturnem navarjanju elementov iz malolegiranega srednjeogljičnega jekla (C45).

Cilj je obnovitev začetne geometrije elementa, pomembna pa je tudi izbira dodajnega materiala z ustreznimi lastnostmi (v danem primeru je ta enak osnovnemu materialu). Te lastnosti so v veliki meri odvisne od fazne sestave. Dodajni material vpliva na trdoto, krhkost in duktilnost. Zaradi dragih eksperimentov, ki jih zaradi geometrijskih omejitev pogosto niti ni mogoče izvesti, je bila sprejeta odločitev o numerični analizi problema. Model je bilo mogoče poenostaviti iz treh v dve razsežnosti (simetrija izračunov za dolge varke), zato so bili opravljeni izračuni po metodi končnih elementov v prečno postavljeni ravnini glede na smer nanosa. Vsak novi varek je bil upoštevan kot dodatna površina v mreži končnih elementov.

Opravljena je bila analiza vpliva širine varkov (0,006 m, 0,01 m in 0,014 m) in temperature predgrevanja na fazne transformacije in efektivne napetosti obnovljenega sloja. Uporabljen je bil nestandarden način predgrevanja (pred nanosom vsakega varka, po ohladitvi na temperaturo okolice). V članku je analiziranih 12 različnih kombinacij temperatur predgrevanja in širin varkov za doseganje ustreznega navarjenega sloja brez neskladnosti. Vsi preračuni so bili opravljeni z avtorsko zaščitenim programom. Model vključuje ustrezne odvisnosti med elementi za modeliranje temperatur in faznih transformacij nad oz. pod temperaturo likvidus (T_L) in solidus (T_S). Upoštevane so tudi odvisnosti med zgornjimi modeli in modelom mehanskih lastnosti.

Iz rezultatov sledi sklep, da povečanje širine varkov ugodno vpliva na zmanjšanje stopnje efektivnih preostalih napetosti, kar pa je težko izvedljivo v praksi. Napetosti so najmanj ugodne v prvi površini navara. Pri nižjih temperaturah predgrevanja in ožjih varkih so bila identificirana območja možnih razpok. V tem primeru je treba uporabiti nižjo temperaturo predgrevanja in popuščanje, kar je povezano s podobnimi stroški energije kot pri višjih temperaturah predgrevanja.

Načrtovana je tudi eksperimentalna raziskava za potrditev teh rezultatov, konkretno metalografske preiskave za opredelitev doseženih faznih transformacij. To še zlasti velja za območja, kjer prihaja do ponovnega ogrevanja. Načrtovani so tudi preizkusi trdote materiala. Ti bodo lahko potrdili analizo sestave navara in osnovnega materiala, kakor tudi rezultate numeričnih simulacij. Analiza trdote je lahko tudi izhodišče za konstruiranje elementov, ki jih je mogoče obnoviti ali so namenjeni abrazivni obdelavi.

V inženirski praksi se pred opredelitvijo postopka navarjanja elementov iz težavnih materialov, kot so tisti z visoko vsebnostjo ogljika, opravi serija eksperimentalnih raziskav. V članku je predstavljen numerični model, ki lahko v veliki meri nadomesti te raziskave. Analiza napetostnega stanja, opredeljenega z numeričnimi simulacijami, bo omogočila izbiro ustreznih parametrov procesa za komponente zahtevnih oblik, ki niso primerne za eksperimentalne študije s poenostavljeno geometrijo. Predstavljena analiza faznih premen v trdnem stanju in nastalih napetosti omogoča napovedovanje vedenja obnovljene površine in samega navara, ne le v območju stabilnega procesa (središče navara), temveč tudi na njegovem začetku in koncu. Rezultati analize bodo uporabni za izbiro širine varkov pri reparaturnem navarjanju.
Ključne besede: računalniška mehanika, numerična simulacija, navar, predgrevanje, analiza deformacij, napetost

*Naslov avtorja za dopisovanje: Tehniška univerza v Čenstohovi, Fakulteta za strojništvo in računalništvo, Poljska, joanna.wrobel@icis.pcz.pl

Strojniški vestnik - Journal of Mechanical Engineering 66(2020)10, SI 73
Prejeto v recenzijo: 2020-07-25
Prejeto popravljeno: 2020-09-14
Odobreno za objavo: 2020-09-21

Vpliv termobariernih prevlek na toplotne napetosti v lopaticah in šobah plinskih mikroturbin

Oscar Tenango-Pirin[1] – Elva Reynoso-Jardón[1] – J.C. García[2]* - Yahir Mariaca[1] – Yuri Sara Hernández[3] – Raúl Ñeco[1] – Omar Dávalos[1]

[1] Avtonomna univerza Ciudad Juárez, Oddelek za strojništvo, Mehika
[2] Avtonomna univerza Estado de Morelos, Raziskovalni center za strojništvo, Mehika
[3] Pachuca tehnološki inštitut, Mehika

Termobarierne prevleke (TBC) pomembno vplivajo na življenjsko dobo mikroturbin, saj omejujejo prenos toplote v komponente. Visokotemperaturne obremenitve lahko skrajšajo življenjsko dobo komponent s tem, da povzročijo nastanek območij visokih napetosti v lopaticah in šobah.

V pričujočem članku so predstavljene numerične analize za vrednotenje novih materialov, ki so bili razviti za termobarierne prevleke lopatic plinskih turbin. Ocenjena je njihova zmogljivost za zaščito komponent mikroturbin. Preučeni so bili novi materiali 8YSZ, Mg_2SiO_4, $Y_3Ce_7Ta_2O_{23.5}$ in $Yb_3Ce_7Ta_2O_{23.5}$. Ti materiali iz literature so bili do zdaj preizkušeni samo v nadzorovanih pogojih in zato so bila v pričujoči raziskavi simulirana okolja, ki so podobna pogojem obratovanja plinskih mikroturbin. Za substrat šobe in lopatic so bile uporabljene lastnosti zlitine Nimonic 105.

Razvit je bil 3D-model plinske mikroturbine, model interakcij med fluidom in konstrukcijo pa je bil razrešen s CFD in MKE. V izračunih CFD so bile za TBC na šobi in lopatici uporabljene lastnosti zgornjih materialov. Pri računanju prenosa toplote iz visokotemperaturnega plina na substrat sta bili upoštevani domeni kapljevinaste in trdne snovi. Izračunana so bila temperaturna polja in amplitude napetosti na šobi in lopatici, rezultati pa so bili nato primerjani z rezultati modela brez toplotnih barier. Neenakomerne temperaturne porazdelitve v šobah in lopaticah so bile v naslednjem koraku uporabljene za izračun napetosti v substratu. Za oceno učinkovitosti toplotne izolacije TBC so bile analizirane temperaturne vrednosti in gradienti v substratu.

Maksimalne temperature so bile ugotovljene na sprednjem in na zadnjem robu šobe in lopatice, tako s prevlekami TBC kot brez njih. Višji temperaturni gradienti so bili ugotovljeni na šobi, maksimalne amplitude temperatur pa na lopaticah. Absolutna vrednost temperatur se je zmanjšala pri uporabi TBC. Ugotovljeno je bilo, da materiali Mg_2SiO_4 in $Y_3Ce_7Ta_2O_{23.5}$ zagotavljajo boljšo toplotno izolacijo komponent turbine v primerjavi z drugimi materiali. Analiza napetosti je pokazala, da so se toplotne napetosti pri uporabi TBC zmanjšale v obeh komponentah, ne glede na uporabljen material. Razvoj napetosti v komponentah je bil v vseh primerih zelo podoben, ugotovljena pa je bila variabilnost njihove amplitude. Največje napetosti pri šobi in pri lopatici so se razvile v predelu korena, kar je mogoče pripisati temperaturnim gradientom in omejitvam. Materiala Mg_2SiO_4 in $Y_3Ce_7Ta_2O_{23.5}$ izkazujeta najboljše termoizolacijske lastnosti za komponente mikroturbin.

V študiji je bila ovrednotena samo sposobnost materialov za zaščito lopatic in šob plinskih mikroturbin pred toplotnimi obremenitvami. Raziskava tako prinaša nova spoznanja na področju optimizacije plinskih mikroturbin in metod za zaščito teh izdelkov pred visokimi temperaturami in napetostmi.

Znano je, da lahko povečanje amplitude napetosti nastopi tudi zaradi vpliva drugih obremenitev, kot so centrifugalne sile ali poškodbe zaradi tujkov. Te obremenitve v tukajšnji raziskavi niso bile zajete.

Ključne besede: termobarierna prevleka, plinske mikroturbine, lopatica turbine, toplotne napetosti, računalniška dinamika fluidov, končni elementi

*Naslov avtorja za dopisovanje: Avtonomna univerza Ciudad Juárez, Oddelek za strojništvo, Av. Universidad 1001, Cuernavaca, Mor., Mehika, jcgarcia@uaem.mx

Strojniški vestnik - Journal of Mechanical Engineering 66(2020)10, SI 74

Prejeto v recenzijo: 2020-04-07
Prejeto popravljeno: 2020-08-04
Odobreno za objavo: 2020-09-01

Učinek prevlek lopatic na delovanje centrifugalnih črpalk pri toku z usedlinami

Yong Wang[1] – Zilong Zhang[1] – Jie Chen[2] – Houlin Liu[1] – Xiang Zhang[3] * – Marko Hočevar[4]
[1] Jiangsu univerza, Raziskovalni center za dinamiko fluidov, Kitajska
[2] Tehnološki inštitut v Pekingu, Fakulteta za strojništvo, Kitajska
[3] Xihua univerza, Laboratorij za fluide, Kitajska
[4] Univerza v Ljubljani, Fakulteta za strojništvo, Slovenija

Centrifugalne črpalke pogosto črpajo tok z usedlinami, npr. za namakanje, v metalurgiji, rudarstvu itd.. Trdna faza v sedimentu povzroči abrazijo omočenih površin, predvsem lopatic, kar vodi do povečanega hrupa, vibracij, puščanja in na koncu do odpovedi črpalke. Zaradi velike hitrosti vrtenja rotorja do odpovedi pride najpogosteje zaradi poškodb na tlačni površini lopatic rotorja. Poleg tega močne vibracije, nihanje tlaka in abrazija materiala poškodovane centrifugalne črpalke znatno zmanjšajo zanesljivost sistema črpališč in povzročajo onesnaževanje okolja s hrupom. Z nanašanjem trdih prevlek na površino lopatic centrifugalnih črpalk želimo podaljšati življenjsko dobo črpalk pri črpanju toka z usedlinami. Študij tokov v dvofaznih dvofaznih centrifugalnih črpalkah z zaščitnimi premazi na lopaticah je v nam dostopni literaturi malo. Trenutno se raziskave na tem področju izvajajo predvsem s pomočjo numeričnih simulacij. Čeprav je numerična simulacija učinkovita metoda za napovedovanje rezultatov, so natančni eksperimenti bistveni za raziskave delovanja.

Da bi raziskali učinek trdih prevlek, smo eksperimentalno preučevali fluktuacije energije, vibracij in tlaka centrifugalne črpalke. Konstrukcijski parametri modelne črpalke so naslednji: nazivni pretok Q_d = 20 m³/h, višina H = 22 m, izkoristek η = 48 %, nazivna moč gredi P = 1,5 kW, hitrost vrtenja n = 2900 vrt/min in specifična hitrost n_s = 81,46. Merilno postajo so sestavljali cevovodi, rezervoar za vodo, izstopni ventil, potopna črpalka, dovodni ventil, elektromagnetni merilnik pretoka, model črpalke s frekvenčnim pogonom, sistem za merjenje fluktuacij tlaka, sistem za merjenje vibracij in sistem za merjenje električne moči črpalke. V poskusu je bila uporabljena enostopenjska horizontalna centrifugalna modelna črpalka z ravnimi lopaticami.

Kot zaščitni material, uporabljen na tlačni površini lopatic, je bil izbran poliuretan. Poliuretanska obloga je bila izdelana s tehnologijo 3D tiska. Debelino prevleke smo predstavili v brezdimenzijski obliki, pri čemer je Ki koeficient debeline prevleke, i = 0, 1, 2, 3. Debeline prevleke so znašale 0 mm, 1 mm, 2 mm, 3 mm, ustrezni koeficienti debeline prevleke pa znašajo $K_0 = 0$, $K_1 = 1$, $K_2 = 2$ in $K_3 = 3$

Rezultati kažejo, da je dobavna višina pri črpanju vode z usedlinami nekoliko večja kot pri čisti vodi z enakim koeficientom debeline prevleke, kadar je volumetrični pretok pod približno 0,9 nazivnega pretoka. Pri večjih pretokih je dobavna višina v primeru črpanja čiste vode višja.

Če vstopni in izstopni kot ter oblika lopatic ostanejo nespremenjeni, se višina H in izkoristek η pri črpanju čiste vode in vode z usedlinami znatno zmanjšata s povečanjem koeficienta debeline prevleke. Frekvenca vrtenja rotorja in frekvenca prehoda lopatic BPF sta glavni frekvenci vzbujanja vibracij črpalke in nihanja izhodnega tlaka. Amplituda hitrosti vibracij in nihanje izhodnega tlaka pri frekvenci 1 BPF sta največja, na drugem mestu pa sledi primer pri frekvenci vrtenja rotorja. Najvišje vrednosti amplitude hitrosti vibracij in nihanja izhodnega tlaka so sorazmerne s koeficientom debeline prevleke.

Analiza je bila izvedena za več naraščajočih debelin prevlek, kar ustreza koeficientom od K_0 do K_3. Pri koeficientih debeline prevleke K_0, K_1 in K_2 je amplituda hitrosti vibracij pri črpanju toka z usedlinami večja od vrednosti pri črpanju čiste vode, medtem ko je pri koeficientu debeline prevleke K_3 razlika zelo majhna. Amplitude nihanj tlaka pri različnih pretokih se najprej zmanjšajo in nato povečajo s povečevanjem koeficienta debeline prevleke, najnižje vrednosti pa so pri koeficientu debeline prevleke K_1.

Ključne besede: centrifugalna črpalka, obraba, prevleka lopatic, vibracije, fluktuacije tlaka, tok z usedlinami

*Naslov avtorja za dopisovanje: Xihua univerza, Laboratorij za fluide, Chengdu, Kitajska, 927340633@qq.com

Strojniški vestnik - Journal of Mechanical Engineering 66(2020)10, SI 75

Prejeto v recenzijo: 2020-04-30
Prejeto popravljeno: 2020-07-30
Odobreno za objavo: 2020-09-03

Napovedovanje deformacijskih mej za napredno dvofazno visokotrdno jeklo DP600 z modelom Marciniak-Kuczynski in novim polempiričnim modelom krivulje mejnih deformacij

Ilyas Kacar[1,*] - Fahrettin Ozturk[2, 3] - Serkan Toros[4] - Suleyman Kilic[5]
[1] Univerza Ömerja Halisdemirja v provinci Nigde, Turčija
[2] Turška letalska in vesoljska industrija, Turčija
[3] Univerza Yıldırıma Beyazıta v Ankari, Turčija
[4] Univerza Nigde Ömer Halisdemir, Turčija
[5] Univerza Ahija Evrana v Kirsehirju, Turčija

Krivulja mejnih deformacij (KMD) je uporabno orodje za načrtovanje procesov preoblikovanja pločevine. V pričujočem članku je predstavljen nov polempirični model krivulje mejnih deformacij, ki določa mejo preoblikovalnosti in varno območje v različnih pogojih preoblikovanja pločevine, obenem pa je tudi učinkovito orodje za diagnosticiranje napak v izdelavi. V predstavljeni študiji je bila za napovedovanje krivulje mejnih deformacij uporabljena kombinacija modela Marciniak-Kuczynski in nekaterih anizotropnih kriterijev tečenja. Krivulje so bile ovrednotene z rezultati eksperimentov, opravljenih na jeklu DP600.

Napredna visokotrdna jekla, med katera spada tudi dvofazno jeklo DP600, se uporabljajo za zmanjševanje teže vozil. Z določitvijo mejnih deformacij jekla DP600 je mogoče zagotoviti preoblikovanje brez napak, primeren model pa omogoča tudi točnost napovedi simulacij.

Modeli plastičnosti so bili izpeljani s funkcijami Hill48, Barlat89 in YLD2000-2d. Modeli so bili kombinirani z modelom M-K in s predlaganim kriterijem porušitve, določen je bil najprimernejši kriterij za popis anizotropije. Model in iz njega izpeljane krivulje so uporabni in dovolj natančni za različne vrste deformacij jekla DP600. Predlagani kriterij porušitve je bil določen z regresijsko analizo eksperimentalno pridobljenih KMD. Pri modeliranju KMD so bile opredeljene splošne mehanske lastnosti, ki vplivajo na KMD materiala. Pri analizi prileganja s preprostimi matematičnimi formulami so bile konstante nato omejene z danimi eksperimentalno določenimi lastnostmi.

Formula po Marciniaku in Kuczynskem kot najbolj priljubljeni porušitveni kriterij je bila primerjana z novim polempiričnim kriterijem porušitve za pločevino. Najbolj konzervativna in najprimernejša funkcija deformacije med funkcijami izotropije za kriterij porušitve pločevine DP600 je YLD2000-2d. Predstavljeni so parametri modela YLD2000-2d. Na krivuljah mejnih deformacij so predstavljene možnosti napovedovanja deformacijskih mej.

Za jeklo DP600 so bile preučene deformacijske meje. Funkcije anizotropne deformacije so bile uporabljene z modelom M-K in z novim polempiričnim modelom. Za oba modela so bile določene zmožnosti napovedovanja deformacijskih mej. Zaključki so:

- Ocenjena krivulja plastičnosti, koeficienti anizotropije in normalizirane meje plastičnosti materiala DP600 se dobro ujemajo z eksperimentalnimi podatki za kriterij YLD2000-2d.
- YLD2000-2d je najprimernejša krivulja v območju pozitivnih deformacij KMD, zato ima prednost pri napovedovanju porušitve pločevine DP600. Uporabna je za vse debeline pločevine.
- Predlagani model v kombinaciji s krivuljo YLD20002d zagotavlja najbolj natančne napovedi porušitve pločevine DP600.

Ključne besede: DP600, anizotropija, kriterij tečenja, krivulja mejnih deformacij, kriterij porušitve M-K

*Naslov avtorja za dopisovanje: Univerza Ömerja Halisdemirja v provinci Nigde, Nigde 51240, Turčija, ikacar@gmail.com

Strojniški vestnik - Journal of Mechanical Engineering 66(2020)10, SI 76

Prejeto v recenzijo: 2020-04-03
Prejeto popravljeno: 2020-07-30
Odobreno za objavo: 2020-09-01

Raziskava metode za zmanjševanje šuma na osnovi DTCWT in cikličnega spektra razlik singularnih energij

Xihui Chen[1,2,*] – Gang Cheng[2,4] – Ning Liu[3] – Xinhui Shi[1] – Wei Lou[1]

[1] Univerza Hohai, Kolidž za strojništvo in elektrotehniko, Kitajska
[2] Kitajska rudarska in tehniška univerza, Šola za mehatroniko, Kitajska
[3] Kitajska tehnologija premoga in strojništvo, Kitajska
[4] Shandong Zhongheng Optoelektronska tehnologija, Kitajska

Zobniki so najpomembnejši del prenosnih sistemov v mehanski opremi, z nadzorom in diagnostično obravnavo delovanja zobnikov pa je mogoče izboljšati zanesljivost mehanske opreme. Mehanska oprema običajno obratuje v zahtevnih razmerah. Signal vibracij zobnikov je v realnih delovnih pogojih obremenjen z močnim šumom, to pa je velik izziv za učinkovito diagnosticiranje napak na zobnikih.

Za razrešitev problema močnega šuma v signalu vibracij je predlagana metoda za zmanjševanje šuma na podlagi dvodrevesne kompleksne valčne transformacije in cikličnega spektra razlik singularnih energij.

Signal vibracij zobnikov z močnim šumom se s pomočjo časovno-frekvenčne analize DTCWT najprej razstavi na vrsto signalnih komponent z različnimi frekvenčnimi karakteristikami. Sledi predlagana metoda cikličnega spektra razlik singularnih energij, ki sloni na pristopu s kaskadnim ciklom in postopno odpravo šuma za obdelavo posameznih signalnih komponent z različnimi frekvenčnimi karakteristikami. Pogoje za zaključek metode cikličnega spektra razlik singularnih energij je mogoče prilagoditi lastnostim porazdelitve šuma v različnih frekvenčnih pasovih. Končno zmanjšanje šuma v originalnem signalu vibracij se izvede z rekonstrukcijo očiščenih posameznih signalnih komponent z različnimi frekvenčnimi pasovi. Članek sodi v področje obdelave signalov elektromehanske opreme.

Opravljeni so bili tudi eksperimenti za preverjanje učinkovitosti predlagane metode zmanjševanja šuma na podlagi DTCWT in metode cikličnega spektra razlik singularnih energij, ki je učinkovita in primerna za zmanjševanje šuma v signalu vibracij.

V nadaljnjih študijah metode cikličnega spektra razlik singularnih energij bodo podrobneje preučeni pogoji za končanje cikla.

Signali vibracij mehanske opreme, pridobljeni v realnih delovnih pogojih, so obremenjeni z močnim šumom, ki otežuje učinkovito izločanje značilk napak. Predstavljena je metoda za zmanjševanje šuma na osnovi DTCWT in cikličnega spektra razlik singularnih energij, ki sloni na ideji kaskadnega cikla in postopne odprave šuma. Uspešnost predlagane metode je bila dokazana s simulacijami in eksperimentalno. Metoda je uporabna v procesu preobdelave signalov mehanske opreme in je osnova za nadaljnje diagnosticiranje napak in napovedovanje življenjske dobe.

Ključne besede: zmanjševanje šuma, DTCWT, singularni razcep, ciklični spekter razlik singularnih energij, signal vibracij

*Naslov avtorja za dopisovanje: Univerza Hohai, Kolidž za strojništvo in elektrotehniko, Kitajska, chenxh@hhu.edu.cn

Guide for Authors

All manuscripts must be in English. Pages should be numbered sequentially. The manuscript should be composed in accordance with the Article Template given above. The maximum length of contributions is 12 pages (approx. 5000 words). Longer contributions will only be accepted if authors provide justification in a cover letter. For full instructions see the Information for Authors section on the journal's website: http://en.sv-jme.eu .

SUBMISSION:

Submission to SV-JME is made with the implicit understanding that neither the manuscript nor the essence of its content has been published previously either in whole or in part and that it is not being considered for publication elsewhere. All the listed authors should have agreed on the content and the corresponding (submitting) author is responsible for having ensured that this agreement has been reached. The acceptance of an article is based entirely on its scientific merit, as judged by peer review. Scientific articles comprising simulations only will not be accepted for publication; simulations must be accompanied by experimental results carried out to confirm or deny the accuracy of the simulation. Every manuscript submitted to the SV-JME undergoes a peer-review process.

The authors are kindly invited to submit the paper through our web site: http://ojs.sv-jme.eu. The Author is able to track the submission through the editorial process - as well as participate in the copyediting and proofreading of submissions accepted for publication - by logging in, and using the username and password provided.

SUBMISSION CONTENT:

The typical submission material consists of:

- A **manuscript** (A PDF file, with title, all authors with affiliations, abstract, keywords, highlights, inserted figures and tables and references),
- Supplementary files:
  - a **manuscript** in a WORD file format
  - a **cover letter** (please see instructions for composing the cover letter)
  - a ZIP file containing **figures** in high resolution in one of the graphical formats (please see instructions for preparing the figure files)
  - possible **appendicies** (optional), cover materials, video materials, etc.

Incomplete or improperly prepared submissions will be rejected with explanatory comments provided. In this case we will kindly ask the authors to carefully read the Information for Authors and to resubmit their manuscripts taking into consideration our comments.

COVER LETTER INSTRUCTIONS:

Please add a **cover letter** stating the following information about the submitted paper:

1. Paper **title**, list of **authors** and their **affiliations**. **One** corresponding author should be provided.
2. **Type of paper**: original scientific paper (1.01), review scientific paper (1.02) or short scientific paper (1.03).
3. A **declaration** that neither the manuscript nor the essence of its content has been published in whole or in part previously and that it is not being considered for publication elsewhere.
4. State the **value of the paper** or its practical, theoretical and scientific implications. What is new in the paper with respect to the state-of-the-art in the published papers? Do not repeat the content of your abstract for this purpose.
5. We kindly ask you to suggest at least two **reviewers** for your paper and give us their names, their full affiliation and contact information, and their scientific research interest. The suggested reviewers should have at least two relevant references (with an impact factor) to the scientific field concerned; they should not be from the same country as the authors and should have no close connection with the authors.

FORMAT OF THE MANUSCRIPT:

The manuscript should be composed in accordance with the Article Template. The manuscript should be written in the following format:

- A **Title** that adequately describes the content of the manuscript.
- A list of **Authors** and their **affiliations**.
- An **Abstract** that should not exceed 250 words. The Abstract should state the principal objectives and the scope of the investigation, as well as the methodology employed. It should summarize the results and state the principal conclusions.
- 4 to 6 significant **key words** should follow the abstract to aid indexing.
- 4 to 6 **highlights;** a short collection of bullet points that convey the core findings and provide readers with a quick textual overview of the article. These four to six bullet points should describe the essence of the research (e.g. results or conclusions) and highlight what is distinctive about it.
- An **Introduction** that should provide a review of recent literature and sufficient background information to allow the results of the article to be understood and evaluated.
- A **Methods** section detailing the theoretical or experimental methods used.
- An **Experimental section** that should provide details of the experimental set-up and the methods used to obtain the results.
- A **Results** section that should clearly and concisely present the data, using figures and tables where appropriate.
- A **Discussion** section that should describe the relationships and generalizations shown by the results and discuss the significance of the results, making comparisons with previously published work. (It may be appropriate to combine the Results and Discussion sections into a single section to improve clarity.)
- A **Conclusions** section that should present one or more conclusions drawn from the results and subsequent discussion and should not duplicate the Abstract.
- **Acknowledgement** (optional) of collaboration or preparation assistance may be included. Please note the source of funding for the research.
- **Nomenclature** (optional). Papers with many symbols should have a nomenclature that defines all symbols with units, inserted above the references. If one is used, it must contain all the symbols used in the manuscript and the definitions should not be repeated in the text. In all cases, identify the symbols used if they are not widely recognized in the profession. Define acronyms in the text, not in the nomenclature.
- **References** must be cited consecutively in the text using square brackets [1] and collected together in a reference list at the end of the manuscript.
- **Appendix(-icies)** if any.

SPECIAL NOTES

Units: The SI system of units for nomenclature, symbols and abbreviations should be followed closely. Symbols for physical quantities in the text should be written in italics (e.g. v, T, n, etc.). Symbols for units that consist of letters should be in plain text (e.g. ms^{-1}, K, min, mm, etc.). Please also see: http://physics.nist.gov/cuu/pdf/sp811.pdf .

Abbreviations should be spelt out in full on first appearance followed by the abbreviation in parentheses, e.g. variable time geometry (VTG). The meaning of symbols and units belonging to symbols should be explained in each case or cited in a **nomenclature** section at the end of the manuscript before the References.

Figures (figures, graphs, illustrations digital images, photographs) must be cited in consecutive numerical order in the text and referred to in both the text and the captions as Fig. 1, Fig. 2, etc. Figures should be prepared without borders and on white grounding and should be sent separately in their original formats. If a figure is composed of several parts, please mark each part with a), b), c), etc. and provide an explanation for each part in Figure caption. The caption should be self-explanatory. Letters and numbers should be readable (Arial or Times New Roman, min 6 pt with equal sizes and fonts in all figures). Graphics (submitted as supplementary files) may be exported in resolution good enough for printing (min. 300 dpi) in any common format, e.g. TIFF, BMP or JPG, PDF and should be named Fig1.jpg, Fig2.tif, etc. However, graphs and line drawings should be prepared as vector images, e.g. CDR, AI. Multi-curve graphs should have individual curves marked with a symbol or otherwise provide distinguishing differences using, for example, different thicknesses or dashing.

Tables should carry separate titles and must be numbered in consecutive numerical order in the text and referred to in both the text and the captions as Table 1, Table 2, etc. In addition to the physical quantities, such as t (in italics), the units [s] (normal text) should be added in square brackets. Tables should not duplicate data found elsewhere in the manuscript. Tables should be prepared using a table editor and not inserted as a graphic.

REFERENCES:

A reference list must be included using the following information as a guide. Only cited text references are to be included. Each reference is to be referred to in the text by a number enclosed in a square bracket (i.e. [3] or [2] to [4] for more references; do not combine more than 3 references, explain each). No reference to the author is necessary.

References must be numbered and ordered according to where they are first mentioned in the paper, not alphabetically. All references must be complete and accurate. Please add DOI code when available. Examples follow.

Journal Papers:

Surname 1, Initials, Surname 2, Initials (year). Title. Journal, volume, number, pages, DOI code.

[1] Hackenschmidt, R., Alber-Laukant, B., Rieg, F. (2010). Simulating nonlinear materials under centrifugal forces by using intelligent cross-linked simulations. *Strojniški vestnik - Journal of Mechanical Engineering,* vol. 57, no. 7-8, p. 531-538, DOI:10.5545/sv-jme.2011.013.

Journal titles should not be abbreviated. Note that journal title is set in italics.

Books:

Surname 1, Initials, Surname 2, Initials (year). Title. Publisher, place of publication.

[2] Groover, M.P. (2007). *Fundamentals of Modern Manufacturing*. John Wiley & Sons, Hoboken.

Note that the title of the book is italicized.

Chapters in Books:

Surname 1, Initials, Surname 2, Initials (year). Chapter title. Editor(s) of book, book title. Publisher, place of publication, pages.

[3] Carbone, G., Ceccarelli, M. (2005). Legged robotic systems. Kordić, V., Lazinica, A., Merdan, M. (Eds.), Cutting Edge Robotics. Pro literatur Verlag, Mammendorf, p. 553-576.

Proceedings Papers:

Surname 1, Initials, Surname 2, Initials (year). Paper title. Proceedings title, pages.

[4] Štefanić, N., Martinčević-Mikić, S., Tošanović, N. (2009). Applied lean system in process industry. *MOTSP Conference Proceedings*, p. 422-427.

Standards:

Standard-Code (year). Title. Organisation. Place.

[5] ISO/DIS 16000-6.2:2002. *Indoor Air – Part 6: Determination of Volatile Organic Compounds in Indoor and Chamber Air by Active Sampling on TENAX TA Sorbent, Thermal Desorption and Gas Chromatography using MSD/FID.* International Organization for Standardization. Geneva.

WWW pages:

Surname, Initials or Company name. Title, from http://address, date of access.

[6] Rockwell Automation. Arena, from *http://www.arenasimulation.com,* accessed on 2009-09-07.

EXTENDED ABSTRACT:

When the paper is accepted for publishing, the authors will be requested to send an **extended abstract** (approx. one A4 page or 3500 to 4000 characters or approx. 600 words). The instruction for composing the extended abstract are published on-line: http://www.sv-jme.eu/information-for-authors/ .

COPYRIGHT:

Authors submitting a manuscript do so on the understanding that the work has not been published before, is not being considered for publication elsewhere and has been read and approved by all authors. The submission of the manuscript by the authors means that the authors automatically agree to transfer copyright to SV-JME when the manuscript is accepted for publication. All accepted manuscripts must be accompanied by a Copyright Transfer Agreement, which should be sent to the editor. The work should be original work by the authors and not be published elsewhere in any language without the written consent of the publisher. The proof will be sent to the author showing the final layout of the article. Proof correction must be minimal and executed quickly. Thus it is essential that manuscripts are accurate when submitted. Authors can track the status of their accepted articles on http://en.sv-jme.eu/.

PUBLICATION FEE:

Authors will be asked to pay a publication fee for each article prior to the article appearing in the journal. However, this fee only needs to be paid after the article has been accepted for publishing. The fee is 380 EUR (for articles with maximum of 6 pages), 470 EUR (for articles with maximum of 10 pages), plus 50 EUR for each additional page. The additional cost for a color page is 90.00 EUR (only for a journal hard copy; optional upon author's request). These fees do not include tax.

Strojniški vestnik -Journal of Mechanical Engineering
Aškerčeva 6, 1000 Ljubljana, Slovenia, e-mail: info@sv-jme.eu

9 770039 248001
ISSN 0039-2480

http://www.sv-jme.eu

Contents

Papers